

**PHOTOCATALYTIC DEGRADATION OF SUNSET  
YELLOW BY HYDROTHERMALLY SYNTHESIZED  
THREE-DIMENSIONAL FLOWER-LIKE BISMUTH  
OXYBROMIDE WITH HIERARCHICAL STRUCTURE**

**LIM CHIN AIK**

**MASTER OF ENGINEERING SCIENCE**

**FACULTY OF ENGINEERING AND GREEN  
TECHNOLOGY**

**UNIVERSITI TUNKU ABDUL RAHMAN**

**2018**

**PHOTOCATALYTIC DEGRADATION OF  
SUNSET YELLOW BY HYDROTHERMALLY  
SYNTHESIZED THREE-DIMENSIONAL  
FLOWER-LIKE BISMUTH OXYBROMIDE  
WITH HIERARCHICAL STRUCTURE**

By

**LIM CHIN AIK**

A thesis submitted to the Faculty of Engineering and  
Green Technology, Universiti Tunku Abdul  
Rahman, in partial fulfilment of the requirements for  
the degree of Master in Engineering Science.

May 2018

# **PHOTOCATALYTIC DEGRADATION OF SUNSET YELLOW BY HYDROTHERMALLY SYNTHESIZED THREE-DIMENSIONAL FLOWER-LIKE BISMUTH OXYBROMIDE WITH HIERARCHICAL STRUCTURE**

## **ABSTRACT**

Heterogeneous photocatalysis under visible light irradiation has shown considerable potential in the area of wastewater treatment. This thesis described the synthesis, characterization and applicability of a visible light active photocatalyst, bismuth oxybromide (BiOBr). Flower-like BiOBr hierarchical structures were successfully synthesized by a simple hydrothermal method. The as-synthesized samples were characterized by X-ray diffraction (XRD), energy-dispersive X-ray spectroscopy (EDX), field-emission scanning electron microscopy (FESEM), transmission electron microscopy (TEM), high resolution transmission electron microscopy (HRTEM), X-ray photoelectron spectroscopy (XPS), UV-visible diffuse reflectance spectroscopy (UV-vis DRS) and nitrogen adsorption-desorption analysis. The diffraction peak of XRD characterization at 10.9°, 21.9°, 25.2°, 31.7°, 32.2°, 34.1°, 39.3°, 44.6°, 46.4°, 46.9°, 50.7°, 53.4°, 56.2°, 57.1°, 61.9°, 66.2° and 67.4° indicated that the as-prepare BiOBr.were tetragonal phase pure BiOBr and demonstrated well-crystalline. Besides, the FESEM images showed that the as-synthesized BiOBr were accumulated by large amount of interleaving nanosheets and formed an open porous structure through oriented aggregation. EDX and XPS spectra of flower-like BiOBr hierarchical structures detected the existence of Bi, O and Br on the surface of the samples. The good optical properties of as-synthesized BiOBr were characterized by UV-vis DRS. The flower-like BiOBr fundamental

photoabsorption edge at 430 nm while the TiO<sub>2</sub> exhibited photoabsorption below 400 nm.

. In this research, the photocatalytic activity of as-synthesized BiOBr was studied for the degradation of sunset yellow (SSY) aqueous solution. Under fluorescent light irradiation flower-like BiOBr hierarchical structures can degrade 53.5% of SSY while BiOBr nanosheets and TiO<sub>2</sub> can degrade 46.2 % and 41.4% of SSY degradation under 10 ppm of initial SSY concentration, 1.0 g/L of catalyst and natural SSY pH value. Such enhancement was attributed to the unique hierarchical porous surface structure of flower-like BiOBr with excellent visible light absorption ability. This can improve the generation and separation of electron-hole pairs leading to high yield of hydroxyl radicals as proven by the photoluminescence spectra. In addition, the photocatalytic studies showed that various effects of parameters exerted their individual influence on the degradation of SSY. The degradation of SSY reached 73.3% when the catalyst loading was at 1.00 g/L, initial SSY concentration at 10 ppm and solution pH at pH 3.0. For the study on the effect of inorganic anions, the photocatalytic activity of as-synthesized BiOBr was inhibited due to the scavenging effect of inorganic anions. Moreover, the as-synthesized BiOBr samples still able to degrade 70% of SSY after four cycles which indicating the good potential of as-synthesized BiOBr for practical applications in environmental remediation. The degradation of SSY was fitted into the first order kinetic and the widely accepted Langmuir-Hinshelwood kinetic model was suggested for the reaction kinetic in this study. Using response surface methodology (RSM), the optimum conditions for SSY degradation were 1.30 g/L flower-like BiOBr, 10 ppm SSY concentration, pH 3.0 and 180 min

irradiation. Lastly, the flower-like BiOBr hierarchical structures can be considered as promising photocatalysts for wastewater treatment due to the ability to degrade organic pollutants under both fluorescent light and sunlight irradiation.

## ACKNOWLEDGEMENTS

I would first like to thank my supervisor, Dr. Sin Jin Chung for his guidance, assistance and patience throughout my study. The door of Dr. Sin's office always open when I encountering problem and trouble on my research or writing. He consistently steered me to the right direction whenever he thought I needed it. Besides, I would also like to extend my appreciation to my co-supervisors, Dr. Lo Po Kim and Dr. Lam Sze Mun for their advice and encouragement. I am also taking this chance to sincerely apologize to them for any inconvenience I have caused them.

I am thankful to the Head of Department of Laboratory Management and Safety Administration, Ir. Dr. Low Chong Yu for his support and assistance toward making this research a success. I would also like to thank the staffs and lab officers who were involved in this research project: Pn. Ropidah Hamimi, Ms. Lim Cheng Yen, Mr. Chin Kah Seng and Ms. Mirohsha. Without their passionate participation, guidance and assistance, this research could not have been successfully conducted. Additionally, I am grateful to Ms. Ng Suk Ting and Ms. Noor Hazreena for the help with sample analyses.

Finally, I must express my very profound gratitude to my parents and to my friends for providing me with unfailing support and continuous encouragement throughout my years of study and through the process of researching and writing this thesis. This accomplishment may not be possible without them. Thank you.

## APPROVAL SHEET

This thesis/dissertation entitled “**PHOTOCATALYTIC DEGRADATION OF SUNSET YELLOW BY HYDROTHERMALLY SYNTHESIZED THREE-DIMENSIONAL FLOWER-LIKE BISMUTH OXYBROMIDE WITH HIERARCHICAL STRUCTURE**” was prepared by LIM CHIN AIK and submitted as partial fulfilment of the requirements for the degree of Master of Engineering Science at Universiti Tunku Abdul Rahman.

Approved by:

---

(Dr. SIN JIN CHUNG)  
Supervisor  
Department of Petrochemical  
Engineering  
Faculty of Engineering and Green  
Technology  
Universiti Tunku Abdul Rahman

Date:.....

---

(Dr. LO PO KIM)  
Co-supervisor  
Department of Petrochemical  
Engineering  
Faculty of Engineering and Green  
Technology  
Universiti Tunku Abdul Rahman

Date:.....

---

(Dr. LAM SZE MUN)  
Co-supervisor  
Department of Environmental  
Engineering  
Faculty of Engineering and Green  
Technology  
Universiti Tunku Abdul Rahman

Date:.....

**FACULTY OF ENGINEERING AND GREEN TECHNOLOGY**

**UNIVERSITI TUNKU ABDUL RAHMAN**

Date: \_\_\_\_\_

**SUBMISSION OF DISSERTATION**

It is here by certified that **LIM CHIN AIK (16AGM01198)** has completed this thesis entitled “PHOTOCATALYTIC DEGRADATION OF SUNSET YELLOW BY HYDROTHERMALLY SYNTHESIZED THREE-DIMENSIONAL FLOWER-LIKE BISMUTH OXYBROMIDE WITH HIERARCHICAL STRUCTURE” under the supervision of Dr. Sin Jin Chung from the Department of Petrochemical Engineering, Faculty of Engineering and Green Technology and Dr. Lo Po Kim from the Department of Petrochemical Engineering, Faculty of Engineering and Green Technology as well as Dr. Lam Sze Mun, from the Department of Environmental Engineering, Faculty of Engineering and Green Technology.

I understand that the Universiti will upload softcopy of my thesis in pdf format into UTAR Institutional Repository, which may be made accessible to UTAR community and public.

Yours truly,

---

(Lim Chin Aik)



## DECLARATION

I, LIM CHIN AIK hereby declare that the thesis is based on my original work except for quotations and citations which have been duly acknowledged. I also declare that it has not been previously or concurrently submitted for any other degree at UTAR or other institutions.

---

(LIM CHIN AIK)

Date:.....

## TABLE OF CONTENTS

	<b>Page</b>
<b>ABSTRACT</b>	i
<b>ACKNOWLEDGEMENT</b>	iv
<b>APPROVAL SHEET</b>	v
<b>SUBMISSION SHEET</b>	vi
<b>DECLARATION SHEET</b>	vii
<b>TABLE OF CONTENTS</b>	viii
<b>LIST OF TABLES</b>	xii
<b>LIST OF FIGURES</b>	xiii
<b>LIST OF SYMBOLS</b>	xviii
<b>LIST OF ABBREVIATIONS</b>	xix

### **CHAPTER ONE: INTRODUCTION**

1.1	Background of Study	1
1.2	Problem Statement	3
1.3	Objectives	5
1.4	Scope of Study	6
1.5	Organization of Thesis	7

### **CHAPTER TWO: LITERATURE REVIEW**

2.1	Sunset Yellow	9
2.2	Advanced Oxidation Processes (AOPs)	11
2.3	Heterogeneous Photocatalysis	12
2.4	Bismuth Oxybromide (BiOBr) as Photocatalyst	18
2.5	Three Dimensional (3D) BiOBr Hierarchical Structures	20
2.6	Degradation of Azo Dyes Over BiOBr	28
2.7	Effect of Operating Parameters	
2.7.1	Effect of Catalyst Loading	29
2.7.2	Effect of Initial Dye Concentration	33
2.7.3	Effect of Solution pH	37

2.7.4	Effect of Inorganic Anions	40
2.8	Response Surface Methodology (RSM)	43
2.9	Summary of Literature Review	46

### **CHAPTER THREE: METHODOLOGY**

3.1	Overall Flow Chart of Work	47
3.2	List of Chemical and Other Materials	48
3.3	Synthesis of BiOBr Photocatalyst	
3.3.1	Synthesis of Flower-Like BiOBr Hierarchical Structures	49
3.3.2	Synthesis of BiOBr Nanosheets	51
3.4	Characterization Studies	
3.4.1	X-ray Diffraction (XRD)	53
3.4.2	Field-Emission Scanning Electron Microscopy (FESEM) and Energy Dispersive X-ray Spectroscopy (EDX)	53
3.4.3	Transmission Electron Microscopy (TEM) and High Resolution Transmission Electron Microscopy (HRTEM) Analysis	53
3.4.4	X-ray Photoelectron Spectroscopy (XPS)	54
3.4.5	UV-vis Diffuse Reflectance Spectroscopy (UV-vis DRS)	54
3.4.6	Nitrogen Adsorption-Desorption Isotherm Analysis	55
3.5	Photocatalytic Experiment Set Up	55
3.6	Photocatalytic Performance Evaluation	56
3.7	Detection of Active Species	57
3.8	Effect of Operating Parameters	
3.8.1	Effect of Catalyst Loading	58
3.8.2	Effect of Initial Dye Concentration	58
3.8.3	Effect of Solution pH	59
3.8.4	Effect of Inorganic Anion	59
3.9	Optimization Studies Using Response Surface Methodology (RSM)	59

## CHAPTER FOUR: RESULT AND DISCUSSION

4.1	Characterization Studies	
4.1.1	X-Ray Diffraction (XRD)	63
4.1.2	Energy Dispersive X-ray Spectroscopy (EDX)	64
4.1.3	Field Emission Scanning Electron Microscopy (FESEM)	65
4.1.4	Transmission Electron Microscopy (TEM) and High Resolution Transmission Electron Microscopy (HRTEM) Analysis	66
4.1.5	X-ray Photoelectron Spectroscopy (XPS)	68
4.1.6	UV-vis Diffuse Reflectance Spectroscopy (UV-vis DRS)	71
4.2	Proposed Growth Mechanism of Flower-Like BiOBr Hierarchical Structures	72
4.3	Photocatalytic Studies of Flower-Like BiOBr Hierarchical Structures Under Different Conditions	74
4.4	Proposed Photocatalytic Mechanism of Flower-Like BiOBr Hierarchical Structures	
4.4.1	Active Species Trapping Experiments	78
4.4.2	Terephthalic Acid Photoluminescence Probing Technique (TA-PL)	81
4.4.3	Possible Photocatalytic Mechanism	84
4.5	Effect of Operating Parameters	
4.5.1	Effect of BiOBr Loading on Photodegradation of SSY	85
4.5.2	Effect of Initial SSY Concentration on Photodegradation of SSY	88
4.5.3	Effect of Solution pH on Photodegradation of SSY	91
4.5.4	Effect of Inorganic Anions on Photodegradation of SSY	94
4.6	Catalytic Activity of Recycled Flower-Like BiOBr Hierarchical Structures	98
4.7	Kinetic Study	
4.7.1	Determining the Kinetic Order	101
4.7.2	Langmuir-Hinshelwood Model	105

4.8	Optimization Studies Using Response Surface Methodology (RSM)	108
4.9	Photocatalytic Degradation of SSY Over Flower-Like BiOBr Hierarchical Structures Under Sunlight Irradiation	123
<b>CHAPTER FIVE: CONCLUSION AND RECOMMENDATIONS</b>		
5.1	Conclusions	125
5.2	Recommendations	127
<b>REFERENCES</b>		129
<b>APPENDIX</b>		
Appendix I	FESEM images for BiOBr nanosheets	161
Appendix II	N <sub>2</sub> adsorption-desorption isotherm analysis of flower-like BiOBr and BiOBr nanosheets	162
<b>LIST OF PUBLICATIONS</b>		163

## LIST OF TABLES

		<b>Page</b>
Table 2.1	List of pollutants degraded by photocatalysis.	16
Table 2.2	BiOBr at nanoscale and hierarchical micro/nanostructures on the photocatalytic degradation of organic dyes.	25
Table 2.3	Effect of catalyst loading on the photocatalytic degradation of various organic dye.	31
Table 2.4	Effect of initial dye concentration on the photocatalytic degradation of various organic dye.	35
Table 2.5	Effect of solution pH on the photocatalytic degradation of various organic dyes.	38
Table 3.1	List of chemical and other materials	48
Table 3.2	The coded and actual values of the design factors	61
Table 3.3	Experiment design matrix for optimization of SSY degradation.	62
Table 4.1	Reaction order and rate law for a reaction involving a single reactant (Gaya, 2014).	101
Table 4.2	Table of rate constants ( $k$ ) and correlation coefficient ( $R^2$ ) obtained from different reaction order graphs.	104
Table 4.3	Value of $k$ and $R^2$ under different solution pH.	107
Table 4.4	Experiment matrix and the response values.	109
Table 4.5	Analyses for model fitting.	110
Table 4.6	ANOVA for the quadratic model for SSY degradation.	111
Table 4.7	Factors and their desired goal for optimizing SSY degradation.	121
Table 4.8	Experimental solution as given by the software.	122
Table A1	BET surface area of flower-like BiOBr and BiOBr nanosheets.	161

## LIST OF FIGURES

		<b>Page</b>
Figure 2.1	Chemical structure of SSY (Harp and Barrows, 2015)	10
Figure 2.2	The basic mechanism of heterogeneous photocatalysis (Saadati et al., 2016; Bora and Mewada, 2017).	14
Figure 2.3	Structured morphologies: (a) 1D nanobelt; (b) 2D nanoflakes; (c) 2D nanosheet; (d) four-leaf clover-shape BiOBr; (e) 3D flower-like BiOBr and (f) 3D microspheres.	22
Figure 2.4	Response surface plot as presented by the Design-Expert software, (version 6, StatEase, Inc., USA).	44
Figure 3.1	Flow Chart of the Overall Methodology.	47
Figure 3.2	Flow Chart of synthesis route of flower-like BiOBr hierarchical structures.	50
Figure 3.3	Flow Chart of synthesis route of BiOBr nanosheets (adopted from Jiang et al., 2010).	52
Figure 3.4	Schematic Diagram of the Photocatalytic Degradation Reaction System.	56
Figure 4.1	XRD pattern of as-synthesized flower-like BiOBr hierarchical structures.	63
Figure 4.2	EDX spectrum of as-synthesized flower-like BiOBr hierarchical structures. The <i>inset</i> show element composition of as-synthesized BiOBr.	65
Figure 4.3	FESEM images of as-synthesized flower-like BiOBr hierarchical structures at different magnifications: (a) 1500X, (b) 10000X, (c) 20000X and (d) 40000X.	66
Figure 4.4	(a) TEM and (b) HRTEM images of the as-synthesized flower-like BiOBr hierarchical structures.	67
Figure 4.5	XPS survey spectra of as-synthesized flower-like BiOBr hierarchical structures.	68
Figure 4.6	XPS spectra of bismuth (Bi 4f) in as-synthesized flower-like BiOBr hierarchical structures.	69

Figure 4.7	XPS spectra of oxygen (O 1s) in as-synthesized flower-like BiOBr hierarchical structures	70
Figure 4.8	XPS spectra of bromine (Br 3d) in as-synthesized flower-like BiOBr hierarchical structures.	70
Figure 4.9	UV-vis DRS spectra of as-synthesized flower-like BiOBr hierarchical structures and TiO <sub>2</sub> . The <i>inset</i> shows the plot of R% versus photon energy	71
Figure 4.10	Schematic illustration of the formation process of flower-like BiOBr hierarchical structures.	73
Figure 4.11	Control experiments and photocatalytic degradation of SSY over different types of photocatalysts. Conditions: catalyst loading= 1.00 g/L, initial dye concentration= 10 ppm, solution pH= natural pH of SSY.	74
Figure 4.12	Photocatalytic degradation of SSY over flower-like BiOBr hierarchical structures in the absence and presence of scavengers under fluorescent light irradiation for 180 min. Condition: catalyst loading= 1.00 g/L, initial SSY concentration= 10 ppm, solution pH= natural pH of SSY and scavenger concentration= 0.5 mmol.	79
Figure 4.13	PL spectra changing with irradiation time over the flower-like BiOBr hierarchical structures	82
Figure 4.14	PL spectra of TA with an excitation at 315 nm for as-synthesized flower-like BiOBr hierarchical structures, BiOBr nanosheets and TiO <sub>2</sub>	83
Figure 4.15	Effect of BiOBr loading on the photocatalytic degradation of SSY over flower-like BiOBr hierarchical structures. Conditions: initial SSY concentration= 10 ppm, solution pH= natural pH of SSY and irradiation time= 180 min.	87
Figure 4.16	Effect of initial SSY concentration on the photocatalytic degradation of SSY over flower-like	89



	BiOBr hierarchical structures. Conditions: BiOBr loading= 1.00 g/L, solution pH= natural pH of SSY and irradiation time= 180 min.	
Figure 4.17	Effect of solution pH on the photocatalytic degradation of SSY over flower-like BiOBr hierarchical structures. Conditions: BiOBr loading= 1.00 g/L, initial SSY concentration= 10 ppm and irradiation time= 180 min.	92
Figure 4.18	Effect of different anions on the photocatalytic degradation of SSY over flower-like BiOBr hierarchical structures. Conditions: BiOBr loading= 1.00g/L, initial SSY concentration= 10 ppm, solution pH= pH 3 and irradiation time= 180 min.	95
Figure 4.19	Reusability efficiency of flower-like BiOBr hierarchical structures. Conditions: BiOBr loading= 1.00 g/L, SSY concentration= 10 ppm, solution pH= pH 3.0 and irradiation time= 180 min.	99
Figure 4.20	Fitting for zero-order reaction. Conditions: BiOBr loading= 1.00 g/L, SSY concentration= 10 ppm and solution pH= pH 3.0.	102
Figure 4.21	Fitting for first-order reaction. Conditions: BiOBr loading= 1.00 g/L, SSY concentration= 10 ppm and solution pH= pH 3.0.	103
Figure 4.22	Fitting for second-order reaction. Conditions: BiOBr loading= 1.00 g/L, SSY concentration= 10 ppm and solution pH= pH 3.0.	103
Figure 4.23	Fitting for third-order reaction. Conditions: BiOBr loading= 1.00 g/L, SSY concentration= 10 ppm and solution pH= pH 3.0.	104
Figure 4.24	Plots of $\ln C_{SSY_0}/C_{SSY}$ versus time for SSY degradation under different solution pH. Conditions: BiOBr	107

	loading= 1.00 g/L and initial SSY concentration= 10 ppm.	
Figure 4.25	3D surface plot indicating the effect of catalyst loading and solution pH on the percentage of SSY degradation at constant initial SSY concentration and fluorescent light irradiation time.	113
Figure 4.26	3D surface plot indicating the effect of initial SSY concentration and catalyst loading on the percentage of SSY degradation at constant solution pH and fluorescent light irradiation time.	114
Figure 4.27	3D surface plot indicating the effect of initial SSY concentration and solution pH on the percentage of SSY degradation at constant BiOBr loading and fluorescent light irradiation time.	116
Figure 4.28	3D surface plot indicating the effect of BiOBr loading and fluorescent light irradiation time on the percentage of SSY degradation at constant initial SSY concentration and solution pH.	117
Figure 4.29	3D surface plot indicating the effect of initial SSY concentration and fluorescent light irradiation time on the percentage of SSY degradation at constant BiOBr loading and solution pH.	118
Figure 4.30	3D surface plot indicating the effect of solution pH and fluorescent light irradiation time on the percentage of SSY degradation at constant BiOBr loading and initial SSY concentration.	120
Figure 4.31	Photocatalytic degradation of SSY over flower-like BiOBr and BiOBr nanosheets under solar irradiation. Conditions: BiOBr loading= 1.30 g/L, initial SSY concentration= 10 ppm, solution pH= pH 3.0 and irradiation time= 180 min.	123

Figure A1 FESEM images for BiOBr nanosheet at different 160  
magnification (a) 20000X and (b) 50000X.

Figure A2 N<sub>2</sub> adsorption-desorption analysis of flower-like 161  
BiOBr and BiOBr nanosheet.

## LIST OF SYMBOLS

Symbol	Description	Unit
$C_0$	Concentration of dye after 30 min of dark run	ppm
$C_t$	Concentration of dye at reaction time t	ppm
$C_{SSY0}$	Initial concentration of SSY	ppm
$C_{SSY}$	Concentration of SSY at time t	ppm
$dC_{SSY}/dt$	Differential of $C_{SSY}$ with respect to time t	ppm/min
$e^-$	Photon generated electron on the photocatalyst	-
$h^+$	Photon generated hole on the photocatalyst	-
$h\nu$	light	-
$k$	Observed rate constant	ppm/min
$k_{app}$	Apparent rate constant for first order equation	1/min
K	Adsorption equilibrium of SSY	1/ppm
$OH^-$	Hydroxide ion	-
$\bullet OH$	Hydroxyl radical	-
$-r$	Reaction rate	ppm/min
$R^2$	Correlation coefficient	-
t	Time	min
$\lambda$	Wavelength of fluorescent light	nm

## LIST OF ABBREVIATIONS

AC	Activated carbon
ANOVA	Analysis of variances
AOPs	Advanced oxidation processes
ADI	Acceptable daily intake
BET	Brunauer-Emmett-Teller
BOD	Biochemical oxygen demand
CB	Covalent band
CCD	Central composite design
CdS	Cadmium sulfide
CO <sub>2</sub>	Carbon dioxide
COD	Chemical oxygen demand
DG	Direct green
DOE	Design of experiments
EDX	Energy dispersive X-ray spectroscopy
Fe	Iron
HCl	Hydrochloric acid
H <sub>2</sub> SO <sub>4</sub>	Sulphuric acid
H <sub>2</sub> O	Water
H <sub>2</sub> O <sub>2</sub>	Hydrogen peroxide
KI	Potassium iodide
MB	Methylene blue
MG	Malachite green
MO	Methyl orange

MRGO	Magnetically reduced graphene oxide
NaOH	Sodium hydroxide
O <sub>2</sub>	Oxygen
PL	Photoluminescence
RB 5	Reactive black 5
RB 198	Reactive blue 198
RY 145	Reactive yellow 145
RhB	Rhodamine B
RSM	Responses Surface Methodology
SSY	Sunset Yellow
TA	Terephthalic acid
TAOH	2-hydroxyterephthalic acid
TiO <sub>2</sub>	Titanium dioxide
UV	Ultraviolet
ZnO	Zinc oxide

# CHAPTER ONE

## INTRODUCTION

### 1.1 BACKGROUND OF STUDY

Water is an important part for every living thing and transfigured through widespread land cover change, industrialization and urbanization as well as engineering schemes such as irrigation and reservoirs that maximized human access to water (Vörösmarty et al, 2010). The water cycle had been interrupted by humans by dams for water preserving and discharging water for industrial, agricultural, and domestic purposes. Besides that, gradually climate change is anticipated to affect the water supply and demand. (Haddelanda, et al, 2013). Furthermore, for the past two decades, the mass growing of industrial activities and agricultural productions have resulted the contaminated of natural water by various hazardous chemical substances such as dyes, phenols, pesticides, solvents and other organic pollutants existing in various natural resources (Sin et al, 2013).

$7 \times 10^5$  tones of organic dyes have been reported to be produced yearly and 10-15% was flowed into wastewater treatment during manufacturing and application processes (Lam et al., 2012). Besides, wastewater from dye manufacturing consists of unreasonable chemical oxygen demand (COD), strong colour, outrageous of total dissolved solids (TDS) content and various pH value. Moreover, intermediates of dyes in wastewater can be carcinogenic or mutagenic, which threatened the ecosystem of aquatic life and microorganism.

The elimination of anthropogenic and carcinogenic azo dyes is considered as one of the main concerns in the environment remediation. Many physiochemical processes such as reverse osmosis, flocculation, coagulation, activated carbon adsorption, Fenton process and electrochemical oxidation had been used to degrade azo dyes from textile water (Sarkar et al, 2017). However, the applications had their limitations, such as the over usage of chemicals led to sludge generation with further treatment problem, costly installation as well as operating costs and sensitivity towards variability in wastewater input (Balapure et al, 2014). In addition to physiochemical method, biological treatments via algae, fungi, bacterial and yeast are commonly used to degrade certain type of dyes. In comparison to physiochemical method, biological methods are relatively environmental friendly, less sludge generated and low cost but biological applications required a large land area for reactivity, has sensitivity toward toxicity of certain chemicals and requires longer treatment time (Brillas and Huitle, 2014).

Furthermore, most of the azo dyes contained complex aromatic molecular structure and toxicity of azo dyes making them to be non-biodegradable (Sarkar, 2017). Li et al. (2016) stated that electro-fenton reaction is a classical advanced oxidation process which is also an efficient method for azo dyes wastewater treatment but it has a short catalyst lifespan, high cost of electrode materials and high consumption of energy limiting the industrial application. Moreover, physical process such as membrane technology led to phase transfer of dye and no destruction which does not resolve the full problem as the adsorbent material needed to be regenerated and adsorbed azo dyes have to undergo further treatment (Chengalroyen and Dabbs, 2012; Popli and Patel.,



2014). Chemical processes are rapid but the addition of large quantities of expensive chemicals into the effluent resulted to the yield of secondary pollution or hazardous sludge products that tends to accumulate in final solutions ( Brillas and Huitle., 2014; Popli and Patel, 2014; Ramrez et al, 2016). Hence, an alternative method required to be discovered for a higher efficiencies on degrading sunset yellow azo dyes.

Advanced Oxidation Processes (AOPs) using reactive radicals as major oxidizing agents are widely reported to treat different types of wastewater efficiently (Deng and Zhao, 2015). Heterogeneous photocatalysis is one of the AOPs method that hugely involved in environmental and energy related sectors. The photocatalytic properties of certain materials such as  $\text{TiO}_2$  and  $\text{ZnO}$  are used as photocatalysts to transform solar energy into chemical energy for oxidizing or reducing harmful pollutants into a more safety or useful materials (Nakata and Kujishima, 2012).  $\text{TiO}_2$  and  $\text{ZnO}$  are commonly used in photocatalysis field due to their strong oxidizing abilities for degrading organic pollutants, chemical stability, non-toxicity, long durability and low cost (Nakita and Kujisama, 2012) but they also have some limitations in them. Therefore, an alternative photocatalyst has to be applied for improving or replenishing the weakness of  $\text{TiO}_2$  and  $\text{ZnO}$ .

## **1.2 PROBLEM STATEMENT**

Sunset yellow (SSY) For Coloring Food (FCF) is a disulfonated azo dye in neutral pH (Xiao et al., 2014). It can be found in food and beverages such as orange jelly, fruit jam, soft drink, vitamin, medicinal capsule and alcoholic drinks (Warzkiewicz, 2011). Sayed et al. (2012) has conducted a study on the

cytotoxicity of SSY. Their results showed that SSY can cause mutagenic action in mice and gave a significantly chromosomal aberration in the germative and liver cells, DNA fragmentation as well as abnormal morphologies spermatozoid in animals. SSY also can lead to vasculitis, anaphylactic shock, angioedema as well as thromboxane synthesis inhibition in people sensitive to its composition (Gomes, 2013). Besides, SSY also led to genotoxicity in murine models with memory and learning deficits as well as immunomodulatory and xenoestrogenic effects (Carocho et al., 2014). Therefore, the awareness on the negative effect of SSY should be raised and immediate action should be taken on degradation of SSY.

TiO<sub>2</sub> and ZnO are the most used semiconductor materials in photocatalysis industry due to their high resistance to corrosion process, innocuous character and excellent photocatalytic activity (Cuellar et al., 2015). Nevertheless, the large band gap of TiO<sub>2</sub> (~3.2 eV) and ZnO (~3.3 eV) are only active in the UV region, which represented that only small portion (4-5%) of solar radiation and the recombination of photogenerated electrons and holes is very fast. This can lead to the slower rate of electrons and holes reaching the surface of the semiconductor for redox reactions. (Lam et al., 2012; He et al., 2014; Zhu et al., 2015). Therefore, an alternative materials, bismuth oxybromide (BiOBr) can be employed to substitute the TiO<sub>2</sub> and ZnO. BiOBr has an appropriate band gap (~2.8 eV) which is relatively narrower than TiO<sub>2</sub> and ZnO (He et al., 2014). With narrower band gap, BiOBr can absorb the light in visible region of sunlight and can be promising in sunlight photocatalysis. The intrinsic layered BiOBr structure also provided BiOBr with well separation efficiency of

photogenerated electron-hole pairs, leading to an enhancement of photocatalytic performance.

Every unique dimension and morphology of photocatalysts contributed to different properties for their performance especially the surface area of photocatalyst played a significant role due to the photocatalytic reactions normally happened at the interface between the organic pollutants and catalyst surfaces. The nanoscale semiconductors have shown larger specific surface area for photocatalytic reactions. Nevertheless, it should be revealed that low dimensional nanoscaled building blocks (such as nanorods, nanoparticles and nanoplates) can easily aggregate and resulted in decreased surface area as well as lower degradation efficiency (Li et al., 2015). Nowadays, three-dimensional (3D) hierarchical BiOBr structures that are fabricated from low dimensional nanoscaled building blocks have garnered significant attentions. Ren et al. (2014) reported that 3D flower-like microspheres that are build up with low dimensional structures have a higher degradation efficiencies on organic pollutants. This was due to the hierarchical architecture of catalysts had higher surface area and helped in transportation of photo-generated charge carriers. Hence, a flower-like hierarchical BiOBr photocatalyst was synthesized in this study to enhance the dye degradation efficiency.

### **1.3 OBJECTIVES**

In this study, photocatalytic system equipped with fluorescent light was operated to investigate the SSY degradation. The chosen operational parameters for instance catalyst loading, initial dye concentration and solution pH were optimized via conventional one-factor-at-a-time technique as well as response

surface methodology (RSM). The objectives on SSY degradation over flower-like BiOBr hierarchical structures are stated as follows:

1. To synthesize flower-like BiOBr hierarchical structure photocatalysts using a hydrothermal route.
2. To characterize the physical, chemical and optical properties of the as-prepared photocatalysts.
3. To investigate the photocatalytic performance of the synthesized photocatalysts on the photodegradation of SSY under fluorescent light and sunlight irradiation.
4. To perform the effect of operating parameters as well as kinetic studies on the photocatalytic degradation of SSY over the as-synthesized photocatalysts.
5. To obtain optimum operating parameters by response surface methodology.

#### **1.4 SCOPE OF STUDY**

This research mainly focused on the 3D flower-like BiOBr hierarchical structures on the photocatalytic degradation of SSY. 3D flower-like BiOBr photocatalysts are characterized by using analytical instruments which include X-ray diffraction (XRD), field emission scanning electron microscopy (FESEM), energy dispersive X-ray (EDX), transmission electron microscopy (TEM), high resolution transmission electron microscopy (HRTEM), X-ray photoelectron spectroscopy (XPS), N<sub>2</sub> adsorption-desorption isotherm analysis and UV-vis diffuse reflectance spectroscopy (UV-vis DRS). The degradation performance of the as-synthesized BiOBr has also been recorded and studied. Throughout the

research, the operating variables such as effects of catalyst loading, initial SSY concentration, solution pH and inorganic anion are studied. Every chosen operating variables are based on the variables outlined in the literature and via the process of trials and error. The reusability and active species of BiOBr are also investigated in this research. Moreover, Langmuir-Hinshelwood equation were fitted into the obtained result for a kinetic study. Finally, the Design of Experiment (DOE) from Design Expert is also applied to optimize the photocatalytic degradation of SSY over as-synthesized BiOBr photocatalysts. The selected variables are the catalysts loading (0.50 g/L – 2.00 g/L), initial SSY concentration (10ppm-50ppm), solution pH (pH 3.0- pH 9.0) and irradiation duration (60 min- 180 min).

## **1.5 ORGANIZATION OF THESIS**

This thesis is made up of total five chapters that covered important details and information of this research.

Chapter 1 started with the introduction on water pollution and followed by the limitation of traditional method on wastewater treatment. Then the introductory of Advanced Oxidation Process (AOP). Next, the hazardous of SSY, limitation of commercial photocatalysts and the structure of photocatalyst affecting performance of photocatalyst were mentioned. Lastly, the objectives and scope of this study were stated.

Chapter 2 consisted of the literature reviews related to this research. This chapter discussed the targeted pollutants, background of AOPs, basic mechanism and purpose of heterogeneous photocatalysis, fundamental and application of BiOBr, reports on BiOBr structure affecting the photocatalytic

performance and application of BiOBr on various dye. Lastly, the optimization of photocatalytic activity of BiOBr by previous studies were presented.

Chapter 3 outlined the detailed synthesis route of BiOBr, followed by characterization methods to study the chemical, physical and optical properties of the synthesized photocatalysts. The experimental setup and conditions adopted for the degradation of SSY and the analyses were elaborated in final part of this chapter.

Chapter 4 discussed the outcome of the research finding. This chapter clarified the characterization results such as XRD, EDX, FESEM, TEM, HRTEM, XPS and UV-vis DRS of chosen photocatalysts. Besides, the photocatalytic performance on targeted organic pollutant over selected photocatalysts were also discussed. Moreover, this chapter also endowed the effect of parameters for the optimized condition and its mechanism were presented.

Chapter 5 furnished the conclusions and recommendation towards this study.

## **CHAPTER TWO**

### **LITERATURE REVIEW**

#### **2.1 SUNSET YELLOW**

Azo dyes are chemical compounds when a diazotized amine (-N=N-) coupled to an amine or phenol which provided colours under a low concentration (Singh et al., 2015; Chung, 2016). According to Balapure et al. (2014), more than 10,000 dyes were known and amongst them azo dyes were the largest class of synthetic dyes used in numerous industries such as textile, paper, printing, leather, food and cosmetic industries. More than 40000 metric tonnes of dye stuffs were produced worldwide per annual and have been reported to be discharged into the environment which can cause water pollution, and threatened the environmental balance (Julkapli et al., 2014; Alkaim et al., 2014). In addition, the uncontrollable discharge of dyes can increase the chemical oxygen demand (COD) and biological oxygen demand (BOD) in the water by changing pH as well as altered organic-inorganic chemical contents of natural water reservoir (Sarkar et al, 2017). The toxicity and carcinogenic of azo dyes can affect the aquatic ecosystem because the colour of azo dyes can block the light penetration and oxygen consumption (Singh et al, 2015; Sarkar et al, 2017).

Sunset yellow (SSY) is a mono-azo dye which widely added to food products such as candies, snacks, juices, jellies and soft drinks in order to provide yellow-orange colouring (Vasques, 2014; Chung, 2016). In 2013, Ministry of

Health Malaysia had found a case regarding contamination of SSY on chicken meat products which resembled chicken to deceive consumers (Rovina et al, 2016). Figure 2.1 shows the chemical structure of SSY.

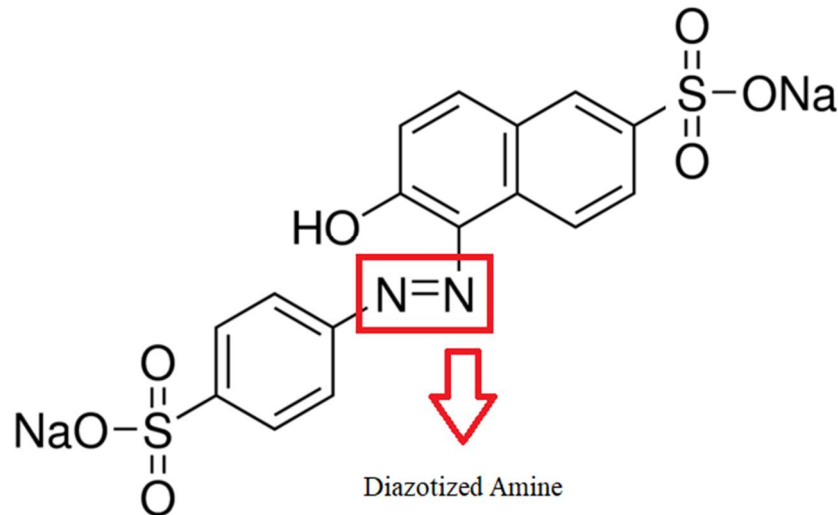


Figure 2.1: Chemical structure of SSY (Harp and Barrows, 2015)

Excess intake of SSY may cause allergies, respiratory problems, thyroid tumours, chromosomal damage, urticarial, hyperactivity and abdominal pain (Rovina et al, 2016). According to Chao and Ma (2014), overdose of SSY intake can cause allergic and intolerance reaction, particularly among asthmatics and people with aspirin intolerance. Besides, SSY also exhibited genotoxic effects to human and animals which led to abnormalities of sperm morphologies and DNA fragmentation (Pandir, 2014). Jain and Mathur (2015) also found out that the consumption of more than 2.5 mg/kg body weight/ day of SSY can lead to diarrhoea and weight reduction. The overdosing of SSY can also disrupt the supportive role of Sertoli cells, infertility of spermatogonia or spermatocytes and reduced sperm output (Mahfouz and Moussa, 2015). Moreover, Bhattacharjee



(2014) found out that SSY that widely use in food and beverage products had a strong mitodepressive effect on *Allium sativum* root tip cells. Hence, Joint PAO/WHO Expert Committee on Food Additives (JECFA) had set Acceptable Daily Intake (ADI) for average consumers which was 1.5-2.25 mg/kg body weight/day in every food products involving addition of SSY (Jain and Mathur, 2015; Dwivedi and Kumar, 2015).

## **2.2 ADVANCED OXIDATION PROCESSES (AOPs)**

Advanced oxidation processes (AOPs) are considered as greener and sustainable disinfection technologies for the remediation of water contaminated with organic pollutants. The AOPs reactions depended on the formation active radicals which can oxidize the organic pollutants into CO<sub>2</sub>, H<sub>2</sub>O and inorganic ions as desired end-products (Antonopoulou et al., 2013; Ribeiro et al., 2014). When the pollutants underwent the oxidation process, the intermediate products can be completely mineralized and secondary treatment is not needed (Ribeiro et al., 2014). The fast reaction rates and non-selective oxidation allowed the remediation of multiple contaminants simultaneously as well as ultimate mineralization properties have made AOPs became famous decontamination methods studied by many researchers (Antonopoulou et al., 2013; Cheng et al., 2015; Giannakis et al., 2017).

Common AOPs have been widely reported to employ in dye water treatment processes from different industries. Sohrabi et al. (2014) investigated the removal of Carmoisine edible dye from aqueous solution by AOPs. The results of their study work demonstrated high efficient removal (92.7%) of Carmoisine by AOPs. Besides, AOPs were applied by Hassaan et al. (2016) to

degrade mordant violet 40 dye in freshwater and seawater. They found out that the AOPs able to degrade 98% of mordant violet 40 and lowered the toxicity of mordant violet 40 under UV light irradiation. The research of degradation on reactive black 5 (RB5) and setazol black DPT was done by Bilińska et al. (2016). Almost completely colour removal was achieved and chemical oxygen demand (COD) decreased by employing AOPs.

The AOPs also showed good effectiveness as single stage for treatment of winery wastewater in Portugal (Souza et al., 2013). Besides, AOPs were merged with conventional biological process which can improve the removal of both organic materials and recalcitrant compounds (Naddeo, 2013). AOPs were also employed to degrade two materials that produce earthy and musty odour in drinking water which were 2-methylisobomeol (MIB) and geosmin (GSM) (Antonopoulou et al., 2014). Applications of AOPs also successfully removed polycyclic aromatic hydrocarbon, polychlorinated biphenyls and total petroleum hydrocarbon from contaminated soils (Cheng et al., 2016). Lastly, the AOPs showed promising efficiency for detoxification of dyes wastewater and effectively removed micropollutant from hospital wastewater treatment in Switzerland (Iqbal and Bhatti, 2014; Glamnakis et al., 2017). Thus, AOPs had their versatility which able to be employed in various type of decontamination processes.

### **2.3 HETEROGENEOUS PHOTOCATALYSIS**

From IUPAC Gold Book, photocatalysis is explained as the change in the rate of a chemical reaction or its initiation under the light radiation in the presence of a photocatalyst that absorbed light and involved in the chemical

transformation of the reaction partners (Byrne et al., 2015; Saravanan et al., 2017). Heterogeneous photocatalysis is one of AOPs that discovered by Fujishima and Honda in 1970s who used  $\text{TiO}_2$  as a photocatalyst to split water into  $\text{H}_2$  and  $\text{O}_2$  under ultraviolet light irradiation. There are several advantages of heterogeneous photocatalysis. One of the major advantages is the potential of utilizing sunlight for various applications such as pollutants degradation, chemical transformation and clean energy production (Xiao et al., 2015). Moreover, the reaction of heterogeneous photocatalysis happened in different phases between the catalyst itself and the medium involved which can ease the separation and reutilization of photocatalysts after the reaction completed (Acar et al., 2014). The complete mineralization characteristic led to no waste disposal problem making heterogeneous photocatalysis also became a more extraordinary compared to other conventional methods (Saravanan et al., 2017).

The photocatalysis concept is generally separated into two parts: (1) light absorption to generate excited electron-hole pairs and (2) redox reaction by the separated charge carriers (Zangeneh et al., 2014; Xiao et al., 2015; Bora and Mewada, 2017). Figure 2.2 presents the basic mechanism of heterogeneous photocatalysis.

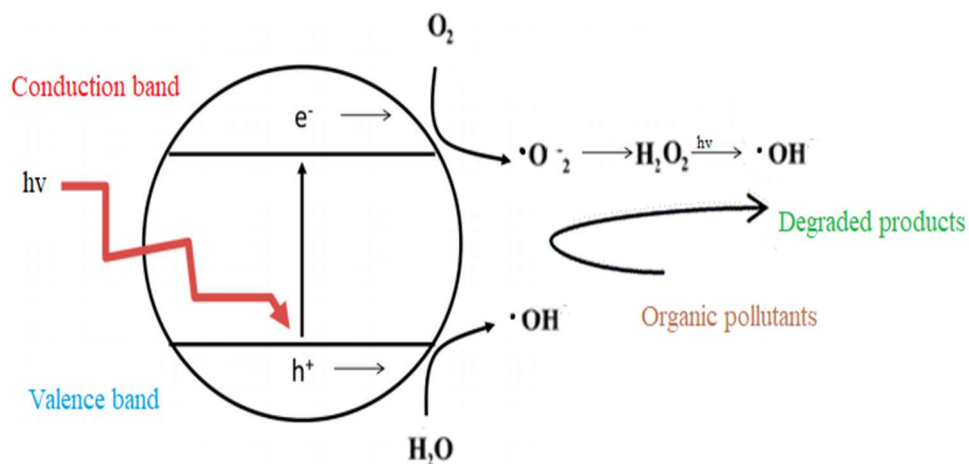
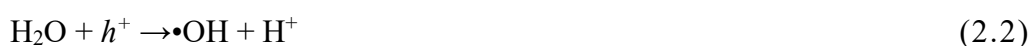


Figure 2.2: The basic mechanism of heterogeneous photocatalysis (Saadati et al., 2016; Bora and Mewada, 2017)

Figure 2.2, the photocatalytic reaction can separate into few steps: when the light ( $h\nu$ ) hit on the surface of a semiconductor with the energy of incident ray greater than or equalled to its band gap energy, the electron ( $e^-$ ) can be triggered and moved to the conduction band (CB) and leaving holes ( $h^+$ ) in the valence band (VB) of the semiconductor (Equation 2.1).

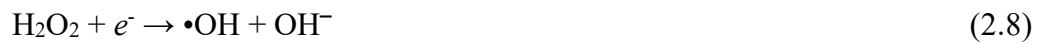


The  $h^+$  in valence band can oxidize donor molecules and reacted with water molecule ( $\text{H}_2\text{O}$ ) to generate  $\bullet\text{OH}$  as high oxidizing species for organic pollutants degradation (Equations 2.2 – 2.3).



The  $e^-$  in CB can react with oxygen species ( $\text{O}_2$ ) to generate superoxide anion radicals ( $\text{O}_2^{\bullet-}$ ) The  $\text{O}_2^{\bullet-}$  can be protonated to produce hydroperoxyl radical

(•OOH) and then converted to hydrogen peroxide (H<sub>2</sub>O<sub>2</sub>). Cleavage of H<sub>2</sub>O<sub>2</sub> by the e<sup>-</sup> further produced •OH and OH<sup>-</sup> ions (Equations 2.4 -2.8).



With the formation of active species such as •OH radicals, they can react with the organic pollutants effectively due to their main high oxidizing potential. From the above discussion, heterogeneous photocatalysis is suggested as a promising technology which has potential to employ in wastewater treatment. Table 2. 1 shows the list of pollutants degraded by photocatalysis.

Table 2.1 List of pollutants degraded by photocatalysis.

<b>Class of Organics</b>	<b>Examples</b>	<b>References</b>
Alkanes	n-alkane (C14-C17), n-decane, methane	King, et al. (2014); Miranda et al. (2014); Chen et al. (2016)
Alcohol	methanol, tert-butyl alcohol, benzyl alcohol, poly(vinyl alcohol)	Moulis and Krýsa (2015); Seddigi et al. (2015); Ouayng et al. (2016); Si et al. (2016); Su et al. (2017)
Aromatic Ring	acetone, acetaldehyde, toluene, trinitrotoluene	Bianchi et al. (2014); Guz et al. (2016)
Carboxylic Acid	fulvic acid, naphthenic acid, aliphatic carboxylic acids, linear carboxylic acid	Zhou et al. (2013); Mcqueen et al. (2016); Prakash et al. (2016); Bouhadoun et al. (2017)

Table 2.1 Continued

---

Pesticide	lindane, paraoxon, aldicarb, parathion, imidacloprid, carbofuran	Khan et al. (2016); Keihan et al. (2017); Manoharan and Samkaran (2017); Rasoulnezhad et al. (2017); Shorgoli and Shokri (2017); Dávila-jiménez et al. (2017)
Phenolic compound	Phenol, chlorophenols, dichlorophenols, phenolic hydroxyl, sinapinic acid	Elaoud et al. (2011); Al-Hamdi and Silanpää (2014); Al-Sabahi et al. (2016); Al-Kandari et al. (2017); Han et al. (2017); Khamparia and Jaspal (2017)
Dyes	methyl orange, mordant black 11, reactive red 195, dicholorophenol-indophenol (DCPIP), orange G	Bouanimba et al. (2013); Kumar et al. (2013); Miao et al. (2013); Kumar et al. (2014); Hamad et al. (2015); Shu et al. (2017); Saien and Mesgari (2017)

---

## 2.4 BISMUTH OXYBROMIDE (BiOBr) AS PHOTOCATALYST

Bismuth oxyhalides, BiOX (Cl, Br, I) compounds had attracted mass of interest in their photocatalytic activity and stability under UV and visible light irradiation. Among bismuth oxyhalides compounds, bismuth oxybromide (BiOBr) is an ideal candidate for its nontoxicity, chemical stability, relatively superior photocatalytic ability, and eco-friendly in photocatalytic reaction (Yuan et al., 2015). Particularly, BiOBr had band gap of  $\sim 2.8$  eV and active under visible light irradiation (Xue et al., 2014; Wang et al., 2014). There were the capability of BiOBr for effective separation of the photo-generated electron-hole pairs in the photocatalytic activity (Zhu et al., 2017). BiOBr with a tetragonal matlockite structure that consisted of  $[\text{Bi}_2\text{O}_2]$  positively slabs and interleaved by double slabs of Br atoms to form  $[\text{Br-Bi-O-Bi-Br}]$  layers (Li et al., 2013; Xiong et al., 2013). The intra-layers were not closely packed and connected by van der Waals forces provided the related atoms and orbitals possessed enough space to polarize (Xiong et al., 2013). This can facilitate an effective separation of photogenerated electron-holes pairs endowing BiOBr with promising potential application for photocatalytic degradation in wastewater treatment (Li et al., 2013; Xue et al., 2014).

Wang et al. (2013) investigated the photocatalytic activity of BiOBr catalyst on the degradation of methyl orange (MO) under visible light irradiation. The experimental conditions were catalyst loading = 0.80 g/L and initial concentration = 10 ppm. The photocatalytic degradation of MO reached 100% in the presence of BiOBr after 150 min irradiation. In addition, the photocatalytic experiment of BiOBr thin film on degradation of MO was conducted by Liu et al. (2013). According to their results, solvothermally synthesized BiOBr thin



film can degrade 47.2% of MO after 300 min visible light irradiation. The photodegradation of MO over hierarchical BiOBr microsphere can reach 94% after 270 min of photocatalytic experiment (Wei and Wang, 2016).

Moreover, hydrothermally synthesized four-leaf-clover-shape BiOBr synthesized by Wang et al. (2013) achieved 64% of rhodamine B (RhB) degradation after 240 min of visible light irradiation. The photocatalytic activity of the hydrothermally synthesized BiOBr nanosheets were also examined by RhB degradation under UV light irradiation. After 120 min of UV light irradiation, RhB removal over BiOBr nanosheets was 83%. Based on the obtained result, they deduced that BiOBr nanosheets displayed good photocatalytic activity under UV light irradiation. In order to test the photocatalytic degradation of RhB by BiOBr microspheres, Ahmad et al. (2016) added 1.00 g/L of BiOBr into 10 mg/L RhB aqueous solution during photocatalytic experiment. The RhB were completely removed after 120 min visible light irradiation.

The photocatalytic performance of BiOBr microspheres was investigated by Dai et al. (2014) on methylene blue (MB) degradation under UV and visible light irradiation. With the presence of BiOBr microspheres, 91% of MB was decomposed after 120 min of visible light irradiation. When the solution containing BiOBr microspheres was irradiated with UV light, 90% of MB was decomposed after 60 min irradiation. The photocatalytic activity of magnetically reduced graphene oxide-bismuth oxybromide (MRGO-BiOBr) photocatalysts was investigated via photodegradation of MB dye (Janani et al., 2015). The MRGO-BiOBr showed 76.24% of MB dye degradation after 120 visible light irradiation with the experimental parameters (catalyst loading= 0.60 g/L and

initial dye concentration= 50 ppm). The photodegradation experiments of reactive yellow 145 (RY 145), reactive black 5 (RB 5) and reactive blue 198 (RB 198) were done by Kanagaraj et al. (2017) for the sake of investigating the photocatalytic activity of BiOBr catalysts. With the presence of BiOBr catalysts, the degradation of listed dyes (RY 145, RB 5 and RB 198) achieved 80% after 90 min of visible light irradiation.

Apart from dyes, BiOBr also able to degrade other pollutants such as pesticide. Using BiOBr as photocatalysts, Peng et al. (2015) successfully degraded 70% of acetochlor under visible light irradiation for 40 hours with experimental condition of 50 ppm of acetochlor, 1.50 g/L of BiOBr loading and solution pH at 5.76. Moreover, Li et al. (2016) conducted a photocatalytic experiment on ibuprofen (IBP) over BiOBr microspheres under visible light. Approximately 80% of IBP was degraded after 120 min irradiation under a condition of BiOBr dosage at 1.00 g/L, initial IBP concentration at 0.05 mmol/L and solution pH at 7.0. From the results, BiOBr can degrade various types of organic pollutants including dyes under UV and visible light irradiation.

## **2.5 THREE DIMENSIONAL (3D) BiOBr HIERARCHICAL STRUCTURES**

Hierarchical photocatalysts are defined as the structure of semiconductors having multidimensional domains at different levels or multimodal pore structure such as one dimensional (1D) nanowires and nanorods, two dimensional (2D) nanosheets, three dimensional (3D) nanoflowers and nanosphere (Li et al., 2016; Zhao et al., 2017). The hierarchical structured

semiconductors allowed them to be promising candidates for heterogeneous photocatalysis.

Recently, hierarchical 3D structures which constructed by low dimensional structures have become ideal material in photocatalytic field. 3D hierarchical structures build up by low dimensional building block have been reported to have high surface-to-volume ratio, anti-aggregation ability and provided higher mass transfer rate of the reactants as well as products (Lee and Jang, 2014; Liu et al., 2014; Tong et al., 2015; Li et al., 2016; Chen et al., 2017). The 3D structure which was formed by oriented agglomeration of lower dimensional structures also reported to enhance the light harvesting capability by allowing more lights reflection and multiple-scattering within their structure (Jiang et al., 2014). Moreover, the assembled porous structure increased the number of light travelling and enhanced light interaction leading to faster interfacial charge separation and thus strengthened the photocatalytic efficiencies (Cheng et al., 2013; Li et al., 2015). Figure 2.3 reveals different dimensional of BiOBr photocatalysts that have been synthesized by researchers.

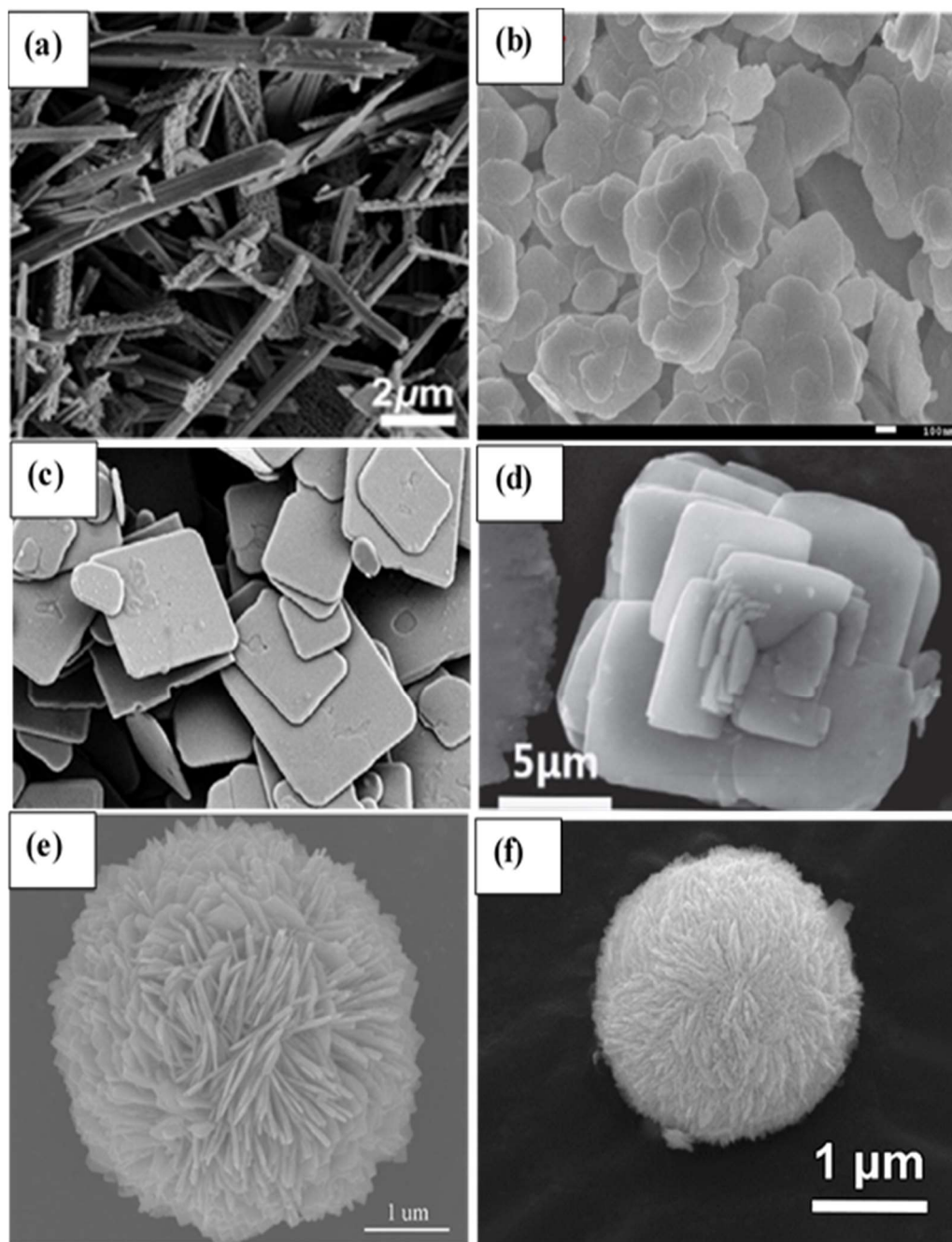


Figure 2.3 Structured morphologies: (a) 1D nanobelt; (b) 2D nanoflakes; (c) 2D nanosheet; (d) four-leaf clover-shape BiOBr; (e) 3D flower-like BiOBr and (f) 3D microspheres.

Table 2.2 shows the lists of different dimensions of BiOBr used for photocatalytic degradation of organic dyes. 1D belt-like BiOBr hierarchical nanostructure have been synthesized by Li et al. (2016) via 12 hours of solvothermal treatment. The as-synthesized BiOBr and TiO<sub>2</sub> were used to degrade MB under visible light irradiation for 240 min. As-synthesized belt-like BiOBr able to degrade 65% of MB while the degradation efficiency of TiO<sub>2</sub> reached only 23% after 240 min visible light irradiation. Using MB as pollutants, hydrothermally synthesized 2D nanoflake BiOBr exhibited degradation efficiency of 60% after irradiation of 450 min (Li et al., 2014). Moreover, Feng et al. (2015) also synthesized 2D BiOBr nanosheets by a facile hydrothermal method. The as-synthesized samples were applied for MO degradation under visible light irradiation and achieved 90% degradation efficiency after 200 min irradiation of visible light.

Since 3D hierarchical structures of BiOBr equipped with many advantages, increased research interest has been found on the application of 3D BiOBr photocatalysts to degrade different types of organic pollutants. Xiao et al. (2012) synthesized BiOBr sub-microflowers via a precipitation method and the photocatalytic properties were studied by the photodegradation of MO as well as phenol. The BiOBr sub-microflowers exhibited 97% degradation efficiency of MO and 45% of phenol decomposition efficiency under visible light irradiation. Dai et al. (2014) had conducted photocatalytic measurements of MB over hierarchical BiOBr microspheres and TiO<sub>2</sub> under visible light and UV light irradiation. They reported that 91% of MB was decomposed by BiOBr while TiO<sub>2</sub> only decomposed 17% MB after 120 min of visible light irradiation. They also reported that 90% of MB can be degraded by BiOBr with only 60 min UV

light irradiation. Moreover, solvothermally synthesized BiOBr microspheres were used to degrade anionic dye MO under simulated solar radiation and 97% of MO was decomposed after 60 min of photocatalytic reaction (Mera et al., 2017). Based on the reviews, absolute degradation efficiency on the photocatalytic degradation of various dye can be achieved by using 3D BiOBr hierarchical structures.

Table 2.2 BiOBr at nanoscale and hierarchical mirco/nanostructures on the photocatalytic degradation of organic dyes.

<b>System</b>	<b>BiOBr photocatalyst</b>	<b>Synthesized method</b>	<b>Target compound</b>	<b>Result</b>	<b>References</b>
One dimensional	Nanobelts	Solvothermal	Methylene Blue (MB)	~90% of MB was degraded after 240 min of visible light irradiation	Li et al. (2016)
Two dimensional	Thin film	Solvothermal	Methyl Orange (MO)	After 300 min of visible light irradiation 47.2% of MO was degraded.	Liu et al. (2013)
	Nanoflakes	Hydrothermal	Rhodamine Blue (RhB), Methylene Blue (MB)	~90% of RhB was degraded after 100 min of visible light irradiation ~60% of MB was degraded after 450 min of visible light irradiation	Li et al. (2014)
	Nanosheets	Hydrothermal	Methyl Orange (MO)	~ 90% of degradation obtained after 250 min visible light irradiation	Feng et al. (2015)

Table 2.2 Continued

Three dimensional structure	Flower-like	Precipitation	Methyl Orange (MO) and Phenol	97% of MO degradation achieved under visible light irradiation for 90 min 45% of phenol degraded under 240 min of visible light irradiation	Xiao et al. (2012)
		Hydrothermal	Methyl Orange (MO)	~50% of degradation obtained after 100 min of visible light irradiation	Shi et al. (2013)
	Four leaf clover shape BiOBr	Hydrothermal	Rhodamine B	The degradation efficiency of RhB reached 74 % under 240 min of visible light irradiation	Wang et al. (2013)
	Microsphere	Solvothermal	Methyl Orange (MO)	~50% of MO removal after 90 min visible light irradiation	Qin et al. (2013)



Table 2.2 Continued

Hydrothermal	Methylene Blue (MB)	~90% of MB degraded after 120 min visible light irradiation ~90% of MB decomposed under UV light irradiation for 60 min	Dai et al. (2014)
Solvothermal	Methyl Orange (MO) and Rhodamine B (RhB)	Reaching 98% MO degradation under visible light irradiation for 50 min 98% of RhB was removed within 30 min of visible light irradiation.	Wang et al. (2015)
Solvothermal	Ibuprofen	Optimum degradation was 80 % after 120 min irradiation	Li et al. (2016)
Solvothermal	Methyl orange (MO)	~90% of degradation obtained after 60 min solar radiation	Mera et al. (2017)

## 2.6 DEGRADATION OF AZO DYES OVER BiOBr

Organic azo dyes are the ordinary persistent organic pollutants which released to the environment by textile, leather, food and cosmetic industries. Besides, azo dyes can influence the quality of water leading to various negative effects like cancers and allergies. For example, reduction of azo dyes used in toys and assumed with saliva can be promoted *in vivo* by the action of intestinal anaerobic bacteria (Rajamanickam and Shanthi, 2014). Due to their toxic, mutagenic and carcinogenic effects toward living things, the employment of photocatalytic technology over different semiconductors included BiOBr is needed for environment remediation (Naik et al., 2017).

The photodegradation mechanism of MO over BiOBr was investigated by Jiang et al. (2010). Their findings showed that, the photogenerated  $h^+$  was able to oxidize the MO. They also reported that the CB edge potential of BiOBr was not negative enough to reduce the  $O_2$  molecule to the oxygen radical by the photogenerated  $e^-$ . Zhang et al. (2013) proposed that the photodegradation process of RhB can undergo two possible mechanistic pathways. One is throughout the N-de-ethylation process firstly and then the destruction of the aromatic ring while the other one was the direct breakage of the aromatic ring. Based on the colours of RhB solution study, they confirmed that the RhB degradation underwent the first pathways and the intermediate products were detected due to concentration of RhB reduced at the end of the reaction.

Deng and Guan (2013) used BiOBr for the degradation of RhB under 300 W Xe lamp irradiation with their experimental conditions of 1.00 g/L catalyst loading, 20 ppm initial RhB concentration, 100 mL solution volume and 60 min of irradiation time. The degradation efficiency of RhB was 95% after 25 min of

irradiation. Wang et al. (2013) conducted photocatalytic experiment using four-leaf clover shape BiOBr. The hydrothermally synthesized BiOBr achieved 74% degradation efficiency of RhB after 240 min light irradiation. Mera et al. (2016) also reported that 90% of photocatalytic degradation on MO over hydrothermally synthesized BiOBr nanosheets after 60 min of 12 W xenon lamp irradiation.

## **2.7 EFFECT OF OPERATING PARAMETERS**

In order to take the research to a more implementation level, optimum effects of operational parameters have to be analyzed. When a photocatalyst applied to remediate wastewater containing organic pollutants, some parameters such as catalyst loading, initial substrate concentration, solution pH and inorganic anion were necessary to be considered and optimized to achieve high photocatalytic performance (Bora and Mewada, 2017).

### **2.7.1 Effect of Catalyst Loading**

The catalyst loading is one of the significant factors during photocatalytic reaction because the efficiency can be affected by the number of active sites and photo-absorption ability of the catalyst used (Zhang et al., 2014). As catalyst loading increased, the active sites increased as well as the number photogenerated active species also increased on the catalyst surface resulting higher degradation (Zangeneh et al., 2014). Nevertheless, overdosing of catalyst can decrease the light penetration and caused light scattering effect which can reduce the photocatalytic activity of photocatalyst (Ahamd, 2013).

The effect of catalyst loading on the photocatalytic degradation of numerous organic dyes is shown in Table 2.3. Gondal et al. (2011) reported the effect of catalyst loading on the photodegradation of RhB in the presence BiOBr of photocatalyst. Their catalyst loading was varied from 0.60 g/L to 1.50 g/L while maintaining the other conditions constant (initial RhB concentration= 7 ppm and reaction time= 60 min). Their results showed that 1.20 g/L of catalyst loading exhibited the maximum removal of 94.6 % after 90 min of irradiation.

Moreover, the results obtained by Janani et al. (2015) had a good agreement with the results obtained from previous researchers. The degradation of MB increased when the MRGO-BiOBr loading increased from 0.20 g/L to 1.60 g/L. However, a decrease in the degradation of MB was observed when the catalyst loading was higher than 1.60 g/L. They explained that the more the catalyst amount, the more the availability of active sites for MB degradation. However, MRGO-BiOBr loading reached a certain value, the degradation efficiency of MB reduced because the aggregation of bulky catalyst increased the light scattering effect and reduced the light penetration.

Table 2.3 Effect of catalyst loading on the photocatalytic degradation of various organic dyes.

<b>Pollutant</b>	<b>Reaction Condition</b>	<b>Photocatalyst</b>	<b>Range</b>	<b>Optimum</b>	<b>Reference</b>
<b>Degraded</b>					
Rhodamine (RhB)	B 523 nm laser radiation; initial concentration of RhB= 7 ppm; laser energy= 131 mj; reaction time= 90 min	BiOBr nanosheets	0.60 g/L – 1.50 g/L	1.20 g/L	Gondal et al. (2011)
Methyl orange (MO)	500 W xenon light irradiation; concentration of MO= 10 ppm; volume = 50 mL irradiation time= 140 min	Flower-like BiOBr	0.40 g/L - 1.00 g/L	0.80 g/L	Wang et al. (2013)
Rhodamine (RhB)	B 250 W halide lamp irradiation; initial RhB concentration= 20 ppm; volume=250 mL; irradiation time= 60 min	CdS/BiOBr	0.40 g/L – 1.20 g/L	1.00 g/L	Cui et al. (2014)

Table 2.3 Continued

Methylene blue (MB)	150 W tungsten filament lamp	(Magnetically reduced graphene oxide) MRGO-BiOBr	0.20 g/L – 1.80 g/L	1.60 g/L	Janani et al. (2015)
	irradiation; initial MB concentration= 50 ppm; volume= 500 mL; irradiation time= 120 min				
Rhodamine B (RhB)	300 W tungsten halide lamp irradiation;	Sphere-like BiOBr	0.25 g/L – 1.50 g/L	1.00 g/L	Ahmad et al. (2016)
	initial RhB concentration= 10 ppm				

### 2.7.2 Effect of Initial Dye Concentration

Heterogeneous photocatalysis is dependent on the initial concentration of organic pollutants (Georgaki et al., 2014). This is because the concentration of targeted dye increased, a lot of dye molecules get adsorbed on the surface of the photocatalyst. Hence, the initial dye concentration can affect the photocatalytic degradation efficiency of the photocatalyst.

Rajamanickam and Shanthi (2013) stated that the chances of dye molecule to react with active species decreased at high concentrations of substrate. This was due to the catalyst amount and light intensity remained the same, resulting insufficient amount of active species for photocatalytic reaction. Moreover, abundant amount of dye molecules may compete with oxygen and  $\text{OH}^-$  on the surface of catalyst when high concentrations of dye were involved in the experiment.

The effect of initial substrate concentration towards the photocatalytic degradation of organic dyes is shown in Table 2.4. Cui et al. (2014) evaluated the effect of substrate concentration toward the photodegradation of RhB under 250 W halide lamp irradiation for 60 min. The RhB concentrations were ranged from 5 ppm to 25 ppm. The photocatalytic experiment was carried out over CdS/BiOBr and the result showed that the photocatalytic activity decreased with increasing of RhB concentration. This was attributed to the high RhB concentration can block the light penetration into the solution resulting less photons approaching the surface of catalyst and lowered down the amount of photogenerated active species. Hence, the photodegradation efficiency of RhB reduced.

An experiment was also conducted by Janani et al. (2015) to evaluate the photocatalytic performance of MRGO-BiOBr towards the MB degradation at different initial dye concentration. Similar trend of results was found where the degradation efficiency of MB decreased with the increase of initial dye concentration. According to Lv et al. (2017), the effect of initial dye concentration significantly affected the photocatalytic degradation of MB. They also found out that the photodegradation efficiency of MB reduced when initial MB concentration increased from 2 ppm to 30 ppm. Hence, they deduced that the photodegradation of MB over g-C<sub>3</sub>N<sub>4</sub>/BiOBr photocatalysts achieved optimum efficiency at low MB concentration.



Table 2.4 Effect of initial dye concentration on the photocatalytic degradation of various organic dyes.

<b>Pollutant</b>	<b>Reaction Condition</b>	<b>Photocatalyst</b>	<b>Range</b>	<b>Optimum</b>	<b>Reference</b>
<b>Degraded</b>					
Rhodamine (RhB)	B 175 W metal halide lamp; catalyst loading= 1.00 g/L; solution volume= 100 mL; irradiation time= 240 min	Four-leave clover shape BiOBr	10 ppm – 30 ppm	10 ppm	Wang et al. (2013)
Rhodamine (RhB)	B 250 W halide lamp irradiation; amount= 1.00 g/L; volume=250 mL	Cds/BiOBr	5 ppm – 25 ppm	5 ppm	Cui et al. (2014)
Methylene blue (MB)	150 W tungsten filament lamp irradiation; catalyst amount= 0.80 g/L; volume= 500 mL; irradiation time= 120 min	MRGO-BiOBr	25 ppm – 150 ppm	25 ppm	Janani et al. (2015)
Congo red (CR)	300 Xenon lamp irradiation; catalyst loading= 1.00 g/L; solution pH= 7; volume= 30 mL; irradiation time= 250 min	BiOBr/CoFe <sub>2</sub> O <sub>4</sub>	5 ppm – 35 ppm	5 ppm	Jiang et al. (2015)

Table 2.4 Continued

---

Methylene blue (MB)	50W 410 nm LED light irradiation; catalyst loading= 1.00 g/L; volume= 30 ml; irradiation time= 40 min	g-C <sub>3</sub> N <sub>4</sub> /BiOBr	2 ppm – 30 ppm	2 ppm	Lv et al. (2017)
---------------------	-------------------------------------------------------------------------------------------------------	----------------------------------------	----------------	-------	------------------

---

### 2.7.3 Effect of Solution pH

The wastewater from different industries had different pH values, thus it is one of important variables that can affect the photocatalytic degradation efficiency. However, the verification of solution pH is very difficult as it controlled the surface charge properties of the photocatalyst, affected the production of oxidizing agents and influenced the characteristic of dye (Felix et al., 2014; Alkam et al., 2014; Reza et al., 2015). Table 2.5 shows that effect of solution pH on the photocatalytic degradation of various organic dyes.

The influence of solution pH on the photocatalytic degradation of RhB over hierarchical BiOBr microspheres was evaluated by Chai et al. (2014). The photocatalytic activity of BiOBr microspheres increased with the decreasing of solution pH from 7.5 to 2.5. They suggested that an acidic conditions was more favourable for RhB degradation.

Besides, Mera et al. (2012) conducted the experiment on the effect of solution pH on the photodegradation of sulforhodamine MO under visible light irradiation. They found out that the degradation efficiency of MO decrease as the solution pH increase from pH 2.0 to pH 9.0. They mentioned that high degradation of MO was observed can be due to electrostatic attraction between the positively charged surface of BiOBr microspheres and the negatively charged MO.

Table 2.5 Effect of solution pH on the photocatalytic degradation of various organic dyes.

<b>Pollutant Degraded</b>	<b>Reaction Condition</b>	<b>Photocatalyst</b>	<b>Range of solution pH</b>	<b>Optimum solution pH</b>	<b>Reference</b>
Sulforhodamine (SRM)	Visible light ( $\lambda > 420$ nm) irradiation; catalyst loading= 0.15 g/L; initial dye concentration= 0.355 ppm; volume= 70 mL; irradiation time = 180 min	BiOBr nanosheets	2.0 – 9.0	2.0	Wang et al. (2012)
Rhodamine (RhB)	500 W tungsten halogen lamp irradiation; catalysts loading= 0.50 g/L; initial dye concentration= 10 ppm; volume= 100 mL; irradiation time= 60 min	BiOBr microspheres	2.5 to 7.5	2.5	Chai et al. (2014)

Table 2.5 Continued

Methyl orange (MO)	12 W xenon lamp irradiation; catalyst loading= 0.40 g/L; initial dye concentration= 10 ppm; volume= 200 mL; irradiation time= 60 min	BiOBr microspheres	2.0 – 9.0	2.0	Mera et al. (2017)
Malachite green (MG)	500 W tungsten halide light irradiation; catalyst loading= 0.10 g/L; initial dye concentration= 10 ppm; volume= 100 mL; irradiation time= 360 min	Activated carbon/BiOBr	2.0 – 11.0	7.0	Nethaji et al. (2017)
Methylene blue (MB)	50W 410 nm LED light irradiation; catalyst loading= 1.00 g/L; initial dye concentration= 10 ppm; volume= 30 ml; irradiation time= 40 min	g-C <sub>3</sub> N <sub>4</sub> /BiOBr	1.01 – 13.06	5.07	Lv et al. (2017)

The effect of initial pH was studied by Nethaji et al. (2017) using activated carbon (AC)/BiOBr composite by varying the initial solution ranged from 2 to 11. They mentioned that the zero point charge (ZPC) of AC/BiOBr composite was at pH 6.2. The surface of the composite will be positively charged when  $\text{pH} < 6.2$  and negatively charged when  $\text{pH} > 6.2$ . They also added that MG was a cationic dye and easily attracted to the surface of composite when solution  $\text{pH} > 6.2$ . The electron transfer between excited AC/BiOBr composites and the dye molecule can be enhanced. Thus, a maximum of 96% of MG degradation was observed at neutral pH.

Effect of solution pH on photocatalytic degradation of MB over  $\text{g-C}_3\text{N}_4/\text{BiOBr}$  photocatalyst also investigated by Lv et al. (2017) under condition of 50W 410 nm LED light irradiation, 1.0 g/L of catalyst loading, 10 ppm of initial dye concentration, 30 mL of solution volume, 40 min of irradiation time. The solution pH used in this experiment was varied from 1.01 to 13.06 using HCl or NaOH solution. They observed that the photocatalytic efficiency of MB increased with the increase in pH and achieved an optimum value at pH 5.07. However, when solution pH value was larger than 5.07, the photocatalytic efficiency of MB decreased significantly. This was because of the electrostatic repulsion happened between interface of negatively charged BiOBr surfaces and anionic configuration of MB.

#### **2.7.4 Effect of Inorganic Anions**

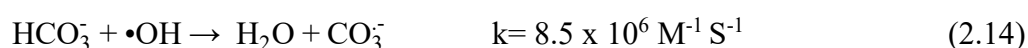
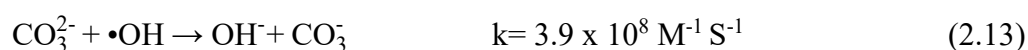
Industrial effluents usually contained different inorganic anions apart from organic matter which can interrupt the photodegradation process. (Frontistis et al., 2017). The inorganic anions can depress the photocatalytic

process by competing the active site of photocatalyst with targeted organic pollutant. Thus, the effect of inorganic anions on the photocatalytic process needs to be evaluated over the organic pollutants degradation.

Bouanimba et al. (2013) reported that the addition of inorganic anions can reduce the photodegradation efficiency of MO. The degradation of MO in the presence of NaCl, KCl, CaCl<sub>2</sub> and BaCl<sub>2</sub> were significantly reduced. The reduction of photocatalytic degradation of MO was due to the chloride ions can scavenge the positive  $h^+$  during photocatalytic degradation according to the following reaction (Equation 2.9 to Equation 2.12):



Bouanimba et al. (2013) also reported that the carbonate and bicarbonate ions significantly suppressed the MO degradation rates from 0.035 min<sup>-1</sup> to 0.01 min<sup>-1</sup> and 0.032 min<sup>-1</sup> to 0.013 min<sup>-1</sup>, respectively. They also found out that the carbonate ions have higher inhibiting effect compared to bicarbonate ions due to carbonate can react with  $\bullet\text{OH}$  with 45 times faster than bicarbonate. The explanation can be obtained from the following reaction (Equation 2.13 to Equation 2.14):



The influence of inorganic anion on the degradation of basic yellow 28 (BY 28) was also studied by Djokic et al. (2012) using sodium chloride salts. A 40% reduction in photodegradation efficiency of BY 28 was observed after 60

min of reaction time. This can be attributed to the scavenging properties of chloride ions on the  $h^+$  of photocatalysts (Djokic et al., 2012). According to Chldkov et al. (2015), anion salts such as  $Cl^-$ ,  $NO_3^-$  and  $SO_4^-$  caused a decrease in the photodegradation efficiency of reactive red 95. They mentioned that these anionic salts slowed down the oxidation rate either by blocking the active sites of the catalyst or by competing with photogenerated active species.

According to Saadati et al. (2016), the presence of some inorganic anions such as  $Cl^-$ ,  $HCO_3^-$  and persulfate ( $S_2O_8^-$ ) can decrease the degradation extent of the pollutants because those anions behaved as  $\bullet OH$  scavengers. However,  $S_2O_8^{2-}$  was an electron scavenger to produce sulphate radical anion which was a weaker oxidant compared to  $\bullet OH$  radical, hence, the photocatalytic activity affected. Besides, competitions happened between these anions and pollutant molecule to react with  $\bullet OH$  radicals which can also decrease the photocatalytic degradation of organic dyes. From the study of Gao et al. (2016), the effects of  $Cl^-$ ,  $SO_4^{2-}$ ,  $NO_3^-$  and  $HCO_3^-$  anion inhibited the photocatalytic degradation of RhB over  $BiPO_4/BiOBr$  with the order of  $HCO_3^- > NO_3^- > SO_4^{2-} > Cl^-$ . The phenomena was attributed to these anions can behave as scavengers and hence the photodegradation was inhibited.



## 2.8 RESPONSE SURFACE METHODOLOGY (RSM)

The photocatalytic degradation efficiency relies on various number of factors such as initial concentration of pollutant, photocatalyst loading, solution pH and irradiation time which monitor the performance of photocatalysis. The involve of various influencing factors can increase the difficulties to evaluate the related factors especially their complex interaction (Khataee et al., 2011). The traditional one-factor-at-a-time method is popularly used to evaluate the optimization of operating parameters on photocatalytic degradation. However, this analytical method do not take into account the interaction within various factors and this technique also time consuming (Kataee et al., 2011; Xiao et al., 2016). Central composite design (CCD) was used among various analytic methods due to CCD gave a restricted set of experiments including all probabilities based on the given factors. The CCD also enabled the evaluation of the most affecting factors in the degradation process (Khamparia and Jaspal, 2017).

CCD also known as Box-Wilson Central Composite Design which contained an imbedded factorial or fraction factorial design with centre points that is augmented with axial points that allowed estimation of curvature. In CCD, every factors are studied in five levels and the experiment number is calculated using  $N = 2^k + 2k + C_0$ , where  $k$  is the number of factors and  $C_0$  is the number of central points (Khataee et al., 2011).

For statistical calculations, the variables were coded according to the following Equation 2.15:

$$x_i = \frac{X_i - X_{i0}}{\Delta X_i} \quad (2.15)$$

Where  $x_i$  is the coded value of the  $i$  th independent variable,  $X_i$  is the natural value of the  $i$  th independent variable at centre point and  $\partial X_i$  is the step change value (Fathinia and Khataee, 2013). A second-order polynomial equation was used to fit the experimental results of CCD as follows (Equation 2.16) (Vaez et al., 2012; Fathinia and Khataee, 2013):

$$Y(\%) = b_0 + \sum b_i x_i + \sum b_{ij} x_i x_j + \sum b_{ii} x_i^2 \quad (2.16)$$

where  $Y$  denoted to the response variable (degradation efficiency);  $x_i$  and  $x_j$  are the independent variables;  $b_0$ ,  $b_i$  ( $i=1, 2$  and  $3$ ),  $b_{ii}$  and  $b_{ij}$  ( $i=1, 2$  and  $3$ ;  $j=1, 2$  and  $3$ ) are the model coefficients, respectively. The response can be represented graphically in a three dimensional plot as shown in Figure 2.4.

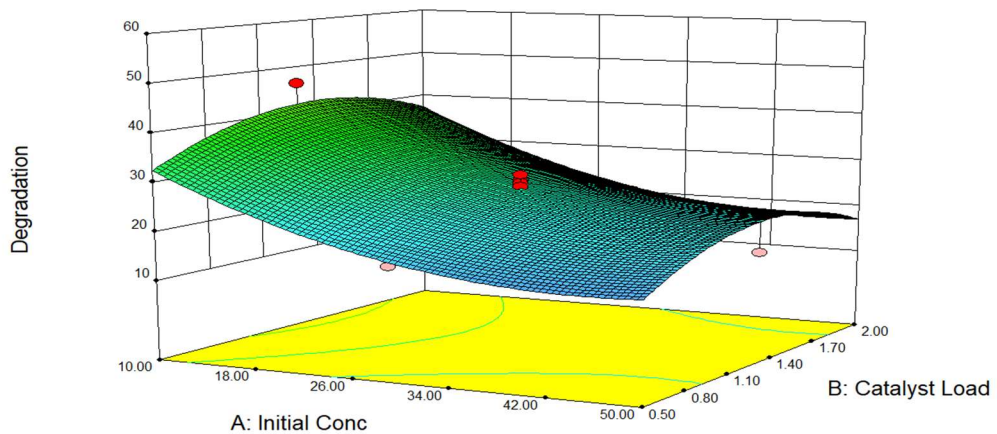


Figure 2.4 Response surface plot as presented by the Design-Expert software, (version 6, StatEase, Inc., USA).

The use of CCD based on RSM was applied by Roosta et al. (2015) to find the optimum conditions of removal of SSY in the presence of photocatalysts. They applied solution pH, catalyst loading and initial SSY concentration as the input variables to obtain the response ( $Y$ ) corresponding to the SSY residual concentration (%). In the case of the degradation of municipal wastewater, Singh

and Chaudhary (2015) employed pH, catalyst dose and amount of oxidant as the input variables while the response was the degradation percentage of wastewater.

The optimization conditions of degradation of SSY over modified photocatalysts were also investigated by Karimi et al. (2016) using CCD under RSM. They had chosen initial dye concentration, catalyst loading, pH and sonication time as independent variables. The desired response (*Y*) was the efficiency of dye removal using the as-synthesized photocatalysts. To obtain the optimum value of variables in the photocatalytic degradation of organic pollutants, Tavakoli et al. (2017) listed initial dye concentration, irradiation time, catalyst loading and solution distance from UV lamp as key factors affecting the response in RSM. CCD was also employed by Khamparia and Jaspal, 2017 to design the experiment for complex binary dye mixture decolourisation where significance of importance parameters and possible interactions were analysed by RSM. The involving key factors were irradiation time, catalyst loading and initial dye concentration while the response was the percentage of decolourisation.

## 2.9 SUMMARY OF LITERATURE REVIEW

The extensive literature review showed that although exhaustive scientific studies have been conducted on the photocatalytic degradation of various organic pollutants including dyes using BiOBr based photocatalysts. There are no studies have been conducted on the photocatalytic degradation of sunset yellow (SSY) dye over flower-like BiOBr hierarchical structures as photocatalysts. Specifically, systematic evaluation on the active species detection for the photocatalytic mechanism of flower-like BiOBr. The interest in using this photocatalyst is also due to it can be obtained in the form of flower-like with hierarchical structure. These structures enhance the efficiency of the photocatalytic system by allowing the increase of the surface area of the material. In addition, various operating variables for instance catalyst loading, initial dye concentration, solution pH and inorganic anion were involved in this study. However, all the works reported are focus in one-factor-at-a-time method and do not study the relationship of various operating variables which influencing the photocatalytic activity of BiOBr. It is necessary to standardize the experimental conditions, to obtain an optimum degradation efficiency which enables to extend the application to an industrial scale. The aim of this work is to determine the optimum values of selected variables by using a response surface methodology (RSM). These are the challenges in the BiOBr photocatalytic areas and all mention above will be determined in an attempt to overwhelm the drawbacks obtained from above review.

## CHAPTER THREE

### METHODOLOGY

#### 3.1 OVERALL FLOW CHART OF WORK

This study can be categorized into several experimental parts. The overall steps were summarised and shown in Figure 3.1.

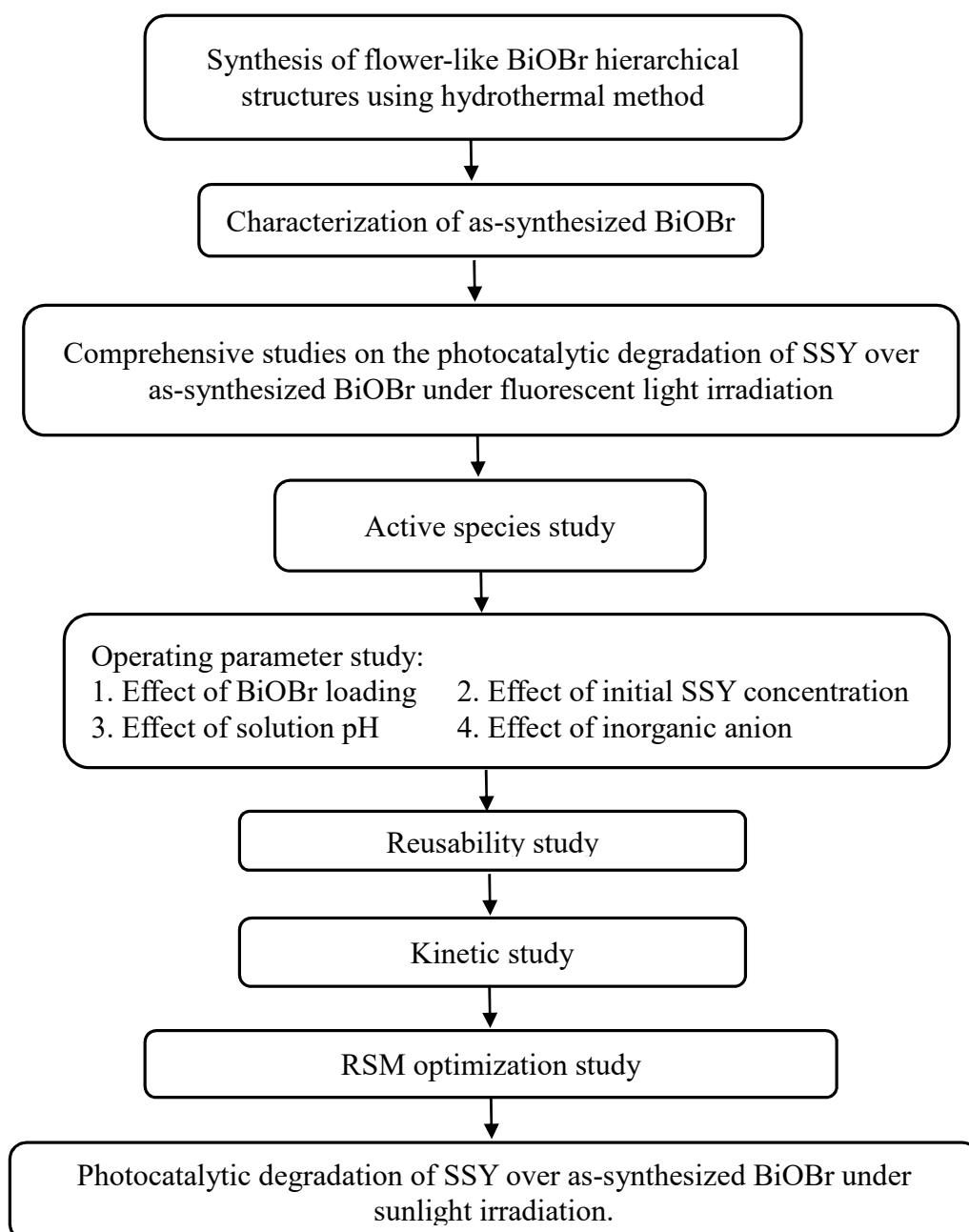


Figure 3.1 Flow Chart of the Overall Methodology.

### 3.2 LIST OF CHEMICALS AND OTHER MATERIALS

Table 3.1 lists the chemicals and materials applied in this study.

Table 3.1 List of chemical and other materials.

Chemical/Materials	Purity	Supplier	Application
Acetic Acid (CH <sub>3</sub> COOH)	99.8%	R&M Chemicals	Photocatalyst preparation
Bismuth(III) nitrate pentahydrate (Bi(NO <sub>3</sub> ) <sub>3</sub> •5H <sub>2</sub> O)	98.0%	Acros Organics	Bi precursor
Ethanol (C <sub>2</sub> H <sub>5</sub> OH)	95%	GENE Chemicals	Photocatalyst preparation
Potassium bromide (KBr)	99+%	Acros Organics	Br precursor
Potassium iodide (KI)	99.995%	Suprapur, Merck	Active species analysis
Sodium carbonate (Na <sub>2</sub> CO <sub>3</sub> )	99.5%	Acros Organic	Inorganic anion test
Sodium chloride (NaCl)	99.0%	System	Inorganic anion test
Sodium hydroxide (NaOH)	>99 %	Avantis	pH adjustment
Sodium nitrate (NaNO <sub>3</sub> )	99.0%	Bendosen	Inorganic anion test
Sodium sulphate (Na <sub>2</sub> SO <sub>4</sub> )	99.0%	System	Inorganic anion test
Sunset yellow FCF (C <sub>16</sub> H <sub>10</sub> N <sub>2</sub> Na <sub>2</sub> O <sub>7</sub> S <sub>2</sub> )	>90.0%	TCI	Model pollutant
Sulphuric acid (H <sub>2</sub> SO <sub>4</sub> )	95 -97 %	Labmedical science	pH adjustment
Terephthalic acid (TA)	≥99%	Acros Organics	Active species analysis

### **3.3 SYNTHESIS OF BiOBr PHOTOCATALYST**

#### **3.3.1 Synthesis of Flower-Like BiOBr Hierarchical Structures**

Flower-like BiOBr hierarchical structures were prepared using hydrothermal method. Firstly, 4 mmol  $\text{Bi}(\text{NO}_3)_3 \cdot 5\text{H}_2\text{O}$  was dissolved into 80 mL acetic acid ( $\text{CH}_3\text{COOH}$ ) and labelled as solution (A). On the other hand, 4 mmol KBr was dissolved into 40 mL distilled water and labelled as solution (B). Subsequently, solution A was added drop-wise into solution B under stirring. The resulting mixture was placed into a Teflon-lined stainless steel autoclave and kept at 120 °C for 12 h. The as-formed precipitates were filtrated, washed several times with distilled water and ethanol, dried at 80 °C for 8 h and eventually calcined at 400 °C for 3 h. The procedures for the synthesis of flower-like BiOBr hierarchical structures are shown in Figure 3.2:

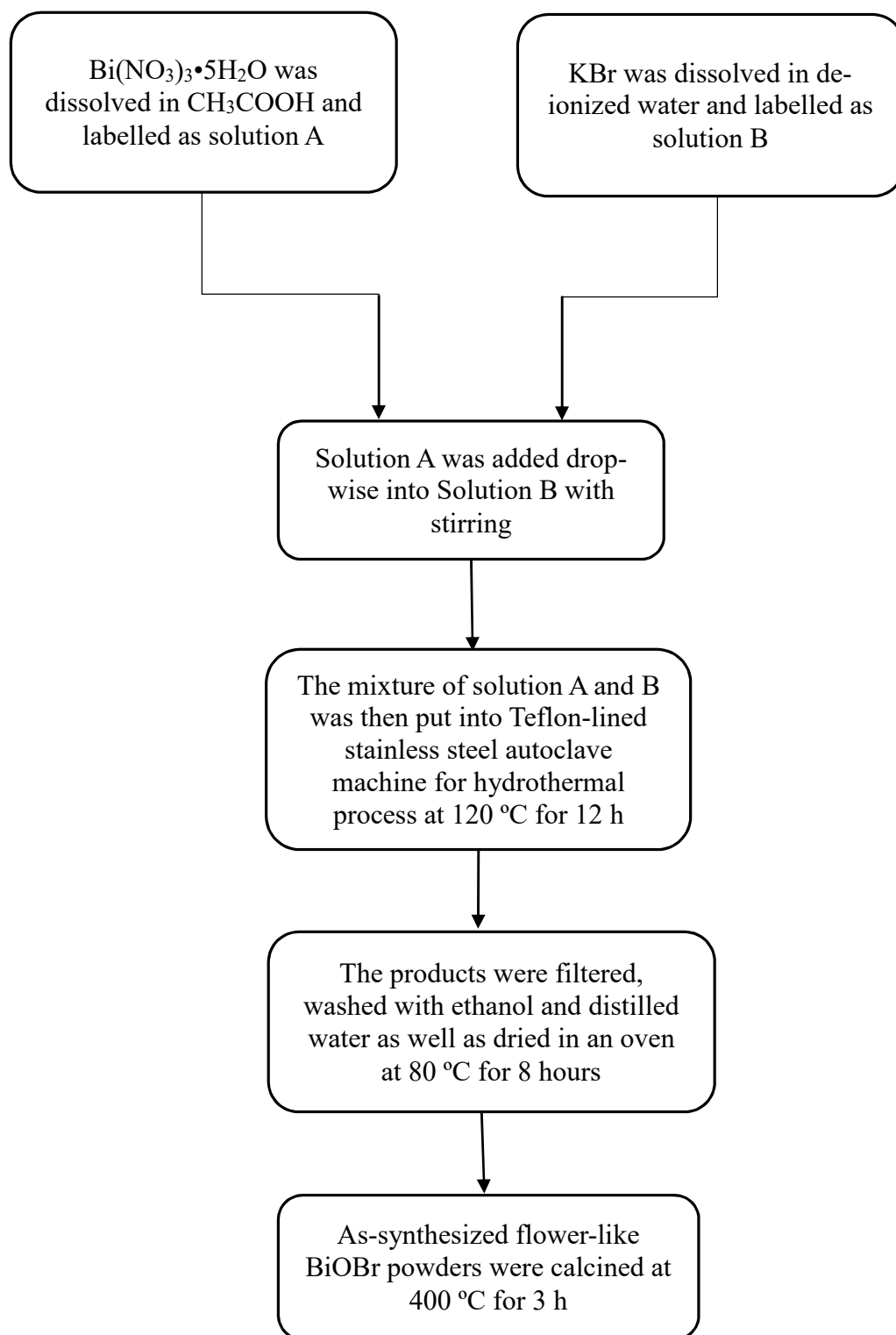


Figure 3.2 Flow Chart of synthesis route of flower-like BiOBr hierarchical structures.



### 3.3.2 Synthesis of BiOBr Nanosheets

BiOBr nanosheets were also prepared using a hydrothermal route according to Jiang et al. (2010). Firstly, 2 mmol of  $\text{Bi}(\text{NO}_3)_3 \cdot 5\text{H}_2\text{O}$  was dissolved in 3 ml acetic acid ( $\text{CH}_3\text{COOH}$ ), and the mixed solution was added to 30 ml distilled water containing 2 mmol KBr under vigorous stirring. Upon the adding of  $\text{Bi}(\text{NO}_3)_3/\text{CH}_3\text{COOH}$  solution, yellow precipitates were observed which then became light yellow as addition was completed. After stirring for 20 min at room temperature, the suspension was transferred into a Teflon-lined stainless steel autoclave and heated at the 120 °C for 24 h. The resulting precipitate was filtrated, washed thoroughly with distilled water to remove any possible ionic species in the product, and then dried at 60 °C overnight. Lastly, the dried BiOBr nanosheets were calcined at 400 °C for 3 h. Figure 3.3 demonstrated the procedures for the synthesis of 2D BiOBr nanosheets.

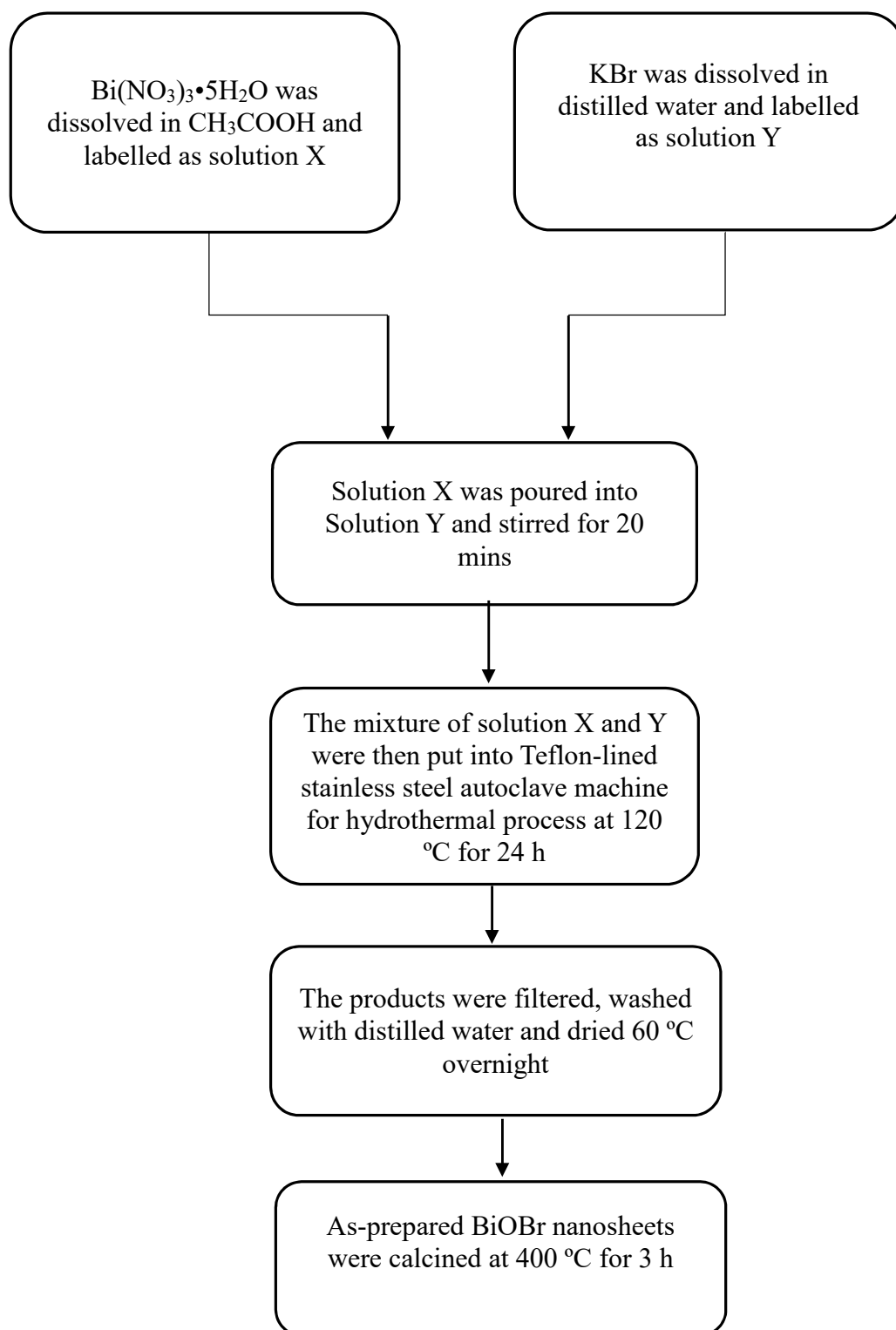


Figure 3.3 Flow Chart of synthesis route of BiOBr nanosheets (adopted from Jiang et al., 2010).

### **3.4 CHARACTERIZATION STUDIES**

#### **3.4.1 X-ray Diffraction (XRD)**

The crystal structure of the as-synthesized BiOBr products was characterized using X-ray diffraction (XRD) analysis on a Philips PW1820 diffractometer equipped with Cu K  $\alpha$  radiation. The XRD data was scanned at  $2\theta$  over a range from  $10^\circ$  to  $70^\circ$ . The analysis was carried out in the School of Materials and Mineral Resources Engineering, Universiti Sains Malaysia.

#### **3.4.2 Field-Emission Scanning Electron Microscopy (FESEM) and Energy Dispersive X-ray Spectroscopy (EDX)**

The surface morphologies of the as-synthesized BiOBr samples were inspected using JEOL JSM-6701F field-emission scanning electron microscopy (FESEM) together with the EDX analysis. A double sided carbon tape was attached on the surface of aluminium stub and the as-synthesized BiOBr powder distributed on the carbon tape evenly. The aluminium stub with sample powder were put into FESEM for scanning at different magnifications. At the same time, the surface chemical composition of the as-synthesized BiOBr powder was verified using EDX method. Both of the analyses were done in Quantum Skynet, Negeri Sembilan.

#### **3.4.3 Transmission Electron Microscopy (TEM) and High Resolution Transmission Electron Microscopy (HRTEM) Analysis**

The TEM image was obtained from Philips CM 12 instrument operating at 120 keV when the HRTEM images were taken by using Tecnai 20 microscope. In this study, TEM and HRTEM characterization were performed to further investigate the microstructure of BiOBr samples. The samples were placed into ethanol and shooked aggressively for a few minutes. Then, the suspensions were

assigned to allow to sediment. A droplet of the pre-treated samples was obtained and put onto a copper grid coated by carbon film. The samples were allowed to dry and attached the copper grid on the sample holder on the instrument for analysis. The image analyses taken from HRTEM micrographs also performed to determine the lattice fringes of as-prepared flower-like BiOBr. TEM analysis was performed in School of Biological Science, USM when the HRTEM characterization was carried out in MIMOS Berhad, Technology Park, Malaysia.

#### **3.4.4 X-ray Photoelectron Spectroscopy (XPS)**

X-ray Photoelectron Spectroscopy (XPS) is the most widely used surface analysis technique because it can be applied to a wide range of materials and provided chemical state information from the surface of the samples. In this study, XPS spectra of BiOBr powders were recorded using PHI Quantera II Physical Electronics in MIMOS Berhad, Technology Park Malaysia. Typically, the surface of samples was excited by mono-energetic Al  $K\alpha$  x-rays causing photoelectrons to be emitted from the sample surface. Then the energy of the emitted photoelectrons was measured by an electron energy analyser. By using the binding energy and photoelectron peak intensity, the elemental identity and chemical state of BiOBr powders were detected.

#### **3.4.5 UV-vis Diffuse Reflectance Spectroscopy (UV-vis DRS)**

In order to identify the optical properties of the as-synthesized BiOBr samples, the technique of UV-vis diffuse reflectance spectrum (DRS) was used. In this study, diffuse reflectance spectroscopy (DRS) of catalysts was tested in a Perkin Elmer Lambda 35 UV-vis spectrometer. The spectra were recorded at room temperature in the range of 350–700 nm using barium sulfate ( $BaSO_4$ ) as

the reference standard. The UV-vis DRS analysis was performed in School of Chemical Sciences, USM.

#### **3.4.6 Nitrogen Adsorption-Desorption Isotherm Analysis**

The information on the surface of the as-synthesized flower-like BiOBr and BiOBr nanosheets were determined by N<sub>2</sub> adsorption-desorption analysis. The N<sub>2</sub> adsorption-desorption isotherms of the photocatalysts were obtained via model ASAP 2020 Micromeritics surface area. Before the analysis, 0.20 g of samples were underwent degasification under vacuum at 300 °C. The sample was then shifted to the instrument along with liquid state N<sub>2</sub>. The result was determined through the relative pressure ( $p/p_0$ ) of N<sub>2</sub> adsorbed on surface of the sample. Furthermore, the volume of N<sub>2</sub> removed from the sample surface was obtained to measure desorption isotherm. The Brunauer-Emmett-Teller (BET) surface area were then verified from N<sub>2</sub> adsorption-desorption processes using computer software. The analyses were performed in Quantum Skynet, Negeri Sembilan.

### **3.5 PHOTOCATALYTIC EXPERIMENT SET UP**

A batch reaction system was used for the experimental set up. The photocatalysis experiments were carried out in a 250 mL beaker. A 55 W fluorescent lamp from World Lighting with a light intensity of 14500 lx was located at 14 cm above the aqueous solution of dye. An acrylic black box was employed during the experiment to prevent stray lights entering the reaction system. Subsequently, a hot plate stirrer provided by Fisher Scientific was utilized to make a satisfactory mixing of the reaction mixture with the photocatalysts. During the experiment, air was bubbled into the dye solution via

the air pump supplied by Sobo attached to a flow meter from Dwyer. Furthermore, cooling fans manufactured by Toyo were employed during the experiment for cooling purpose. The schematic illustration of the photodegradation experimental setup is shown in Figure 3.4.

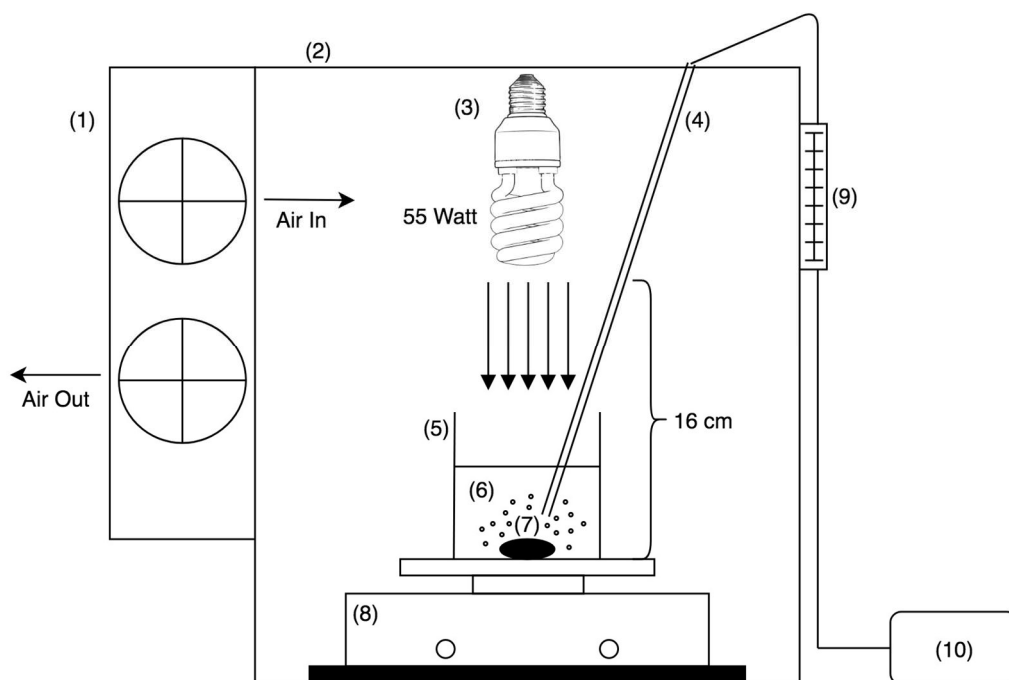


Figure 3.4 Schematic Diagram of the Photocatalytic Degradation Reaction System. (1) Cooling Blower Fans, (2) Acrylic Black Box, (3) Fluorescent Lamp, (4) Air Supply, (5) Beaker, (6) Dye Solution, (7) Magnetic bar, (8) Hot plate stirrer, (9) Flow Meter and (10) Air Pump.

### 3.6 PHOTOCATALYTIC PERFORMANCE EVALUATION

In this study, SSY was chosen as a dye pollutant for the evaluation of photocatalytic activity of flower-like BiOBr hierarchical structures. In a typical photocatalytic experiment, a desirable amount of BiOBr catalyst was dispersed in 200 mL of SSY solution. Prior to the irradiation, the solution was stirred magnetically in the dark for 30 min in order to reach the adsorption equilibrium between photocatalysts and SSY solution. After that, the light was turned on, 5

mL of suspension was withdrawn at given time interval and subjected to centrifugation. The SSY concentration was analysed via HACH DR600 UV-vis spectrophotometer at 480 nm. The photocatalytic degradation of SSY also carried out under sunlight irradiation via the similar experimental set up as mentioned exclude the fluorescent light as well as acrylic black box. The sunlight photocatalytic experiments were performed on sunny days at 11 am to 2 pm during the month of July. The light intensity was measured by lux meter, which was 73000 lux. The similar steps of retrieving samples were used and the obtained sample were analysed via UV-vis spectrophotometer. Both the photocatalytic degradation efficiencies of SSY under fluorescent light and sunlight were calculated based on Equation 3.1:

$$\text{Dye degradation (\%)} = \frac{C_0 - C_t}{C_0} \times 100 \% \quad (3.1)$$

where  $C_0$  is the dye concentration after 30 min of dark run and  $C_t$  is the dye concentration at reaction time,  $t$  (min).

### 3.7 DETECTION OF ACTIVE SPECIES

0.5 mmol of potassium iodide (KI) and ethanol ( $C_2H_6O$ ) were added as scavengers to study the role of  $h^+$  and  $\bullet OH$  radicals respectively in the photocatalytic reaction. The scavenger addition photocatalysis experiments were performed in a similar procedure to the above experiments in Section 3.6.

Furthermore, terephthalic acid photoluminescence probing technique (TA-PL) was also carried out to detect the  $\bullet OH$ . TA readily reacted with  $\bullet OH$  to produce highly fluorescent product, 2-hydroxyterephthalic acid (TAOH). The method relied on the PL signal at 425 nm of TAOH (Zhang et al., 2011; Cao et

al., 2012). The PL intensity of TAOH was corresponded to the amount of •OH radicals generated. In the TA-PL experiment, a basic TA solution was used in the reactor instead of SSY and the concentration of TA was set at  $5 \times 10^{-4}$  M in  $2 \times 10^{-3}$  M NaOH solution. The PL spectra of generated TAOH were measured by a Perkin-Elmer Lambda S55 spectrofluorometer in School of Chemical Sciences, USM. After a certain irradiation period, the reaction solution was applied to determine the PL intensity at 425 nm using provocation wavelength of 315 nm.

### **3.8 EFFECT OF OPERATING PARAMETERS**

#### **3.8.1 Effect of Catalyst Loading**

The effect of catalyst loading on the photocatalytic degradation of SSY was determined by varying the loading of flower-like BiOBr hierarchical structures from 0.25 to 2.00 g/L under fluorescent light irradiation. The selection of this catalyst loading range was referred to the literatures (Wang et al., 2012; Peng et al., 2015; Kanagaraj and Thiripuranthagan, 2017; Han et al., 2018). All the experiment runs were performed under constant initial SSY concentration of 10 ppm and natural solution pH of 6.0.

#### **3.8.2 Effect of Initial Dye Concentration**

SSY solution at different concentrations (10 ppm-60 ppm) were prepared and their effects on the photocatalytic performance of as-synthesized BiOBr powder were recorded. The range of initial dye concentration was selected based on works by Kanagaraj and Thiripuranthagam (2017) as well as Han et al. (2018).



All experiments were conducted at 1.00 g/L of catalyst loading and natural solution pH of 6.0.

### **3.8.3 Effect of Solution pH**

The effect of solution pH on the photocatalytic degradation of SSY was also examined by varying the initial pH of aqueous SSY solution from pH 3.0 to 9.0 with aqueous 0.1 M of H<sub>2</sub>SO<sub>4</sub> or NaOH solutions prior to the photocatalytic experiment. The different solution pH values were selected based on literatures (Wang et al., 2012; Kanagaraj and Thiripuranthagam, 2017; He et al., 2017; Han et al., 2018) while keeping all other experimental conditions constant (BiOBr amount of 1.00 g/L as well as SSY concentration of 10 ppm).

### **3.8.4 Effect of Inorganic Anion**

The effect of inorganic anion on the photocatalytic degradation of SSY over as-synthesized flower-like BiOBr was investigated using different anions (1.00 g/L) such as carbonate ions (CO<sub>3</sub><sup>2-</sup>), sulfate ions (SO<sub>4</sub><sup>2-</sup>), nitrate ions (NO<sub>3</sub><sup>-</sup>) and chloride ions (Cl<sup>-</sup>). These selected anions were based on research works by Gao et al. (2016) and Li et al. (2016). The anions were added into SSY solution before executing the experiment. The other experimental conditions were set at BiOBr loading at 1.00 g/L, initial SSY concentration at 10 ppm and solution pH at 3.0.

### 3.9 OPTIMIZATION STUDIES USING RESPONSE SURFACE METHODOLOGY (RSM)

Numerous researchers have reported that the photocatalyst loading, initial substrate concentration, solution pH and irradiation time were the main parameters to affect the photocatalytic degradation process (Wang et al., 2012; Li et al., 2012; Han et al., 2016; Janani et al., 2016). Nevertheless, most of them were determined individually by varying one parameter each time while keeping the other constant. This analytical method can only be an incomplete detection of the process parameters in the photocatalytic degradation due to the possible interaction between studied variables can be ignored (Xiao et al., 2016). Hence, to overwhelm these limitations, a response surface methodology (RSM) based on central composite design (CCD) was applied in this study for process optimization and analyzed the effect of each studied variables as well as the interaction effects on photocatalytic degradation of SSY.

In CCD method, each selected variable was studied at three levels named zero level, low level coded (-1) and high level coded (+1). Besides, every variables were given factor codes during modeling process such as catalyst loading ( $X_i$ ), initial dye concentration ( $X_{ii}$ ), solution pH ( $X_{iii}$ ) and irradiation time ( $X_{iv}$ ). The desired response ( $Y$ ) is the percentage of SSY degradation under different conditions. The details are presented in Table 3.2.

Table 3.2 The coded and actual values of the design factors.

Factor	Factor code	Unit	Low level (-1)	Zero level (0)	High level (+1)
Catalyst loading	$X_i$	g/L	0.5	1.25	2
Initial dye concentration	$X_{ii}$	ppm	10	30	50
Solution pH	$X_{iii}$	-	3	6	9
Irradiation time	$X_{iv}$	min	60	120	180

The number of experiment will be determined using the expression:  $2^n + 2n + 6$  where  $n$  is the number of variables and 6 are the six replication in CCD design. The experimental variables took into consideration were BiOBr loading, initial SSY concentration, solution pH and irradiation time. The CCD in four variables ( $n=3$ ) and two levels: low level (-1) while high level (+1) consisted 30 sets of experiments which can be separated to three blocks: (a) 16 factor points, (b) 8 axial points and (c) 6 center point for replication. The percentage of SSY degradation was chosen as the response variable (%Y). Table 3.3 summarizes the actual experimental design matrix for SSY degradation that carried out in this research.

Table 3.3 Experiment design matrix for optimization of SSY degradation.

Run	Point type	Factors			
		$X_i$	$X_{ii}$	$X_{iii}$	$X_{iv}$
2	Center	0	0	0	0
5	Center	0	0	0	0
8	Center	0	0	0	0
12	Center	0	0	0	0
23	Center	0	0	0	0
24	Center	0	0	0	0
4	Axial	0	0	0	1
9	Axial	-1	0	0	0
11	Axial	0	1	0	0
15	Axial	0	-1	0	0
16	Axial	1	0	0	0
20	Axial	0	0	1	0
22	Axial	0	0	0	-1
26	Axial	0	0	-1	0
1	Factorial	1	-1	1	1
3	Factorial	1	-1	1	-1
6	Factorial	-1	-1	-1	1
7	Factorial	1	1	1	-1
10	Factorial	-1	1	1	1
13	Factorial	1	-1	-1	1
14	Factorial	-1	-1	-1	-1
17	Factorial	1	-1	-1	-1
18	Factorial	1	1	-1	-1
19	Factorial	-1	-1	1	1
21	Factorial	1	1	1	1
25	Factorial	1	1	-1	1
27	Factorial	-1	1	1	-1
28	Factorial	-1	1	-1	-1
29	Factorial	-1	-1	1	-1
30	Factorial	-1	1	-1	1

The obtained experimental results were then analysed by variance analysis (ANOVA). Lastly, the reliability of every variables were proven by the multiple coefficient of determination,  $R^2$  and the optimum operating parameters as well as the interaction of selected variables were obtained.

## CHAPTER FOUR

### RESULT AND DISCUSSION

#### 4.1 CHARACTERIZATION STUDIES

##### 4.1.1 X-Ray Diffraction (XRD)

The crystal structure of flower-like BiOBr hierarchical structures was analysed via X-ray diffraction method (XRD). Figure 4.1 demonstrates the XRD pattern of as-prepared flower-like BiOBr. All the diffraction peaks were labelled and can be corresponded to the tetragonal phase of BiOBr (JCPDS no.09-0393) with lattice parameters ( $a = 3.92 \text{ \AA}$ ,  $c = 8.10 \text{ \AA}$ ). The diffraction peak at  $10.9^\circ$ ,  $21.9^\circ$ ,  $25.2^\circ$ ,  $31.7^\circ$ ,  $32.2^\circ$ ,  $34.1^\circ$ ,  $39.3^\circ$ ,  $44.6^\circ$ ,  $46.4^\circ$ ,  $46.9^\circ$ ,  $50.7^\circ$ ,  $53.4^\circ$ ,  $56.2^\circ$ ,  $57.1^\circ$ ,  $61.9^\circ$ ,  $66.2^\circ$  and  $67.4^\circ$  were the evidence of tetragonal geometry of as-prepare BiOBr. High purity of the as-prepared products was also observed in this XRD pattern. Moreover, the intense and sharp diffraction peaks also showed that the obtained flower-like BiOBr were well crystalline.

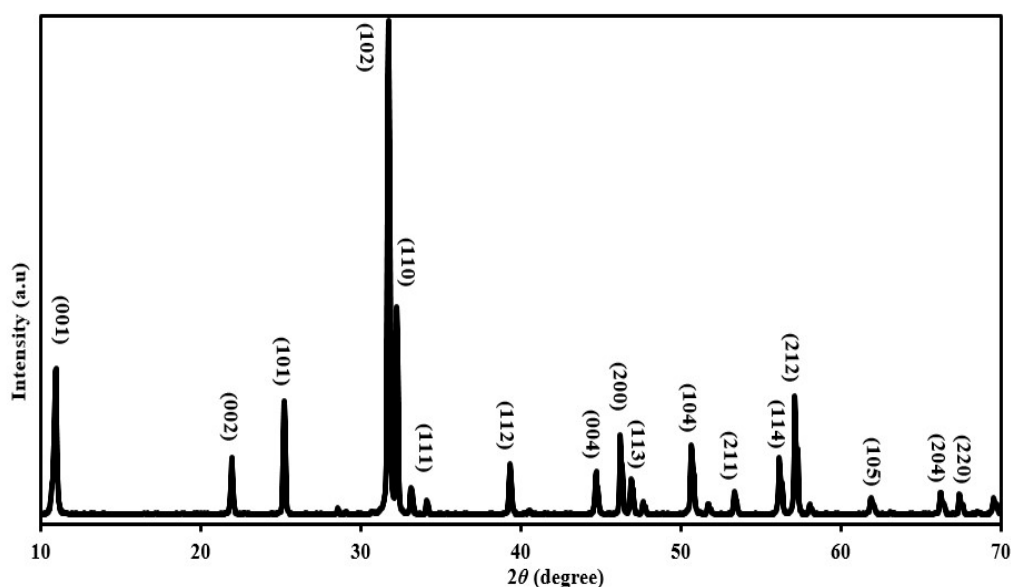


Figure 4.1 XRD pattern of as-synthesized flower-like BiOBr hierarchical structures.

XRD analysis was used by Chen et al. (2011) to characterize the solvothermally synthesized flower-like BiOBr. The XRD pattern of BiOBr also showed the main diffraction peaks of (101), (102), (110) at  $\sim 25.2^\circ$ ,  $\sim 31.7^\circ$  and  $\sim 32.2^\circ$ , indicating the well crystalline and tetragonal phase of BiOBr. At the same year, Huo et al. (2011) also investigated the crystal structure of solvothermally synthesized flower-like BiOBr via XRD analysis. Their results have a good agreement with the finding of Chen et al. (2011) where pure BiOBr crystal phase with high crystallization was obtained.

Besides, Zhang et al. (2014) synthesized BiOBr nanosheets via hydrothermal method and characterized the crystal structure of as-prepared BiOBr using XRD analysis. Based on the XRD pattern, the as-synthesized BiOBr agreed well with the standard data of tetragonal BiOBr and have the most intense peak of (102) and (001), respectively. Mera et al. (2017) conducted photocatalytic degradation of anionic dye via BiOBr microspheres. The as-prepared BiOBr microspheres were characterized via XRD for investigating the phase and crystal structure. They reported the peaks in the XRD pattern can be assigned to the diffraction of (001), (002), (101), (110), (112), (200), (104), (211), (212) and (220) planes of the pure tetragonal BiOBr.

#### **4.1.2 Energy Dispersive X-ray Spectroscopy (EDX)**

Energy dispersion X-ray (EDX) was obtained to characterize the chemical elemental components of the as-synthesized flower-like BiOBr hierarchical structures. Figure 4.2 shows the EDX spectrum of as-synthesized flower-like BiOBr hierarchical structures. The atomic percentage of elemental composition of as-synthesized photocatalysts is shown inset of Figure 4.2. The EDX results suggested the existence of Bi, O and Br species in the structure of

the hydrothermally synthesized photocatalysts by showing distinctive Bi, O and Br peaks in the spectrum. However, the carbon (C) diffraction peak was also determined in the spectrum which dedicated to the supporting carbon tape.

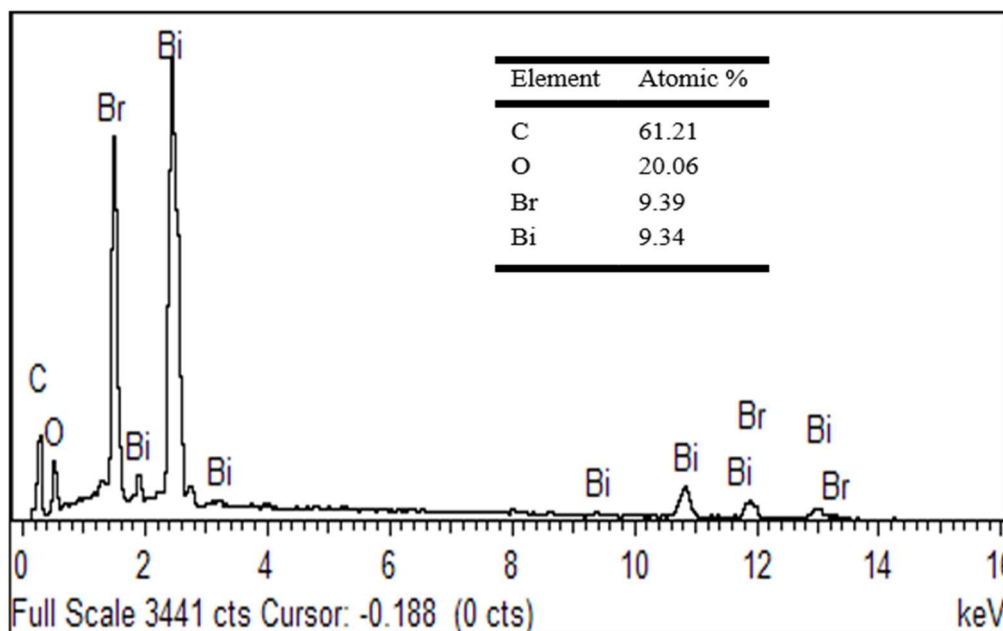


Figure 4.2 EDX spectrum of as-synthesized flower-like BiOBr hierarchical structures. The *inset* show element composition of as-synthesized BiOBr.

#### 4.1.3 Field Emission Scanning Electron Microscopy (FESEM) Analysis

The morphologies of hydrothermally synthesized flower-like BiOBr hierarchical structures were characterized by FESEM and the results are shown in Figure 4.3 (a-d). It can be clearly seen from the FESEM images in Figure 4.3 (a) and (b), as-synthesized BiOBr were in flower-shaped and had sizes in the range of several hundred nanometers to micrometers. With a closer observation in Figure 4.3 (c) and (d), the microflowers consisted hierarchical structures assembled by lots of interleaving nanosheets with average thickness of ~80 nm and formed an open porous structure by oriented aggregation. Besides, the FESEM images of hydrothermally synthesized BiOBr nanosheets were obtained and shown in Appendix I. It can be observed from the FESEM images that large

quantities of irregular with smooth surface BiOBr nanosheet were obtained. By observing the magnified image, the nanosheets with sizes ranged from 0.1  $\mu\text{m}$  to 0.8  $\mu\text{m}$  were stacked each other.

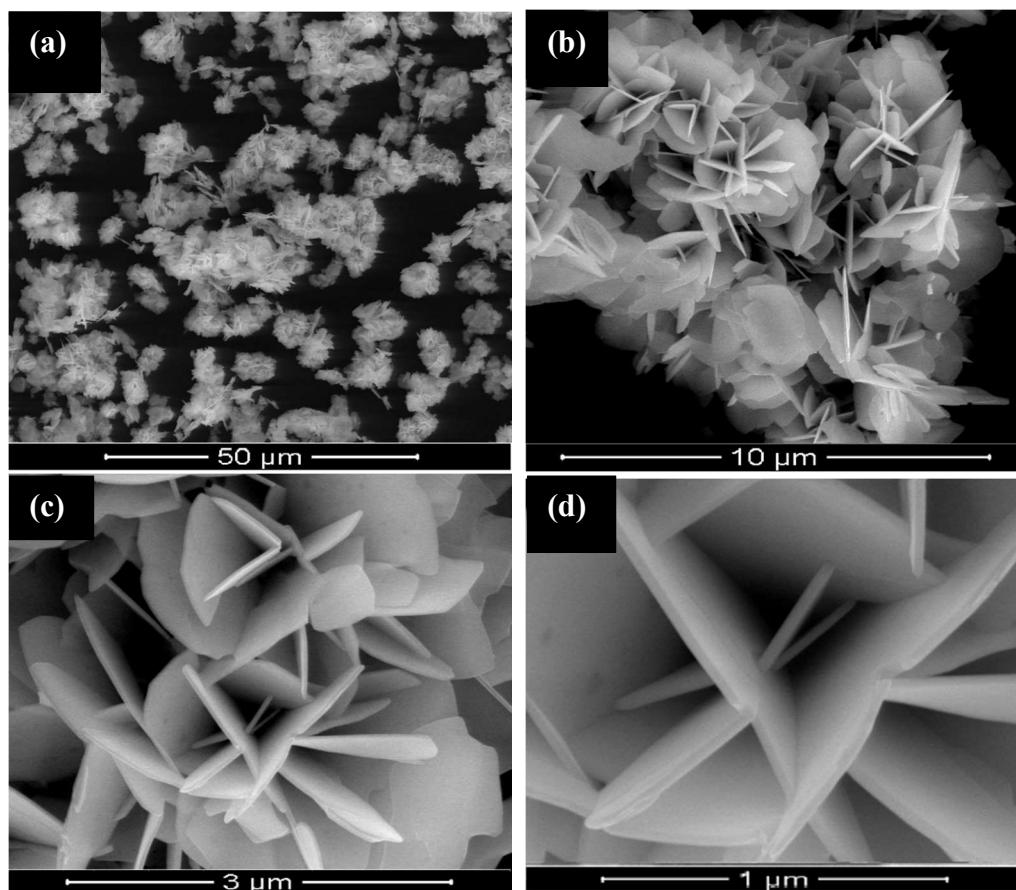


Figure 4.3 (a-d) FESEM images of as-synthesized flower-like BiOBr hierarchical structures at different magnifications: (a) 1500X, (b) 10000X, (c) 20000X and (d) 40000X.

#### 4.1.4 Transmission Electron Microscopy (TEM) and High Resolution Transmission Electron Microscopy (HRTEM) Analysis

The microstructure of as-synthesized flower-like BiOBr was evaluated by TEM and HRTEM analysis. As illustrated in Figure 4.4 (a), the TEM image showed that the nanosheets were arranged in such an order way to form flower-shaped morphologies of as-synthesized BiOBr which further confirmed the



FESEM investigation. Figure 4.4 (b) presents the HRTEM image of as-synthesized BiOBr. The crystallinity of as-prepared flower-like BiOBr can be proven by clear lattice fringe with interplanar spacing of 0.28 nm in the HRTEM image. The observed clear lattice fringe indicated that the as-synthesized BiOBr were well crystallized (Huo et al., 2012; Liu et al., 2014; Wang et al., 2015). On the other hand, the lattice spacing of 0.28 nm further confirmed BiOBr tetragonal structure and growth along (102) plane in XRD analysis.

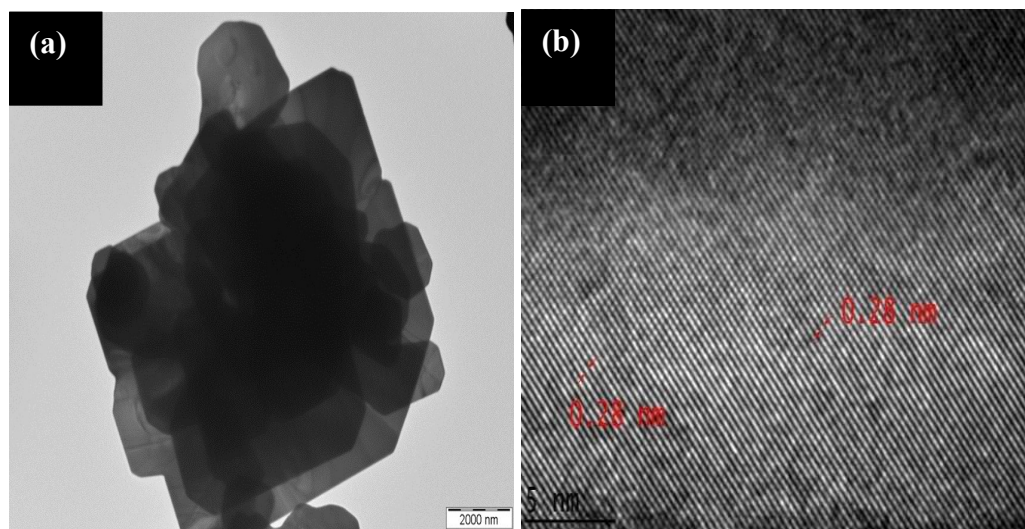


Figure 4.4 (a) TEM and (b) HRTEM images of the as-synthesized flower-like BiOBr hierarchical structures.

In order to further understand the structural properties of as-synthesized flower-like BiOBr samples, Li et al. (2015) employed TEM and HRTEM techniques. Their results showed that clear lattice fringes indicated high crystallinity of their BiOBr samples. They also observed that the distance of lattice spacing was 0.281 nm, which agreed well with the interplanar spacing of (102). The hydrothermally synthesized BiOBr photocatalysts by Yu et al. (2017) were characterized via HRTEM. The HRTEM result showed the interplanar spacing of the crystal was 0.282 nm which has a good agreement with the (102)

plane of tetragonal BiOBr. Hence, the FESEM and XRD results were supported by the TEM and HRTEM analysis, respectively.

#### 4.1.5 X-ray Photoelectron Spectroscopy (XPS)

XPS analysis was used to investigate the surface composition and chemical states of as-synthesized flower-like BiOBr photocatalysts. Figure 4.5 shows the XPS survey spectrum of hydrothermally synthesized flower-like BiOBr hierarchical structures. Bi 4f, O 1s and Br 3d can be easily seen in the XPS spectrum which verified the formation of BiOBr. A trace amount of carbon (C) was also observed in the spectrum which due to the adventitious hydrocarbon from XPS itself (Jiang et al., 2014).

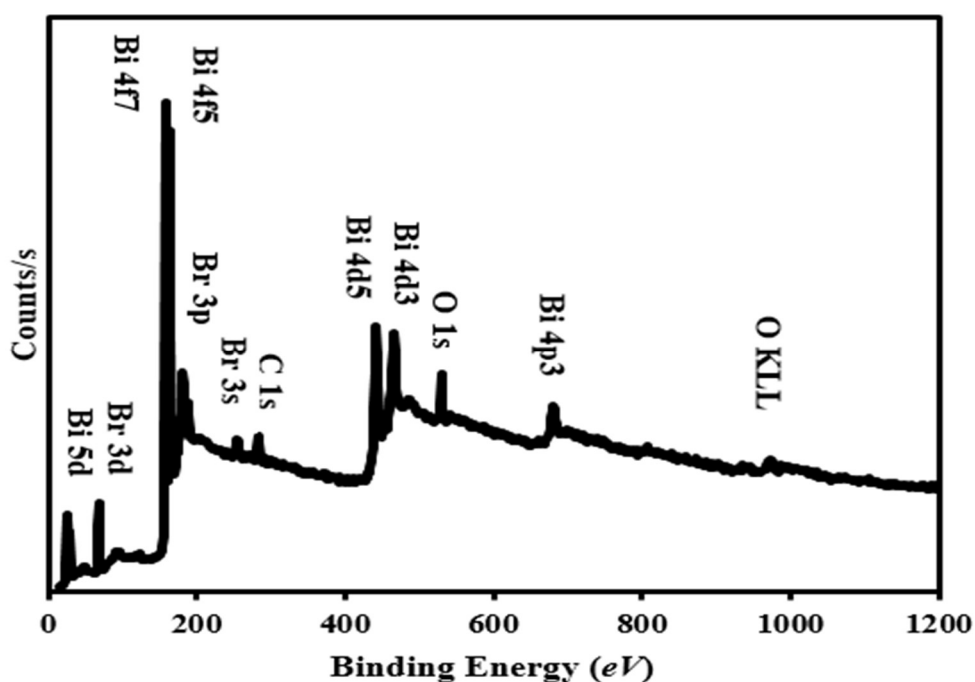


Figure 4.5 XPS survey spectra of as-synthesized flower-like BiOBr hierarchical structures.

Figures 4.6 to 4.8 show the high resolution XPS spectra of Bi, O and Br elements. For the XPS of Bi 4f (Figure 4.6), it can be observed that two main asymmetrical splitting peaks of Bi 4f are located at 159.9 and 165.1 eV were corresponded to Bi 4f<sub>7/2</sub> and Bi 4f<sub>5/2</sub>, respectively. The existence of these peaks indicating the chemical states of bismuth element were trivalent, Bi<sup>3+</sup> in BiOBr (Liu et al., 2013; Jiang et al., 2014). The O 1s XPS spectrum in Figure 4.7 showed a peak at 530.5 eV, which was denoted to lattice oxygen in [Bi<sub>2</sub>O<sub>2</sub>] slabs of BiOBr layered structure (Meng and Zhang, 2015; Yu et al., 2017; Liu et al., 2017). In addition, the Br 3d peak occurred at 69.1 eV was represented the existence of Br<sup>-</sup> in tetragonal BiOBr (Figure 4.8) (Shi et al., 2013; Gao et al., 2018).

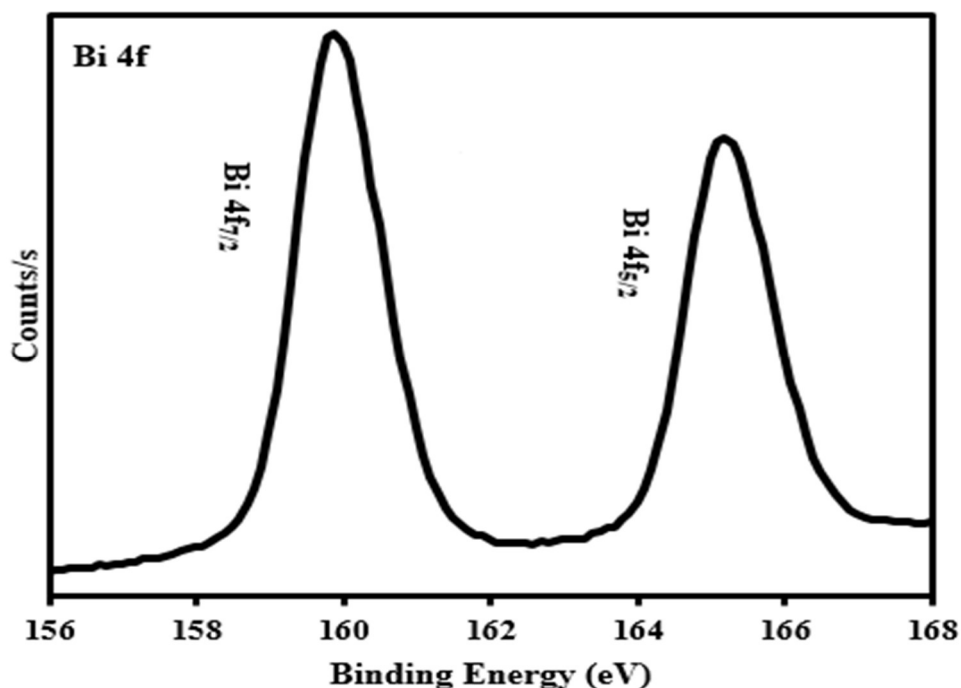


Figure 4.6 XPS spectra of bismuth (Bi 4f) in as-synthesized flower-like BiOBr hierarchical structures.

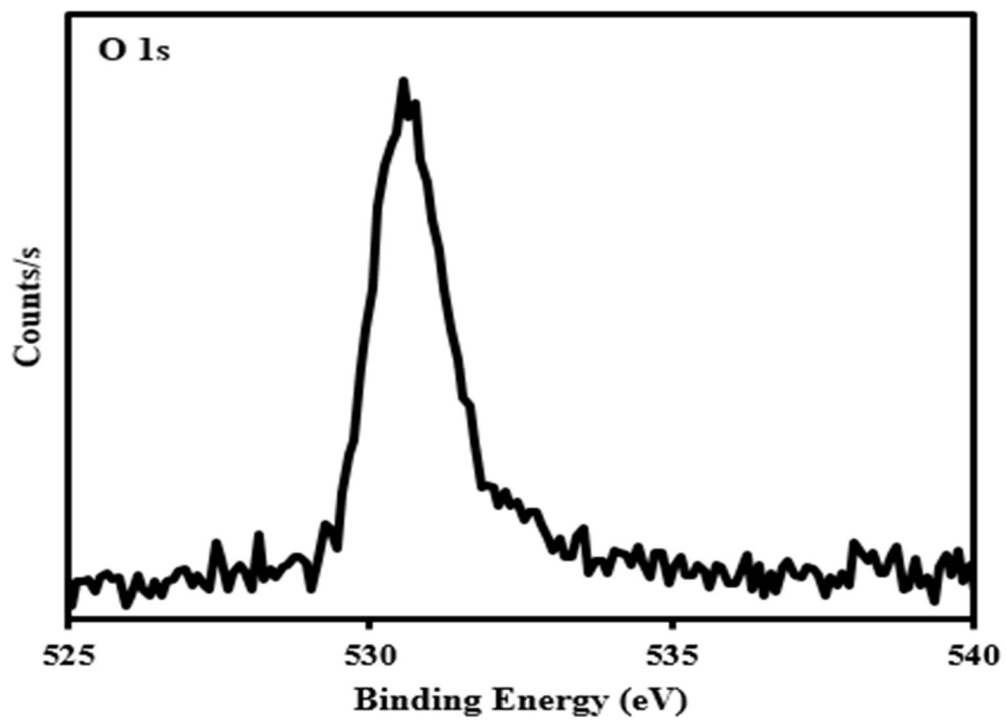


Figure 4.7 XPS spectra of oxygen (O 1s) in as-synthesized flower-like BiOBr hierarchical structures.

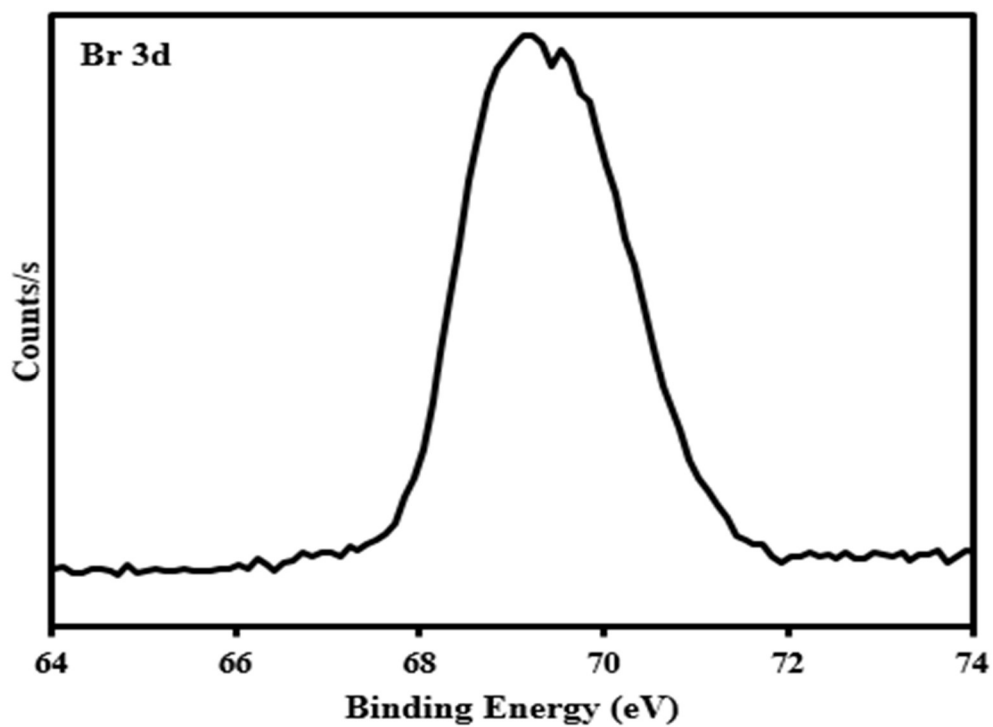


Figure 4.8 XPS spectra of bromine (Br 3d) in as-synthesized flower-like BiOBr hierarchical structures.

#### 4.1.6 UV-vis Diffuse Reflectance Spectroscopy (UV-vis DRS)

The optical properties of BiOBr were evaluated via UV-vis DRS spectroscopy. The UV-vis DRS spectra of hydrothermally synthesized flower-like BiOBr and TiO<sub>2</sub> are shown in Figure 4.9. The as-synthesized BiOBr photocatalysts showed a fundamental photoabsorption edge at 430 nm while the TiO<sub>2</sub> exhibited photoabsorption below 400 nm. This indicated that the light absorption of flower-like BiOBr hierarchical structures in the visible light region was higher than the TiO<sub>2</sub>.

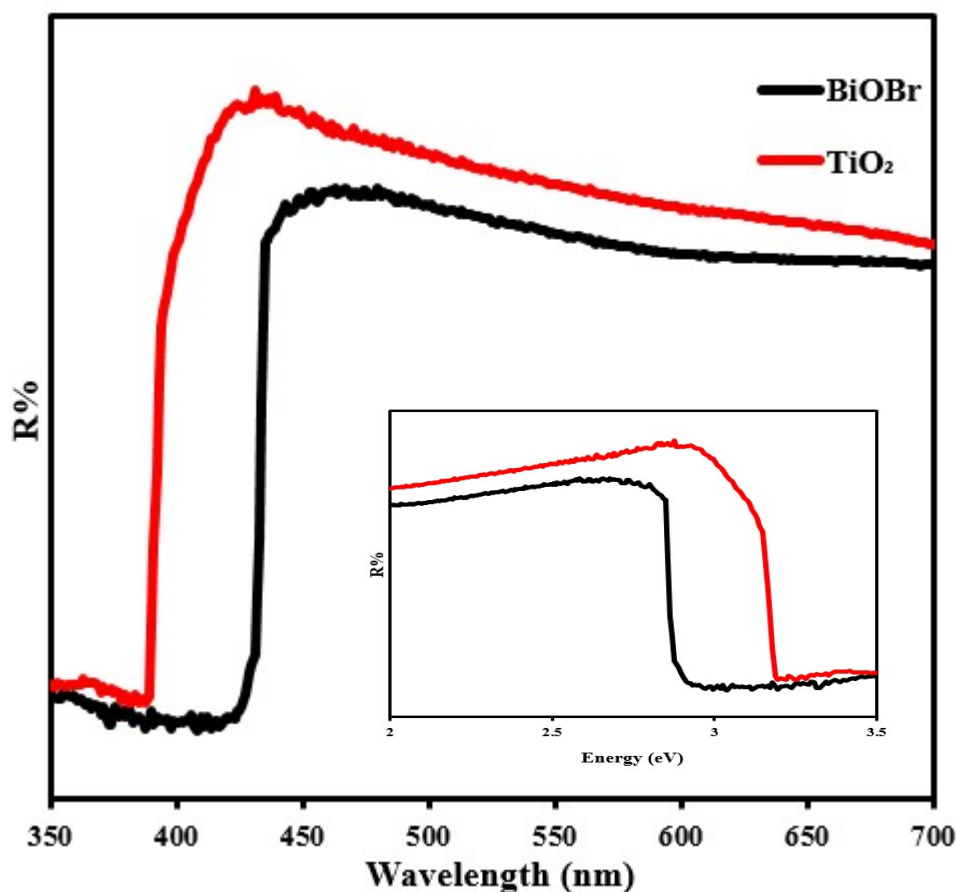


Figure 4.9 UV-vis DRS spectra of as-synthesized flower-like BiOBr hierarchical structures and TiO<sub>2</sub>. The *inset* shows the plot of R% versus photon energy

Furthermore, the  $E_g$  of as-synthesized BiOBr samples and TiO<sub>2</sub> were calculated using the Planck equation (Equation 4.1):

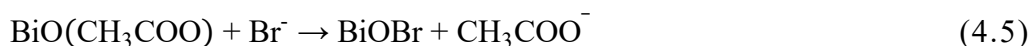
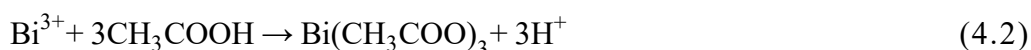
$$E_g (\text{eV}) = \frac{1240}{\lambda (\text{nm})} \quad (4.1)$$

where  $E_g$  is the band gap energy (nm) of absorption onset and  $\lambda$  is the wavelength.  $E_g$  were determined to be 2.88 eV and 3.24 eV for flower-like BiOBr hierarchical structures and TiO<sub>2</sub>, respectively.

The band gap of flower-like BiOBr hierarchical structures which determined in this study was well consistent with the band-gap values of BiOBr reported by previous researchers (Liu et al., 2012; Xiong et al., 2014; Xing et al., 2015). Based on the results, the reflectance property implied that flower-like BiOBr hierarchical structures can be promising in the sunlight photocatalysis compared with that of TiO<sub>2</sub>.

#### **4.2 PROPOSED GROWTH MECHANISM OF FLOWER-LIKE BiOBr HIERARCHICAL STRUCTURES.**

The mechanism responsible for the growth of flower-like BiOBr hierarchical structures was proposed. In the present system, the precursor of Bi, Bi(NO<sub>3</sub>)<sub>3</sub>•5H<sub>2</sub>O reacted with acetic acid to form Bi(CH<sub>3</sub>COO)<sub>3</sub> in solution (A). Concurrently, the KBr was dissolved in water in order to dissociate Br<sup>-</sup> ions in solution (B). Upon the mixing of both solution A and B, the Bi(CH<sub>3</sub>COO)<sub>3</sub> reacted with water to form BiO(CH<sub>3</sub>COO) and then Br<sup>-</sup> ions can react with BiO(CH<sub>3</sub>COO) to form BiOBr nuclei via anion exchange process. The reaction can be demonstrated as follows (Equation 4.2 to Equation 4.5):



From the XRD analysis, the as-synthesized BiOBr samples were proven to be tetragonal crystal structures. The  $[\text{Bi}_2\text{O}_2]$  slabs were sandwiched by two Br slabs and a  $[\text{Bi}_2\text{O}_2\text{Br}_2]$  layer forms, which are stacked together by the van der Waals forces. The weak van der Waals interaction and the strong intralayer bonding induced the anisotropic growth to form 2D nanosheets (Deng and Guan, 2013). During anisotropic growth, surface energy of each nanosheets was quite high with two main exposed planes. In order to reduce exposed area, they aggregated into larger grains through self-assembled of adjacent nanosheets leading a 3D assembly process and then minimized the surface energy of each nanosheet (Zhang et al., 2012). Thus, the flower-like BiOBr hierarchical structures were fabricated from the nanosheets by oriented aggregation process. Figure 4.10 shows the suggested illustration of the formation process of flower-like hierarchical structure.

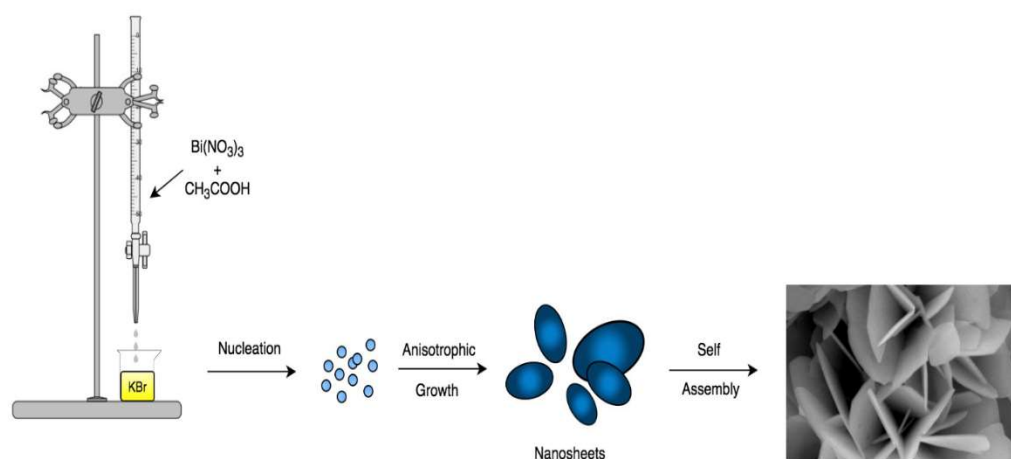


Figure 4.10 Schematic illustration of the formation process of flower-like BiOBr hierarchical structures.

### 4.3 PHOTOCATALYTIC STUDIES OF FLOWER-LIKE BiOBr HIERARCHICAL STRUCTURES UNDER DIFFERENT CONDITIONS

The photocatalytic activity of the as-prepared flower-like BiOBr hierarchical structures was determined by degradation of SSY (catalyst loading= 1.00 g/L, initial SSY concentration= 10 ppm as well as solution pH= natural pH of SSY) under fluorescent light irradiation as presented in Figure 4.11. The dark adsorption for the flower-like BiOBr hierarchical structures represented the inactivation of SSY by BiOBr in absence of any irradiation source. In such condition, the removal of SSY was 7% indicated that flower-like BiOBr does not exhibit photocatalytic activity without light irradiation.

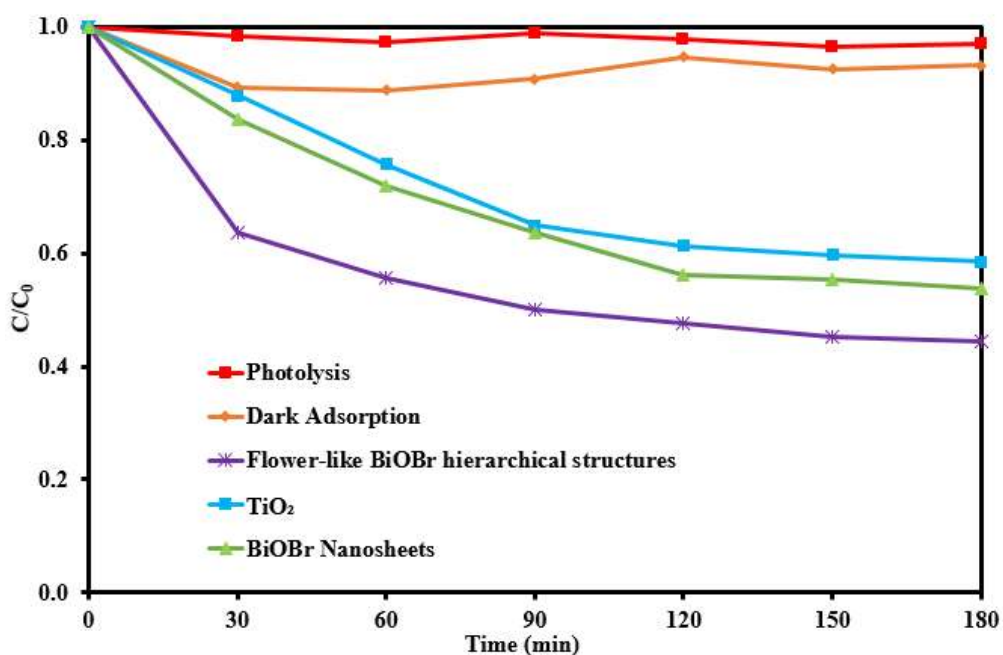


Figure 4.11 Control experiments and photocatalytic degradation of SSY over different types of photocatalysts. Conditions: catalyst loading= 1.00 g/L, initial dye concentration= 10 ppm, solution pH= natural pH of SSY.



On the other hand, blank experiment of SSY degradation in the absence of catalysts under the similar conditions was also carried out. Due to the absence of BiOBr, the SSY barely degraded after 180 min of photolysis under fluorescent light irradiation. It can be observed that SSY self-photodegradation was almost negligible under fluorescent light irradiation in the absence of BiOBr. This demonstrated that pure SSY do not possess photocatalytic activity without any presence of photocatalysts.

Compared with the experiments stated above, the photodegradation efficiency of SSY was accelerated in the existence of flower-like BiOBr hierarchical structures, BiOBr nanosheets and TiO<sub>2</sub>. With the presence of photocatalysts, the degradation of SSY was observed to be 53.5%, 46.2% and 41.4% for the stated photocatalysts, respectively. The flower-like BiOBr hierarchical structures exhibited higher degradation as compared to TiO<sub>2</sub> due to the band gap of as-synthesized BiOBr (2.88 eV) can be easily activated by visible light for photocatalytic reaction. However, the absorption property acquired from UV-vis DRS inferred that the TiO<sub>2</sub> have inappropriate band gap (3.24 eV) to be activated under visible light irradiation. Besides, the excellent degradation efficiency of SSY over as-synthesized BiOBr can be explained by the efficient generation of huge number of  $e^-h^+$  pairs under light irradiation. With great absorption properties in both UV and visible light regions the quantity of photogenerated electron-holes pairs can be increased and available to participate in the photocatalytic degradation of SSY over as-synthesized BiOBr photocatalysts.

The results were in a well accordance with the experiments of organic pollutants degradation which performed by Xu et al. (2013). Their findings revealed that the photocatalytic activity of BiOBr spheres was better than TiO<sub>2</sub>. They explained that low band gap of BiOBr allowed the photo absorption to increase and produced abundant of  $e^-h^+$  pairs leading to the increase of photocatalytic activities of BiOBr. The photocatalytic activity of BiOBr microspheres and TiO<sub>2</sub> were also examined by Xue et al. (2014) via photodegradation efficiency of RhB. From their observations, BiOBr microspheres can degrade 91% of RhB while TiO<sub>2</sub> exhibited only 14.5% of RhB degradation in the same reaction conditions (catalyst loading= 1.00 g/L and initial RhB concentration= 15 ppm). They mentioned that the excellent photocatalytic performance of BiOBr microspheres was attributed to its efficient charge separation during visible light irradiation.

Moreover, the photocatalytic degradation of SSY over flower-like BiOBr was higher than the BiOBr nanosheet. This was due to the specific surface areas of flower-like BiOBr hierarchical structures was greater than the BiOBr nanosheets. In order to confirm with the hypothesis, the Brunauer-Emmett-Teller (BET) specific surface areas of both photocatalysts were characterized by N<sub>2</sub> adsorption-desorption isotherm (Appendix II). The results showed that the adsorbed volume of flower-like BiOBr hierarchical structures was comparatively high. The BET specific surface area of flower-like BiOBr was determined to be 4.7595 m<sup>2</sup>/g which significantly larger than the value (0.0708 m<sup>2</sup>/g) of BiOBr nanosheets. Therefore, the enhanced photocatalytic performance of flower-like BiOBr hierarchical structures can attribute to their specific

hierarchical structures and large surface area which allowed light penetration as well as provided more active sites for the photocatalytic degradation of SSY.

The obtained results were in a good agreement with the research done by Zhang et al. (2011). They found out that hierarchical BiOBr microspheres can degrade 55% of MB while the degradation efficiency of BiOBr nanosheet was only 10%. They mentioned that such excellent photodegradation performance of BiOBr microspheres ascribed to the hierarchical 3D microstructures.

A similar trend was observed by Xu et al. (2013), the photocatalytic activity of BiOBr spheres was better than BiOBr plates for the degradation of benzotriazole. They reported that the excellent photocatalytic performance of BiOBr spheres can be ascribed to their hierarchically spherical structure equipped with larger surface area. They also added that the larger surface area can utilize the irradiation of light and provided more capacious spaces which were beneficial for the enhancement of photodegradation of a photocatalysts

Wu et al. (2015) conducted photocatalytic experiments on the degradation of RhB over BiOBr microspheres and BiOBr nanosheets. Their results showed that the degradation rate constant of BiOBr microspheres ( $0.0623 \text{ m}^{-1}$ ) was four times higher than BiOBr nanosheets ( $0.0152 \text{ m}^{-1}$ ). The large surface area of BiOBr microspheres allowed more active sites exposed to the RhB molecules and this also enhanced the transportation of RhB molecules to the active site. Thus, their photocatalytic degradation efficiency of RhB over BiOBr microspheres was more excellent than the BiOBr nanosheets.

## 4.4 PROPOSED PHOTOCATALYTIC MECHANISM OF FLOWER-LIKE BiOBr HIERARCHICAL STRUCTURES

### 4.4.1 Active Species Trapping Experiments

In order to understand the flower-like BiOBr photocatalytic reaction mechanism for the SSY photodegradation under fluorescent light irradiation, few sets of scavenging experiments were conducted. In the experiments, ethanol was used as scavenger for  $\bullet\text{OH}$  radicals and potassium iodide (KI) was chosen for quenching the  $h^+$  over the photocatalysts. With the direct participation of scavengers, the photocatalytic degradation can decrease to some extents. The suppression of photocatalytic performance indicated that the corresponding radical played an important role in degradation process. All the active species scavenging tests were conducted with catalyst loading= 1.00 g/L, initial SSY concentration= 10 ppm, solution pH= natural pH of SSY and scavenger concentration= 0.5 mmol.

The results of SSY degradation over flower-like BiOBr hierarchical structures in the presence of ethanol and KI scavengers are shown in Figure 4.12. It can be observed that the degradation efficiencies of flower-like BiOBr were significantly decreased after the addition of various radical scavenging agents. When the addition of ethanol into SSY solution under fluorescent light irradiation, the photodegradation of SSY declined to 25 % while the degradation percentage of SSY decreased to 20% in the presence of KI.

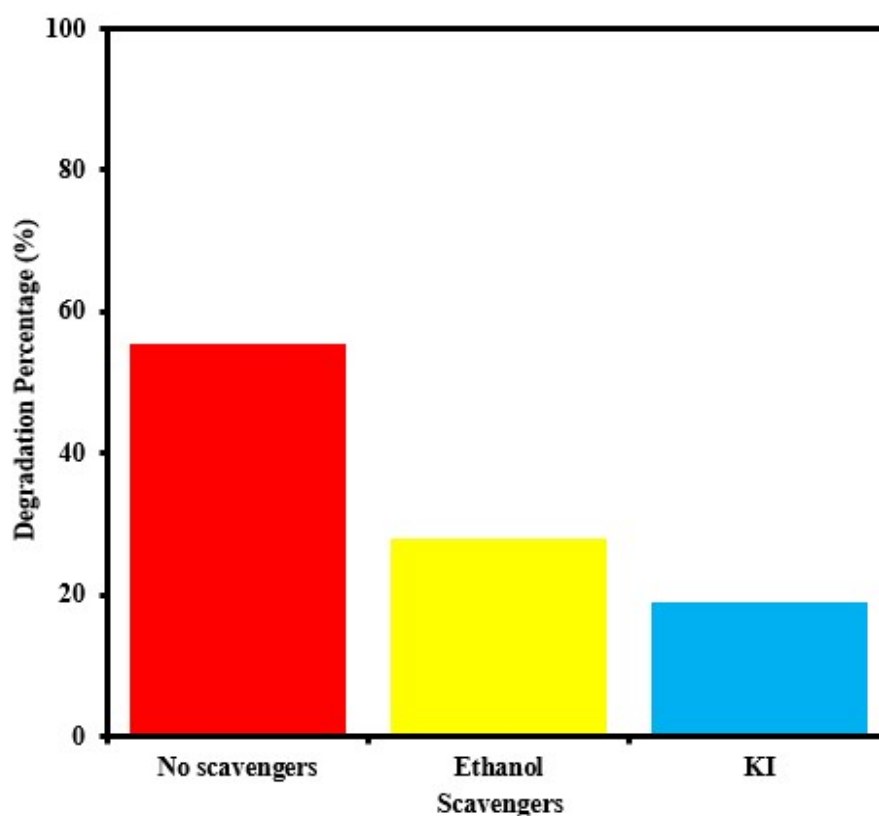
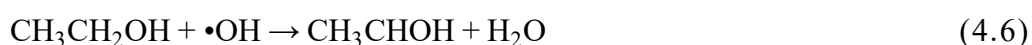
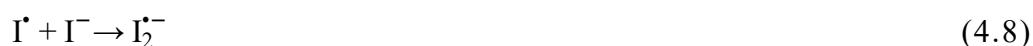


Figure 4.12 Photocatalytic degradation of SSY over flower-like BiOBr hierarchical structures in the absence and presence of scavengers under fluorescent light irradiation for 180 min. Condition: catalyst loading= 1.00 g/L, initial SSY concentration= 10 ppm, solution pH= natural pH of SSY and scavenger concentration= 0.5 mmol.

The inhibition effect of ethanol on the photodegradation of SSY over as-prepared BiOBr hierarchical structures can be due to the rapid reaction between  $\bullet\text{OH}$  radicals and ethanol to form acetaldehyde (Wang et al., 2016) (Equation 4.6).



Besides, the direct participate of  $h^+$  during photocatalytic degradation of SSY was interrupted by KI through mechanisms as follows (Equation 4.7 to Equation 4.9).



In order to investigate the roles of reactive species existing in the BiOBr photocatalytic degradation process of MO, corresponding scavengers were added by Wang et al. (2013) to the reaction solution. When the •OH radicals scavengers and  $h^+$  quencher were added separately in the photocatalytic reaction system, the photodegradation of MO decreased significantly. They deduced that •OH radicals and  $h^+$  played important roles in the photocatalytic degradation of MO. Patil et al. (2016) carried out active species trapping experiments to detect the main active species in the photocatalysis of direct green (DG) over BiOBr-graphene oxide (GO). The main active species such as •OH radicals and  $h^+$  were trapped using methanol and KI. With the presence of methanol and KI, the photocatalytic degradation of DG decreased down to 38% and 24.2%, respectively while compared to photocatalytic degradation carried out without any presence of trapping agents (91.9 %).

The results of trapping experiments conducted by Jiang et al. (2017) have good agreement with the results in this study. The photocatalytic activity of BiOBr/BiOF decreased to 27.4 % for degradation of RhB with the addition of  $h^+$  scavengers, demonstrating the  $h^+$  played an important role in the degradation process. Besides, with the existence of •OH radicals scavengers, the degradation rate decreased to 68.4 % while comparing with degradation efficiency without scavengers (91.9 %). This indicated that •OH radicals were also important in the photodegradation of RhB over BiOBr/BiOF photocatalysts. Hence, the  $h^+$  and

•OH radicals were the main reactive species in the photocatalytic reaction of SSY over flower-like BiOBr hierarchical structures.

#### 4.4.2 Terephthalic Acid Photoluminescence Probing Technique (TA-PL)

TA-PL is a method of PL to detect the formation of •OH radicals using terephthalic acid as a probe molecule. In the extent of further confirmed the formation of •OH radicals during photodegradation of SSY over flower-like BiOBr, the TA-PL technique was employed. The main reason was that the terephthalic acid can react with •OH radicals to produce highly fluorescent product, 2-hydroxyterephthalic acid (TAOH) (Yu et al., 2012). TAOH can exhibit its photoluminescence peak at 425 nm under an excitation wavelength of 315nm during TA-PL experiments (Cao et al., 2012; Na et al., 2014; Han et al., 2018). Hence, the number of •OH radicals produced during photodegradation of SSY can be determined by the TA-PL intensity.

Figure 4.13 presents the PL spectra of flower-like BiOBr hierarchical structure at different irradiation times. A high intensity peak was observed at 425 nm in the PL spectra. The formation of •OH radicals happened during the photocatalytic activity of flower-like BiOBr hierarchical structures. Besides, a gradual increase in PL intensity at 425 nm was observed with changing of irradiation time. This indicating that •OH radicals were produced along with irradiation time and reacted with terephthalic acid to form TAOH during SSY photodegradation.

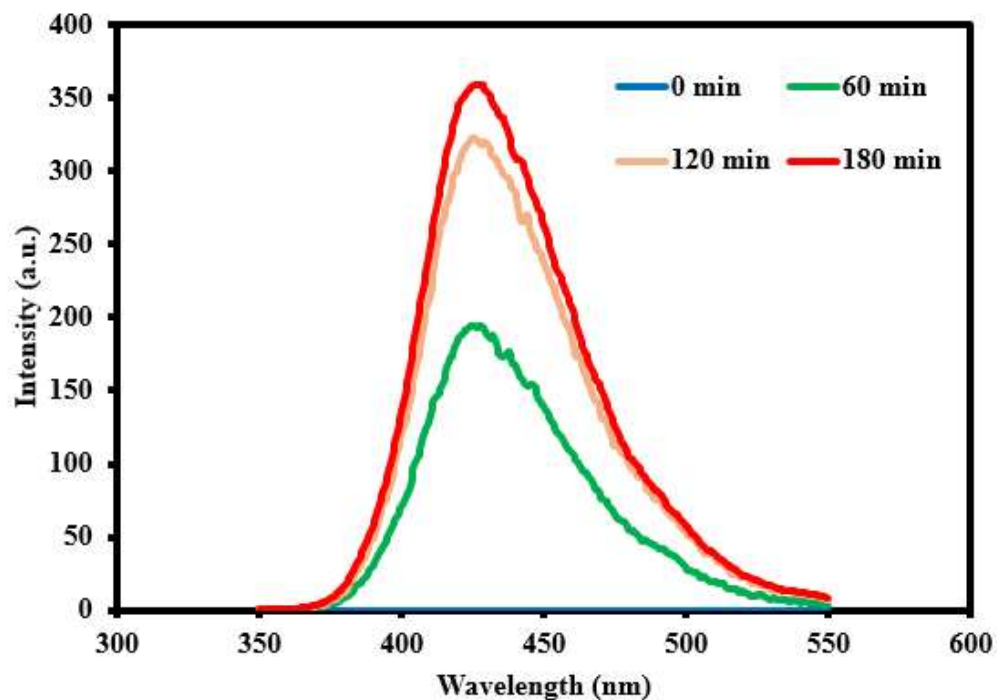


Figure 4.13 PL spectra changing with irradiation time over the flower-like BiOBr hierarchical structures.

This result was in an agreement with the results obtained by Zhang and Zeng (2017). They employed TA-PL technique to determine the formation of  $\bullet\text{OH}$  radicals in the ZnO-BiOBr photocatalysis. They suggested that the fluorescence was due to the chemical reaction of terephthalic acid with  $\bullet\text{OH}$  radicals formed during photodegradation of methylene blue (MB). They also observed that the fluorescence intensity was corresponding to the amount of  $\bullet\text{OH}$  radicals generated as the irradiation time increased. The hydrothermally synthesized two-dimensional BiOBr coupled with molybdenum disulphide ( $\text{MoS}_2$ ) were also analyzed via TA-PL technique to detect the formation of  $\bullet\text{OH}$  radicals (Lee et al., 2017). The peak intensity at 425 nm also increased gradually with increasing irradiation time during in their study. They concluded that  $\bullet\text{OH}$  radicals were formed and took part in degradation of RB5 over BiOBr/ $\text{MoS}_2$  under visible light irradiation.



TiO<sub>2</sub> was also chosen to be compared with flower-like BiOBr during TA-PL experiments and the results are shown in Figure 4.14. By observing the PL spectra, the PL peak intensity at 425 nm of flower-like BiOBr structure was significantly higher than the peak intensity of TiO<sub>2</sub> after 180 irradiation in terephthalic acid solution. This indicated the flower-like BiOBr hierarchical structures able to form abundant amount of •OH radicals compared to TiO<sub>2</sub> under fluorescent light irradiation.

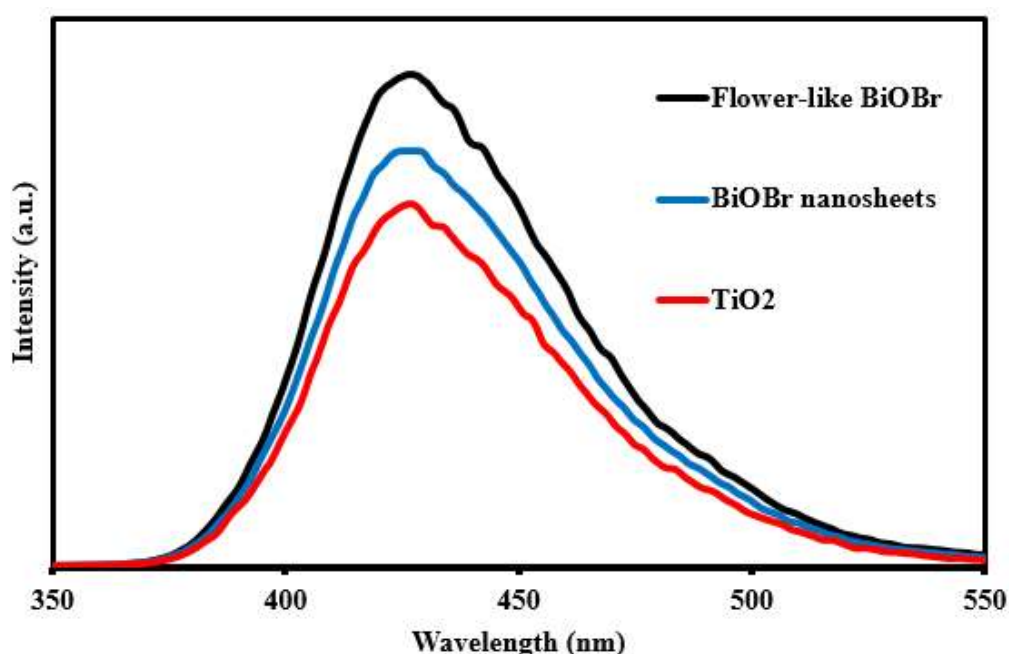


Figure 4.14 PL spectra of TA with an excitation at 315 nm for as-synthesized flower-like BiOBr hierarchical structures, BiOBr nanosheets and TiO<sub>2</sub>.

The depression of •OH radicals generation was due to the large band gap of TiO<sub>2</sub> which restricted the visible light absorption and consequently reduced the production of •OH radicals. These results were corresponded to the UV-vis DRS results that the light absorption of flower-like BiOBr was relatively higher than TiO<sub>2</sub> under visible light irradiation. Thus, higher visible light absorption of flower-like BiOBr resulted higher •OH radicals formation and favourable for improving the photocatalytic activity compared to TiO<sub>2</sub>.

From Figure 4.14, it also can be observed that the PL spectra peak intensity of flower-like BiOBr hierarchical structures was also higher than BiOBr nanosheets. This was due to the specific surface area of flower-like BiOBr was larger than that of BiOBr nanosheets. The larger surface area of flower-like BiOBr hierarchical structures allowed the active sites to be more exposed and accommodate the penetration of light onto the surface of BiOBr. As the fluorescent light hit on the exposed surface of flower-like BiOBr, generous number of •OH radicals generated and reacted with the terephthalic acid to give PL intensity. However, the small specific surface area of BiOBr nanosheets restricted the active sites to be exposed and reduced the light penetration, leading to low formation of •OH radicals. This indicated that the photocatalytic degradation performance of BiOBr nanosheets was weaker than flower-like BiOBr hierarchical structures, which has been discussed in Section 4.3.

#### 4.4.3 Possible Photocatalytic Mechanism

During photocatalytic degradation, the sunset yellow molecule was adsorbed onto the surface of flower-like BiOBr hierarchical structures. The positive  $h^+$  and  $e^-$  were then generated when BiOBr was exposed and irradiated with a stronger energy than its band gap energy. The  $e^-$  are excited from the valence band (VB) to the conduction band (CB) of BiOBr leaving behind  $h^+$ . The photogenerated  $h^+$  can trap on the catalyst surface and oxidized the water molecule ( $H_2O$ ) into •OH radicals. Then photogenerated  $e^-$  reacted with electron acceptors such as  $O_2$  that adsorbed on BiOBr or dissolved in solution to produce  $H_2O_2$ . Hence, the photocatalytic mechanism of flower-like BiOBr hierarchical structures can be given as (Equation 4.10 – Equation 4.14):



However, the CB potential of BiOBr semiconductor ( $\sim 0.27$  eV) was less negative than the standard reduction potential of  $\text{O}_2$  or  $\text{O}_2^{\bullet -}$  ( $-0.33$  eV), indicating that  $\text{O}_2^{\bullet -}$  cannot be generated on the surface of BiOBr (Wang et al., 2013). As the  $e^-$  unable to reduce  $\text{O}_2$ , it transferred to  $\text{O}_2$  species to form  $\text{H}_2\text{O}_2$  and further generated the  $\bullet\text{OH}$  and  $\text{OH}^-$  ions. The hypothesis have a good agreement with the results obtained from TA-PL characterization over flower-like BiOBr hierarchical structures. A significant PL signal was observed at 425 nm in the PL spectral, indicating that  $\bullet\text{OH}$  radicals were generated and involved in photocatalytic degradation process.

## 4.5 EFFECT OF OPERATING PARAMETERS

### 4.5.1 Effect of BiOBr Loading on Photodegradation of SSY

The photocatalyst loading affects the photocatalytic degradation efficiency of organic pollutants. The optimum amount of catalyst required to be determined to evade the excessive amount of catalyst causing unsatisfactory photocatalytic activity. Traditionally, in order to increase the photocatalysis performance, the catalyst are often increased. As the catalyst loading increased,

the tendency toward agglomeration also increased which can reduce the light absorption and caused light scattering effect (Bora and Mewada, 2017). In this study, the effect of BiOBr loading was studied on the photocatalytic degradation of SSY by varying dosage range from 0.25 g/L to 2.00 g/L (initial SSY concentration = 10 ppm; solution pH = natural pH of SSY; irradiation time= 180 min).

Figure 4.15 presents the degradation efficiency of SSY over flower-like BiOBr hierarchical structures under a constant condition. With the increase in BiOBr amount, the degradation efficiency of SSY firstly increased from 13.0% at 0.25 g/L to 53.5% at 1.00 g/L. However, when BiOBr loading further increased from 1.00 g/L to 2.00 g/L, the efficiency decreased to 43.9% at 2.00 g/L. The increase of degradation efficiency of SSY can be due to the increase in the number of photons absorbed by BiOBr particles from fluorescent light resulting to excitation of mass number of  $e^-$  leaving from the valence band to the conduction band. The more the  $e^-$  transferred, the more the number active species such as  $\bullet\text{OH}$  radicals and  $h^+$  generated for photocatalytic reactions with the increase of BiOBr loading (Hamad et al., 2015). However, overdosing of BiOBr can reduce the penetration of fluorescent light and increased the light scattering (Zhang et al., 2014).

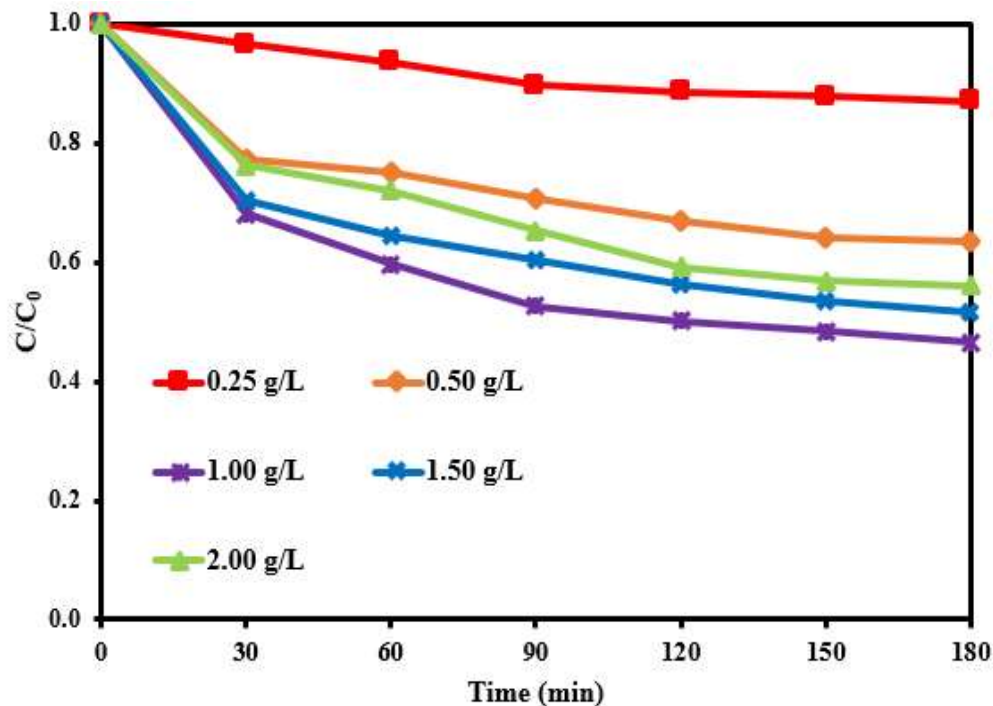


Figure 4.15 Effect of BiOBr loading on the photocatalytic degradation of SSY over flower-like BiOBr hierarchical structures. Conditions: initial SSY concentration= 10 ppm, solution pH= natural pH of SSY and irradiation time= 180 min.

Janani et al. (2015) studied the effect of MRGO (Magnetically Reduced Graphene Oxide)-BiOBr loading on the photodegradation of MB under visible light irradiation for 120 min. The catalysts loading was varied from 0.20 g/L to 1.80 g/L while the initial MB concentration kept constant at 50 ppm. They found that the degradation efficiency increased from 59.44% to 96.84% on increasing the catalyst loading from 0.20 g/L to 1.60 g/L. However, with further increase in the catalyst dosage, a decrease in the degradation efficiency of MB was observed. They also concluded that the increase in the degradation efficiency of MB with increase in the amount of MRGO-BiOBr catalyst was due to numerous availability of active sites on the photocatalyst surface which increased the number of active species produced. For the inhibitory effect was due to turbidity elevation of the suspension and reduce in light penetration resulted scattering effect.

The same incidence also discovered by Kangaraj and Sivakumar (2017) when the effect of SrTiO<sub>3</sub>-BiOBr loading towards the degradation of reactive black 5 was studied. They also provided explanation that the weight of catalyst increased can lead to more number of  $e^-$  and  $h^+$  to participate in redox reaction to form oxidising radicals. Nevertheless, the light penetration onto the catalyst surface was obstructed by further increase in the catalyst loading, which led to low photodegradation efficiency of reactive black 5. Hence, the application of catalyst loading should be optimized in order to ensure sufficient active sites on the catalyst surface and able to fully utilized irradiation light.

#### **4.5.2 Effect of Initial SSY Concentration on Photodegradation of SSY**

As the effect of substrate concentration is of importance in any water treatment process, it is necessary to determine the influence of initial dye concentration on the photodegradation of SSY over flower-like BiOBr hierarchical structures. The SSY dye concentration was varied into 10 ppm, 20 ppm, 40 ppm and 60 ppm for an irradiation time of 180 min, solution pH at 6.0 and catalyst loading of 1.00 g/L.

Figure 4.16 demonstrates the result of initial SSY dye concentration on the photodegradation of SSY in the presence of BiOBr photocatalysts. It can be seen that the increase of initial SSY concentration from 10 ppm to 60 ppm decreased the degradation efficiency from 53.5% to 8.1% after 180 min of fluorescent light irradiation.

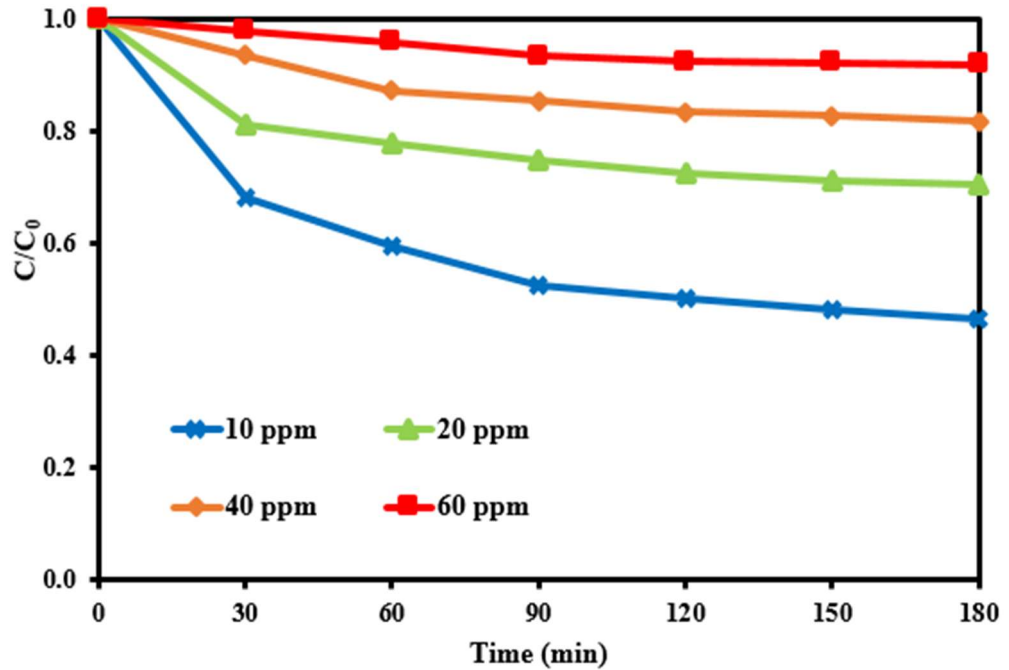


Figure 4.16 Effect of initial SSY concentration on the photocatalytic degradation of SSY over flower-like BiOBr hierarchical structures. Conditions: BiOBr loading= 1.00 g/L, solution pH= natural pH of SSY and irradiation time= 180 min.

The degradation efficiency was associated to the active species generation on the catalyst surface and capability of active species reacting with SSY molecules. As the initial concentration of SSY increased, abundant number of SSY molecules adsorbed on the surface of BiOBr while the constant number of active species formation resulting the probability of active species attacking the SSY molecules decreased (Saadati et al., 2016; Saran et al., 2017). In addition, the high concentrations of SSY, the large amount of adsorbed SSY can compete with  $O_2$  and  $OH^-$  onto the BiOBr surface, which inhibited the generation of active species for photocatalytic degradation (Rajamanickam and Shanthi, 2013). At high SSY concentrations, the path length of the photons entering the dye solution also decreased and resulted to lower photocatalytic activity (Hamad et al., 2016)

Natarajan et al. (2015) investigated the effect of the initial RhB concentration on the photodegradation efficiency at constant catalyst loading of 1.00 g/L. It was observed that the photodegradation efficiency reduced with the increase in RhB dye concentration from 1.2 ppm to 4.8 ppm. They explained that this was owing to the amount of dye adsorption increased as the initial dye concentration increases. As a result, only fewer numbers of photon reached the surface of catalyst and led to the decremented in number of active species formation.

Xiao et al. (2017) also found out that the degradation efficiency of organic pollutants decreased with increasing initial substrate concentration from 5 ppm to 30 ppm when the  $\text{Ag}_3\text{PO}_4/\text{BiOBr}$  loading remained constant (0.50 g/L). They mentioned that the mass number of substrate molecules adsorbed on the surface of  $\text{Ag}_3\text{PO}_4/\text{BiOBr}$  at high initial substrate concentrations can cause less number of photons available to reach the surface of photocatalysts and depressed the generation of active species. Hence, the negative effect was exhibited on degradation efficiency of organic pollutants.

Kanagaraj and Thiripuranthagan (2017) conducted the  $\text{SrTiO}_3\text{-BiOBr}$  photocatalytic experiment at different reactive blue 198 concentrations ranged from 10 ppm to 110 ppm. Their results showed that the degradation efficiency decreased with increasing in the reactive blue 198 concentration. Explanation given by them was that number of active sites were sufficient for the degradation of dye molecules at low concentration. Hence, the degradation efficiency was high at lower initial dye concentration. However, high concentration of dye



prohibited enough light to penetrate through and reached the surface of the catalyst, which resulted to low photodegradation of reactive blue 198.

#### **4.5.3 Effect of Solution pH on Photodegradation of SSY**

The solution pH is one of the important variables in photocatalytic reactions that can influence on the adsorption and degradation efficiencies of the organic pollutants by affecting the surface electrical charge characteristics on the catalysts surface. In this study, pH of the solution was also varied to study its influence towards the degradation of SSY over flower-like BiOBr hierarchical structures. The natural pH of SSY solutions (10 ppm) was pH 6.0. The pH of the solution was varied range from pH 3.0 to pH 9.0 using diluted NaOH or H<sub>2</sub>SO<sub>4</sub> while keeping all other experimental conditions constant (BiOBr loading of 1.00 g/L and SSY concentration of 10 ppm).

Figure 4.17 illustrates the degradation efficiency of SSY over flower-like BiOBr hierarchical structures at different solution pH values. It can be observed that the degradation efficiency increased with increasing irradiation time at all investigated solution pH. After 180 min, the degradation of SSY achieved 73.3% which was maximum at solution pH of 3.0. With further increase of solution pH from pH 6.0 to pH 9.0, the degradation efficiencies diminished from 73.3% (pH 3.0) to 53.5% (pH 6.0), 46.7% (pH 7.0) and 35.1% (pH 9.0).

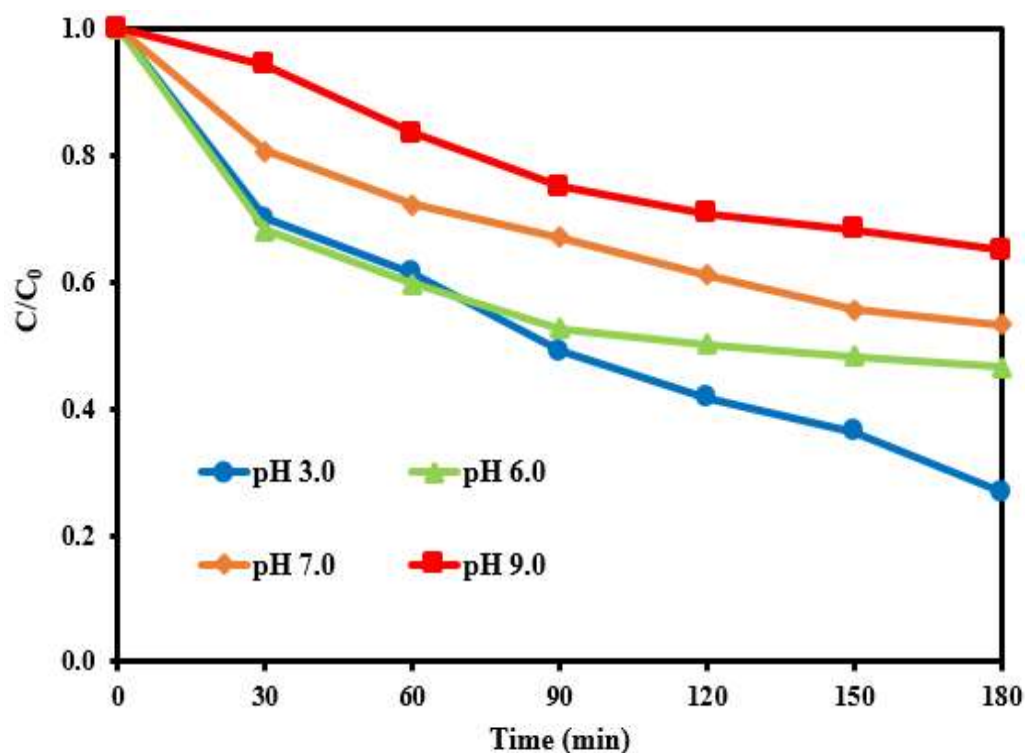


Figure 4.17 Effect of solution pH on the photocatalytic degradation of SSY over flower-like BiOBr hierarchical structures. Conditions: BiOBr loading= 1.00 g/L, initial SSY concentration= 10 ppm and irradiation time= 180 min.

The influence of solution pH on photodegradation efficiency of SSY can be explained on the basis of zero-point charges of BiOBr surface and ionic configuration of SSY. It was noted that at pH 3.0, the surface of flower-like BiOBr hierarchical structures was positively charge due to the zero potential point of BiOBr was 3.4 (Li et al., 2016). The phenomenon of electrostatic attraction between positively charged BiOBr with anionic SSY can lead to maximum degradation efficiency (Ritthidej et al., 2003; Zandipak and Sobhanardakani, 2015). With further increase in the pH value, the degradation efficiency of SSY decreased. This was because at higher pH, both the BiOBr and SSY were negatively charged which led to electrostatic repulsion (Kumar et al., 2017). Hence, the degradation efficiency of SSY decreased at high pH value.

Ahmad et al. (2016) investigated the effect of solution pH on the photocatalytic degradation of RhB over hydrothermally synthesized BiOBr. After 120 min of visible light irradiation, the photocatalytic activity of BiOBr on RhB decreased dramatically at pH 12.0. The suppression of the degradation at high pH was due to the effect of negative charge of BiOBr surface repelled the anionic pollutants for photocatalytic reactions. Moreover, the study of Kanagaraj and Thiripuranthagan (2017) reflected that the degradation of reactive yellow 145 under acidic conditions was higher than in alkaline medium over SrTiO<sub>3</sub>-BiOBr composite. To be precise, the degradation of reactive yellow 145 was effective at pH 3 while suppressed at pH 4.0 to pH 13.0 under constant experimental conditions (initial dye concentration= 50 ppm and catalyst loading= 100 mg). The decrement of degradation percentage in alkaline medium was explained by the repulsion happened between OH<sup>-</sup> ions and the negatively charged surface of the catalyst.

The results obtained of this study was in agreement with investigation reported by Mera et al. (2017). Using solvothermally synthesized BiOBr microspheres, they investigated the effect of solution pH on degradation of methyl orange (MO) under simulated solar radiation. The maximum percentage of MO degradation was obtained at solution pH 2.0. They mentioned that the high degradation efficiency of MO under acidic condition was due to strong electrostatic attraction between the positively charged surface of the BiOBr and the negatively charged MO. However, they also found out that the degradation efficiency of MO over BiOBr microspheres decreased as the solution pH increased from pH 5.0 to pH 9.0. They deduced that the inhibition of the degradation efficiency was caused by the electrostatic repulsion among the

negatively charged BiOBr surface and the negative molecular form of the anionic properties of MO.

#### 4.5.4 Effect of Inorganic Anions on Photodegradation of SSY

The anions are commonly present in water and had a significant effect on photodegradation process of organic pollutants. Thus, the influences of inorganic anions ( $\text{SO}_4^{2-}$ ,  $\text{CO}_3^{2-}$ ,  $\text{NO}_3^-$  and  $\text{Cl}^-$ ) on photocatalytic degradation of SSY over flower-like BiOBr hierarchical structures were investigated using corresponding  $\text{Na}^+$  as cation. The dosage of inorganic anions was set to 1.00 g/L while other experimental conditions were kept constant (BiOBr loading= 1.00 g/L, initial SSY concentration= 10 ppm, solution pH=3.0 and irradiation time= 180 min).

Figure 4.18 presents the effect of inorganic anions on the photocatalytic degradation efficiency of SSY. Based on observations, all anion were observed to retard the photodegradation of SSY in the sequence of  $\text{CO}_3^{2-} > \text{SO}_4^{2-} > \text{NO}_3^- > \text{Cl}^-$ . This can be justified via the basis of reaction of  $h^+$  and  $\bullet\text{OH}$  radicals with anions which behaved as scavengers or quenchers, and hence the photodegradation of SSY was depressed.

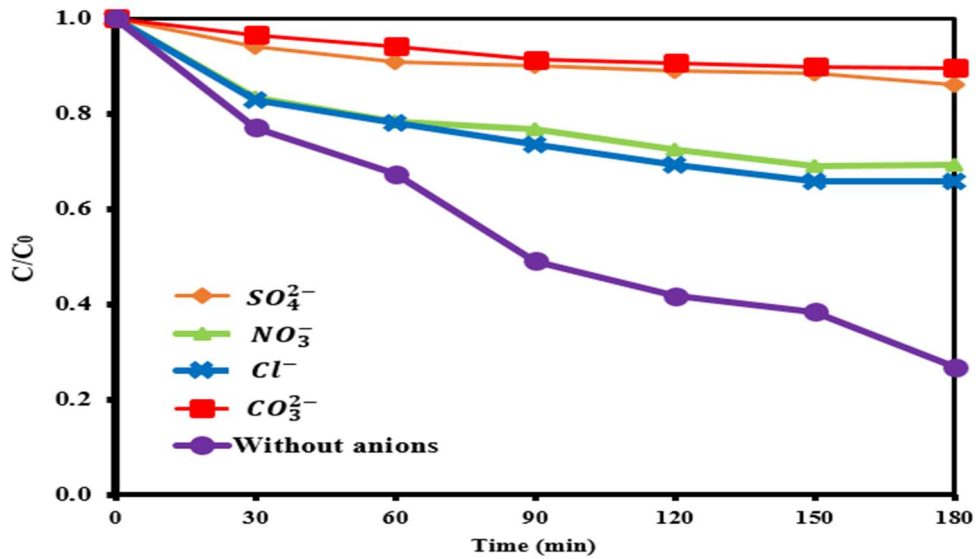


Figure 4.18 Effect of different anions on the photocatalytic degradation of SSY over flower-like BiOBr hierarchical structures. Conditions: BiOBr loading= 1.00g/L, initial SSY concentration= 10 ppm, solution pH= pH 3.0 and irradiation time= 180 min.

The degradation of SSY over flower-like BiOBr was significantly affected by  $CO_3^{2-}$  ions and had the lowest degradation efficiency among all the studied anions. The suppression of photocatalytic performance can be explained as the reaction  $\bullet OH$  radicals by  $CO_3^{2-}$  ions (Bouanimba et al., 2015). In addition, Khataee et al. (2014) also mentioned that the carbonate ions can obstruct the active site on the surface of photocatalysts and deactivated the photocatalysts towards organic pollutants. The mechanism of  $CO_3^{2-}$  ions inhibiting the photocatalytic degradation of SSY is expressed Equation 4.15.



The negative effect of  $SO_4^{2-}$  ions from sodium sulfate ( $Na_2SO_4$ ) on the degradation of SSY can be due to the reaction happened between  $SO_4^{2-}$  ions and

positive  $h^+$  as well as  $\bullet\text{OH}$  radicals (Equation 4.16 to Equation 4.17) (Bouanimba et al., 2015).



Besides, the reason of  $\text{NO}_3^-$  ions inhibited the degradation efficiency of SSY was similar to the inhibition effect of  $\text{SO}_4^{2-}$  ions. The  $\text{NO}_3^-$  ions can quench the positive  $h^+$  of photocatalysts and caused insufficient active species formation to oxidize SSY molecule. However, the degradation performance of SSY with addition of  $\text{NO}_3^-$  ions was relatively better than the addition of  $\text{SO}_4^{2-}$  ions. This was due to the reaction between  $\text{NO}_3^-$  ions and positive  $h^+$  can produce  $\bullet\text{OH}$  radicals which helped in photocatalytic activity (Equation 4.18) (Gao et al., 2015).



It also can be clearly seen that the presence of  $\text{Cl}^-$  ions caused the lowest inhibition effect on the photodegradation efficiency. This was due to the dual effect of  $\text{Cl}^-$  ions in degradation of SSY. When  $\text{Cl}^-$  ions react with  $\bullet\text{OH}$  radicals, it can form chlorine radicals ( $\text{Cl}^{\bullet}$ ). The  $\text{Cl}^{\bullet}$  radicals would have positive effect toward the degradation efficiency of SSY. However, if  $\text{Cl}^{\bullet}$  do not participate in photocatalytic degradation,  $\text{Cl}^-$  ions may act as  $\bullet\text{OH}$  scavenger which will inhibit the SSY degradation (Equation 4.19 to Equation 4.24) (Khataee et al., 2014; Bouanimba et al., 2015; Gao et al., 2015).





Moreover, the inhibition effect of  $\text{SO}_4^{2-}$  and  $\text{CO}_3^{2-}$  ions were greater than  $\text{NO}_3^-$  and  $\text{Cl}^-$  ions. This can be due to the divalence charged of  $\text{SO}_4^{2-}$  and  $\text{CO}_3^{2-}$  ions increased the ionic strength compared to  $\text{NO}_3^-$  and  $\text{Cl}^-$  (Dugandžić et al., 2016). Due to the positively charged surface of BiOBr in acidic condition,  $\text{SO}_4^{2-}$  and  $\text{CO}_3^{2-}$  ions can easily adsorbed to the surface of BiOBr due to electrostatic attraction. Consequently, the surface of BiOBr was mostly occupied by  $\text{SO}_4^{2-}$  and  $\text{CO}_3^{2-}$  ions. Thus, the anionic configuration of SSY was scarcely adsorbed on the surface of BiOBr because of coulumbic repulsion and hence critically reduced the photocatalytic degradation of SSY (Chen et al., 2003).

Xu et al. (2013) investigated the effect of inorganic anions on the degradation of benzotriazole over BiOBr microsphere and BiOBr nanoplates under simulated solar light irradiation. They reported that the inorganic anions can compete with organic pollutant for active sites, which hindered the photocatalytic activity of BiOBr. Besides, the anions can lead to retardation of catalayst effect on the surface of the BiOBr catalyts and deactivated them. Thus, the anion caused a dramatically decrease on the degradation efficiency of benzotriazole over the BiOBr photocatalysts. Using  $\text{BiPO}_4/\text{BiOBr}$  as photocatalyst, Gao et al. (2016) verified the influence of inorganic anions towards the photocatalytic activity for the degradation of Rhodamine B (RhB). From their observation, all the involved anions such as sulphate ions ( $\text{SO}_4^{2-}$ ),

nitrate ions ( $\text{NO}_3^-$ ), chloride ions ( $\text{Cl}^-$ ), bicarbonate ions ( $\text{HCO}_3^-$ ) have negative effects on the photocatalysis. They went further to explain that the photodegradation was inhibited due to the chemical reaction happened between the anions and the active species.

#### **4.6 CATALYTIC ACTIVITY OF RECYCLED FLOWER-LIKE BiOBr HIERARCHICAL STRUCTURES**

The reusability and stability of semiconductor photocatalysts are critical concerns to evaluate their practical value for long term usage in large scale applications. In order to study the reusability of hydrothermally synthesized flower-like BiOBr hierarchical structures. The photocatalytic degradation of SSY experiments were conducted for 4 cycles under optimized conditions (BiOBr loading at 1.00 g/L, initial SSY concentration at 10 ppm and solution pH at 3). After each cycle of photocatalytic degradation of SSY, the suspension was centrifuged and filtered. Then, the used photocatalysts were washed with distilled water and dried at 100 °C for the next cycle usage.

Figure 4.19 shows the use of flower-like BiOBr hierarchical structures after four cycles. It can be observed that the degradation efficiency of flower-like BiOBr hierarchical structures had no significant loss of photocatalytic activity after four cycling run of photodegradation of SSY. This decrease of the photocatalytic ability of flower-like BiOBr hierarchical structures was due to the loss of photocatalysts was very hard to avoid. Moreover, the insignificant decrease of photocatalytic efficiency indicated that the as-synthesized flower-



like BiOBr hierarchical structures can be an efficient photocatalyst which stable for photodegradation of SSY with high reusability potential.

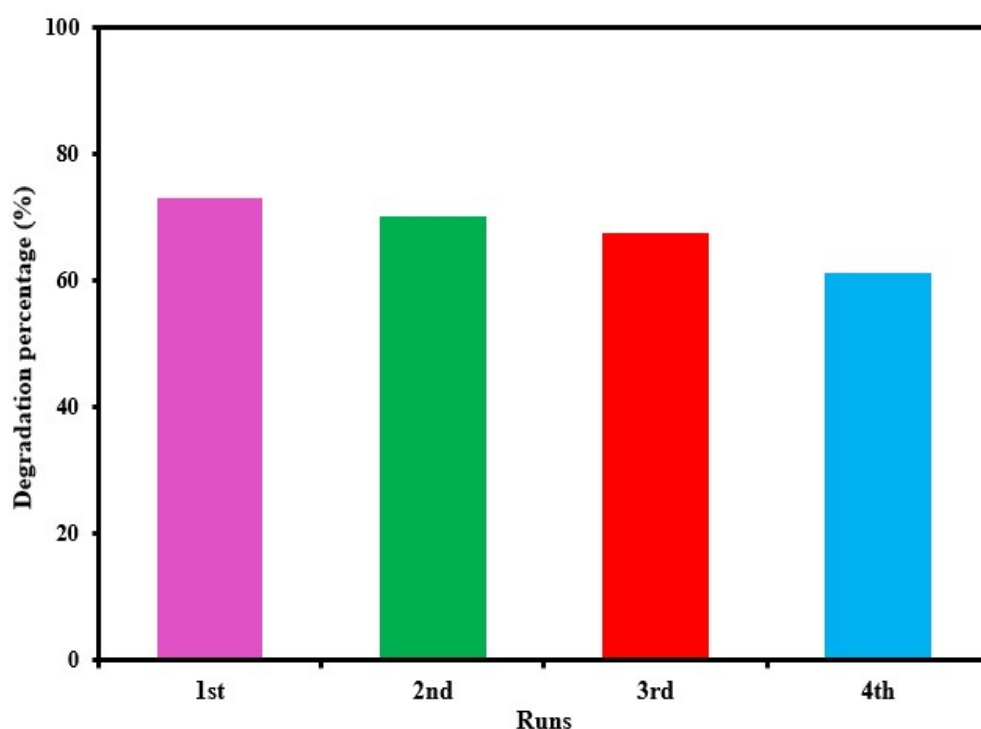


Figure 4.19 Reusability efficiency of flower-like BiOBr hierarchical structures. Conditions: BiOBr loading= 1.00 g/L, SSY concentration= 10 ppm, solution pH= pH 3.0 and irradiation time= 180 min.

In order to investigate the reusability of solvothermally synthesized BiOBr microspheres, Xue et al. (2014) carried out the photodegradation of RhB under visible light irradiation for five cycle. They observed that the photocatalytic activity of as-prepared BiOBr decreased with the increasing of experiments cycle. 71% of RhB were degraded after five cycles of photocatalytic activity compared to 89% RhB were degraded for the first cycle. They claimed that the as-synthesized BiOBr microspheres via solvothermal method acquired with outstanding stability and recyclability which have potential application in environment remediation. Liu and Wu (2015) studied the repetitive use of Bi/BiOBr on MO degradation. The results showed that there was no significant decrease of photocatalytic efficiency on the degradation of MO after four

recycling tests. With the result observed, they also concluded that solvothermally synthesized Bi/BiOBr have good photocorrosion resistance and great stability. The recycled experiments were carried out by Li et al. (2015) to evaluate the stability of SiO<sub>2</sub>-BiOBr photocatalyst on photodegradation of RhB under visible light irradiation. Based on the observations, the photocatalytic ability of SiO<sub>2</sub>-BiOBr photocatalysts did not show significant loss which indicated that SiO<sub>2</sub>-BiOBr was a stable photocatalyst in the photocatalysis reaction system.

Li et al. (2015) examined the stability of hydrothermally synthesized BiOBr photocatalysts on photocatalytic degradation of MO under simulated solar light irradiation. Based on their analysis, they discovered that no significant loss of photocatalytic activity after three recycling reaction. They explained the decrement of photocatalytic efficiency during recycling experiment was due to the decrease of the surface adsorption ability and the photocatalytic ability of as-prepared BiOBr. Reusability performance of solvothermally synthesized BiOBr was determined by Wang et al. (2015) on photocatalytic degradation of RhB. Their result showed that BiOBr microspheres exhibited excellent photostability after the recycling test. They deduced that as-synthesized BiOBr has high photocorrosion resistance and stability during the photocatalytic degradation of RhB.

## 4.7 KINETIC STUDY

### 4.7.1 Determining the Kinetic Order

In heterogeneous photocatalytic process, rates of reaction are normally proportional to the adsorption of reactants and desorption of products on the photocatalyst surface. According to Gaya (2014), the integral treatment of differential rate equations gave integrated rate laws which can be shown by the disappearance of the organic compound that undergoing photocatalytic degradation. On the other words, the equation of reaction rate included concentration where  $-r$  was the rate of disappearance of reactant as shown in Equation 4.25 (Gaya, 2014).

$$-r = \frac{d[A]}{dt} = k [\text{concentration of reactant}]^n \quad (4.25)$$

where  $k$  is the rate constant,  $n$  is the order and  $t$  is the reaction time (min).

Hence, determination of the kinetic order on the photocatalytic degradation of SSY was conducted. Table 4.1 lists the rate laws which relate to zero-, first-, second- and third-order reactions.

Table 4.1 Reaction order and rate law for a reaction involving a single reactant (Gaya, 2014).

Reaction orders	Rate laws	Integrated Equation	Reaction rate units
Zero-order	$-r = kC_{SSY}^0$	$C_{SSY} = -C_{SSY0} + kt$	$\{k\} = \text{mol/L} \cdot \text{min}$
First-order	$-r = kC_{SSY}^1$	$\ln \frac{C_{SSY0}}{C_{SSY}} = kt$	$\{k\} = 1/\text{min}$
Second-order	$-r = kC_{SSY}^2$	$\frac{1}{C_{SSY}} = kt + \frac{1}{C_{SSY0}}$	$\{k\} = \text{L/mol} \cdot \text{min}$
Third-order	$-r = kC_{SSY}^3$	$\frac{1}{C_{SSY}^2} = kt + \frac{1}{C_{SSY0}^2}$	$\{k\} = (\text{L/mol})^2 \cdot \text{min}^{-1}$

Where  $-r$  = reaction rate  
 $k$  = observed rate constant  
 $C_{SSY}$  = concentration of SSY at time  $t$  (ppm)  
 $C_{SSY0}$  = initial SSY concentration (ppm)  
 $t$  = reaction time (min)

After the experiments, the obtained results were substituted into each integrated equation indicating different reaction rate orders. Plotted graphs which equivalent to the results obtained for each equation of zero-, first-, second- and third order are presented in Figure 4.20, 4.21, 4.22 and 4.23, respectively.

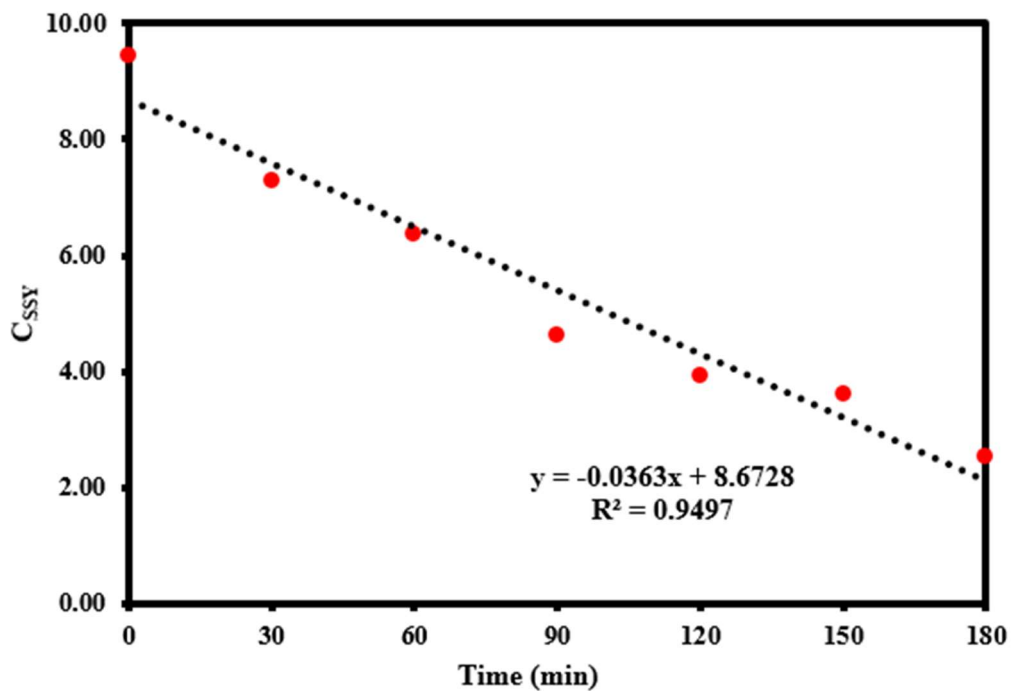


Figure 4.20 Fitting for zero-order reaction. Conditions: BiOBr loading= 1.00 g/L, SSY concentration= 10 ppm and solution pH= pH 3.0.

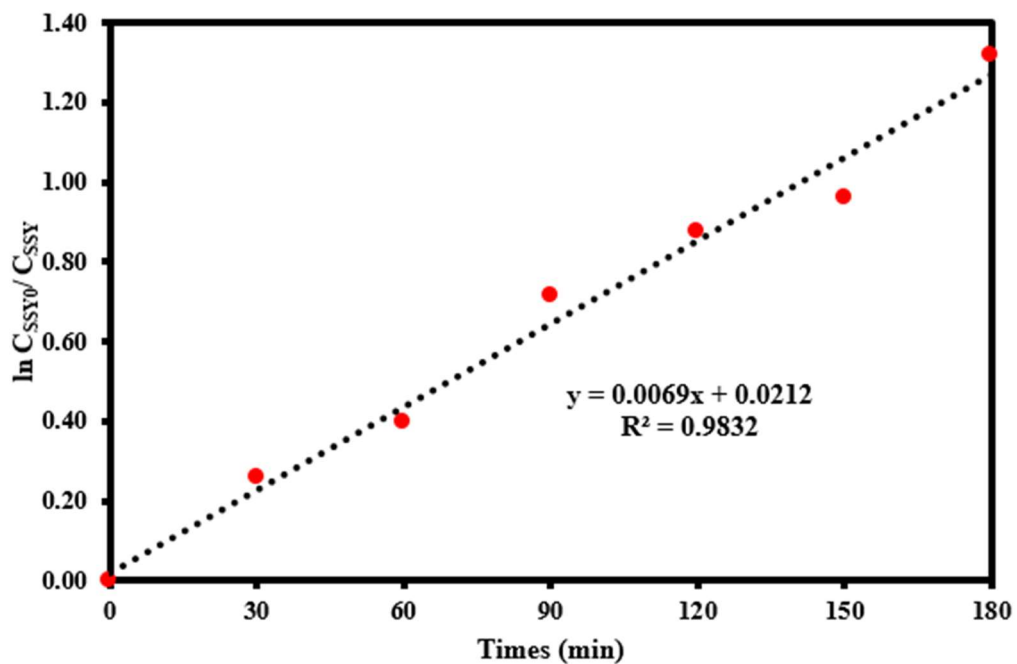


Figure 4.21 Fitting for first-order reaction. Conditions: BiOBr loading= 1.00 g/L, SSY concentration= 10 ppm and solution pH= pH 3.0.

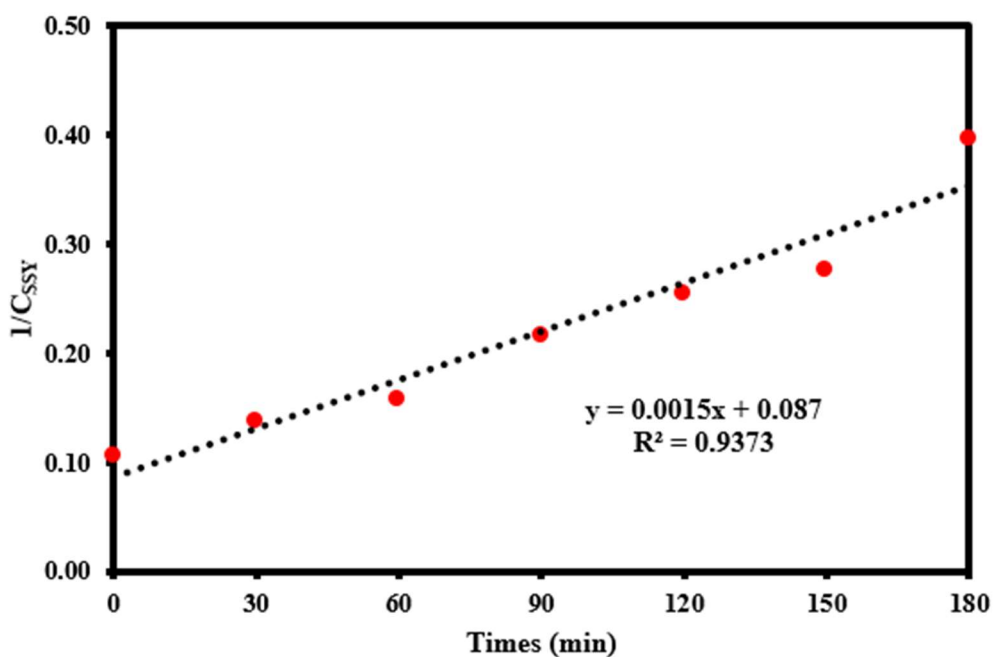


Figure 4.22 Fitting for second-order reaction. Conditions: BiOBr loading= 1.00 g/L, SSY concentration= 10 ppm and solution pH= pH 3.0.

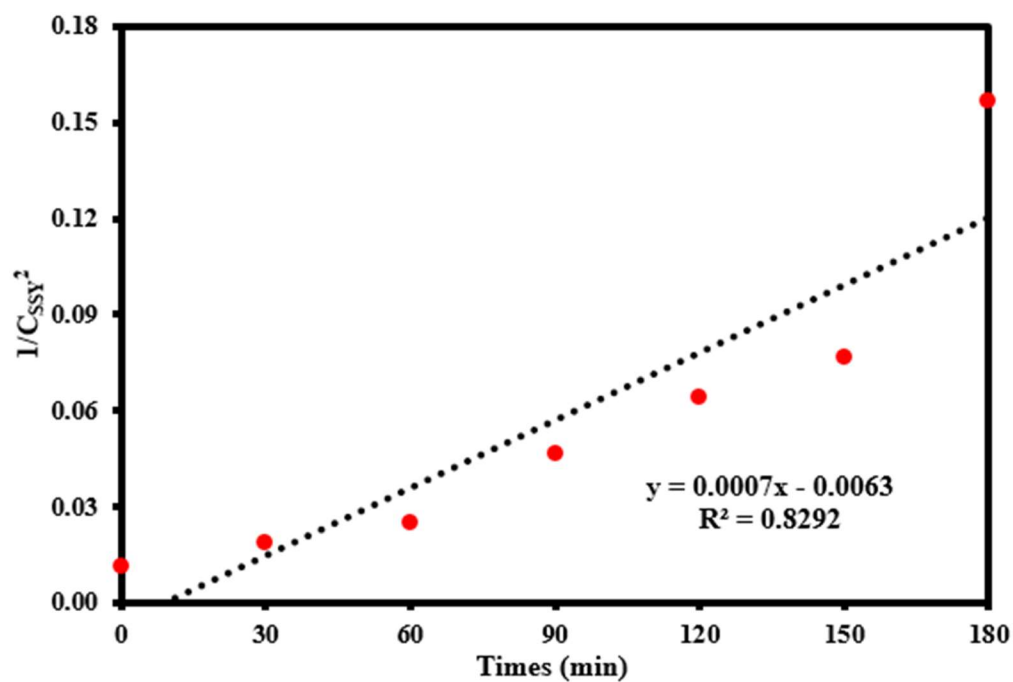


Figure 4.23 Fitting for third-order reaction. Conditions: BiOBr loading= 1.00 g/L, SSY concentration= 10 ppm and solution pH= pH 3.0.

The value of rate constant ( $k$ ) was obtained from the slope from every corresponding graph and the correlation coefficient ( $R^2$ ) value from different corresponding graph and are listed in Table 4.2.

Table 4.2 Table of rate constants ( $k$ ) and correlation coefficient ( $R^2$ ) obtained from different reaction order graphs.

Reaction order	Rate constant ( $k$ )	Correlation coefficient ( $R^2$ )
Zero-order	-0.0363	0.9497
First-order	0.0069	0.9832
Second-order	0.0015	0.9373
Third-order	0.0007	0.8292

Based on Table 4.2, the first-order reaction kinetic gave the optimum rate constant as well as higher correlation coefficient ( $R^2$ ) which was 0.9832. Hence, it was proven that photodegradation of SSY over flower-like BiOBr hierarchical structures under fluorescent light irradiation fitted into first-order reaction. In addition, pseudo first-order reaction has also been successfully used to express various types of organic pollutant degraded by BiOBr in the past few years (Lie et al., 2013; Chang et al., 2014; Zhu et al., 2016; Meng et al., 2018).

#### 4.7.2 Langmuir-Hinshelwood Model

The degradation reaction taking place in photodegradation of SSY over flower-like BiOBr hierarchical structures is designated as a heterogeneous catalytic reaction. Many researchers reported that the first order kinetic of a heterogeneous catalytic reaction commonly accommodated by the Langmuir-Hinshelwood (L-H) model (Nathaji et al., 2016; Bora and Mewada, 2017; Lv et al., 2017; Kanagaraj et al., 2017). Fitting for SSY degradation kinetic order resulted in a first-order reaction indicated that the L-H model can be applied for kinetic reaction of degradation of SSY over as-synthesized BiOBr (Equation 4.26).

$$r = -\frac{dC_{SSY}}{dt} = \frac{kKC_{SSY}}{1+KC_{SSY}} \quad (4.26)$$

where,  $r$  is the rate of reaction of SSY degradation (ppm/min),  $C_{SSY}$  is SSY concentration (ppm),  $t$  is the irradiation time,  $k$  is the reaction rate constant (ppm/min) and  $K$  is the adsorption equilibrium of SSY (1/ppm).

As the L-H model is based on the assumption that both involved molecules adsorbed and underwent a bimolecular reaction. Moreover, the model assumed the reaction steps to be the adsorption of reactants, surface reaction and desorption of products. The expression can be integrated and rearranged as Equation 4.27 (Ahmad, 2013).

$$\ln \frac{C_{SSY0}}{C_{SSY}} + K(C_{SSY0} - C_{SSY}) = kKt \quad (4.27)$$

When SSY concentration is in millimolar, the term  $K(C_{SSY0} - C_{SSY}) < 1$ , the term  $K$  can be ignored and the degradation of SSY follows an apparent first order equation as follow (Equation 4.28) (Hamad et al., 2015):

$$\ln \frac{C_{SSY0}}{C_{SSY}} = kKt = k_{app}t \quad (4.28)$$

where,  $k_{app} = kK$  and is the apparent rate constant for first order equation.

The above model had been used for kinetics of photocatalytic degradation in this study and the degradation rate constants that reported were calculated based on graphical method using the first-order differential equation. The photodegradation of SSY at different solution pH were performed with BiOBr loading of 1.00 g/L and initial SSY concentration of 10 ppm and the results are presented in Figure 4.24. It can be observed that when  $\ln (C_{SSY0}/C_{SSY})$  was plotted as a function of irradiation time, the apparent rate constant ( $k_{app}$ ) can be calculated from the slope of resulting linear equation. The  $k_{app}$  and correlation coefficient ( $R^2$ ) were recorded in Table 4.3.



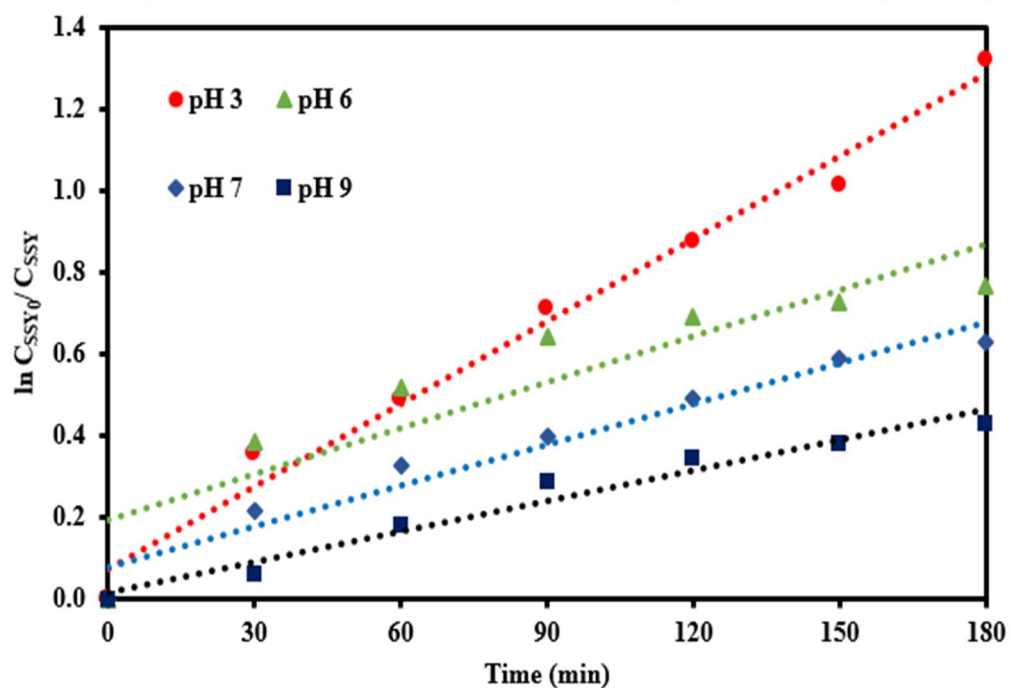


Figure 4.24 Plots of  $\ln C_{SSY0}/C_{SSY}$  versus time for SSY degradation under different solution pH. Conditions: BiOBr loading= 1.00 g/L and initial SSY concentration= 10 ppm.

Table 4.3 Value of  $k$  and  $R^2$  under different solution pH.

Solution pH	$k$ ( $\text{min}^{-1}$ )	$R^2$
3	0.0069	0.9832
6	0.0038	0.8177
7	0.0033	0.9559
9	0.0025	0.9643

It can be observed that the solution pH increased from 3.0 to 9.0, the  $k$  values decreased. Such trend was also observed by Chang et al. (2012) on the photodegradation of RhB over BiOBr (experimental conditions: initial RhB concentration= 7.15 ppm, and catalyst loading= 0.40 g/L). They observed that the rate constant ( $k$ ) decreased dramatically with the increasing of solution pH.

The observation can be explained by the surface of BiOBr tended to be negatively charged and resulted electrostatic repulsion force occurred. This repulsion restricted the adsorption of anion SSY on the surface of BiOBr leading, to low rate of reaction.

#### **4.8 OPTIMIZATION STUDIES USING RESPONSE SURFACE METHODOLOGY (RSM)**

A better understanding of the effects that influenced the photodegradation of SSY over flower-like BiOBr hierarchical structures, method of one-factor-at-a-time experiments have been carried out by changing a parameter while keeping the other parameters constant (Section 4.5). However, this method does not account the relations within the operating parameters and large number of experiments have to be conducted (Ai et al., 2015). Compared to one-factor-at-a-time method, response surface methodology (RSM) is more efficient and reliable as it accounted the interaction effects between studied parameters by conducting minimum number of experiments and much more easier to obtain the optimal conditions (Feilizadeh et al., 2015). Thus, RSM from Design Expert version 6.0 (StatEase, Inc., USA) was used to determine the optimum value of the studied parameters (catalyst loading, initial dye concentration, solution pH and irradiation time) in this study.

The experiment design for the optimization of SSY degradation was studied via central composite design (CCD) of RSM. Based on the data obtained from one-factor-at-a-time, four factors had been chosen to fit into the CCD. The first factor was BiOBr loading ranged from 0.50 g/L to 2.00 g/L, the second was the initial SSY concentration ranging from 10 ppm to 50 ppm, the third was solution pH ranging from pH 3.0 to pH 9.0 and the last was the fluorescent light

irradiation time ranging from 60 min to 180 min. The percentage of SSY degradation (% Y) will be the desired response in the design of experiment. Table 4.4 shows the 30 sets of experiments desired from CCD model based on the studied factors.

Table 4.4 Experiment matrix and the response values.

Run	Factors				Degradation %
	Catalysts Loading (g/L)	Initial Conc. (ppm)	Solution pH	Irradiation Time (min)	
1	2.00	10.00	9.00	180.00	33.10
2	1.25	30.00	6.00	120.00	27.90
3	2.00	10.00	9.00	60.00	15.90
4	1.25	30.00	6.00	180.00	33.60
5	1.25	30.00	6.00	120.00	26.70
6	0.50	10.00	3.00	180.00	60.90
7	2.00	50.00	9.00	60.00	8.20
8	1.25	30.00	6.00	120.00	27.50
9	0.50	30.00	6.00	120.00	16.50
10	0.50	50.00	9.00	180.00	11.80
11	1.25	50.00	6.00	120.00	16.20
12	1.25	30.00	6.00	120.00	24.30
13	2.00	10.00	3.00	180.00	67.60
14	0.50	10.00	3.00	60.00	31.90
15	1.25	10.00	6.00	120.00	46.50
16	2.00	30.00	6.00	120.00	20.30
17	2.00	10.00	3.00	60.00	36.60
18	2.00	50.00	3.00	60.00	20.70
19	0.50	10.00	9.00	180.00	28.80
20	1.25	30.00	9.00	120.00	16.90
21	2.00	50.00	9.00	180.00	13.10
22	1.25	30.00	6.00	60.00	15.40
23	1.25	30.00	6.00	120.00	28.00
24	1.25	30.00	6.00	120.00	29.20
25	2.00	50.00	3.00	180.00	34.90
26	1.25	30.00	3.00	120.00	38.80
27	0.50	50.00	9.00	60.00	5.70
28	0.50	50.00	3.00	60.00	16.90
29	0.50	10.00	9.00	60.00	12.30
30	0.50	50.00	3.00	180.00	30.30

The data obtained were then analysed via regression equation from the analysis of variances (ANOVA) suggested by the Design-Expert software to determine the applicability of the model. Table 4.5 shows the lack of fit test summary suggested from the software.

Table 4.5 Analyses for model fitting.

Model	Sum of Square	DF	Mean Square	F value	Prob > F	
Linear	695.965	20	34.79825	12.55952	0.0053	
2FI	268.581	14	19.18437	6.92410	0.0215	
Quadratic	85.676	10	8.56758	3.09224	0.1123	Suggested
Cubic	11.867	2	5.93374	2.14162	0.2129	Aliased

The Design-Expert software indicated that the quadratic model was the best model fitted to the response. From the data listed in Table 4.5, the quadratic model for SSY degradation over flower-like BiOBr hierarchical structure was being formulated in terms of coded factors presented in Equation 4.29 as:

$$\begin{aligned}
 \% Y = & 26.36 + 1.96X_i - 9.77X_{ii} - 10.71X_{iii} + 8.36X_{iv} - 0.44X_iX_{ii} + 2.68X_{ii}X_{iii} - \\
 & 3.44X_{ii}X_{iv} - 0.51X_iX_{iii} + 0.14X_iX_{iv} - 2.68X_{iii}X_{iv} - 7.04X_i^2 + \\
 & 5.91X_{ii}^2 + 2.41X_{iii}^2 - 0.94X_{iv}^2
 \end{aligned} \tag{4.29}$$

where  $X_i$  is the code factor for BiOBr loading,  $X_{ii}$  is the initial SSY concentration,  $X_{iii}$  represents solution pH and  $X_{iv}$  is the fluorescent light irradiation time. The significance of each factor in Equation 4.29 was determined statistically by the software using ANOVA and the results are tabulated in Table 4.6.

Table 4.6 ANOVA for the quadratic model for SSY degradation.

Source	Sum of Squares	DF	Mean Square	F value	Prob > F
Model	5719.95	14	408.57	61.58	<0.0001
$X_i$ - Catalyst loading	69.23	1	69.23	10.43	0.0056
$X_{ii}$ - Initial concentration	1716.98	1	1716.98	258.77	<0.0001
$X_{iii}$ - pH value	2065.10	1	2065.1	311.23	<0.0001
$X_{iv}$ - Radiation time	1258.35	1	1258.35	189.65	<0.0001
$X_i X_{ii}$	3.15	1	3.15	0.47	0.5013
$X_i X_{iii}$	4.10	1	4.10	0.62	0.4440
$X_i X_{iv}$	0.33	1	0.33	0.050	0.8264
$X_{ii} X_{iii}$	115.03	1	115.03	17.34	0.0008
$X_{ii} X_{iv}$	189.75	1	189.75	28.60	<0.0001
$X_{iii} X_{iv}$	115.03	1	115.03	17.34	0.0008
$X_i^2$	128.55	1	128.55	19.37	0.0005
$X_{ii}^2$	90.38	1	90.38	13.62	0.0022
$X_{iii}^2$	15.00	1	15.00	2.26	0.1535
$X_{iv}^2$	2.31	1	2.31	0.35	0.5641
Residual	99.53	15	6.64		
Lack of Fit	85.68	10	8.568	3.092	0.1123
Pure Error	13.85	5	2.77		
Cor Total	5819.48	29			

Table 4.6 Continued

R <sup>2</sup> = 0.9829	Adj R <sup>2</sup> =0.9669	Adequate = 33.819	Std. Dev. = 2.58	Mean = 26.55	C.V. % = 9.70
-------------------------	-------------------------------	----------------------	---------------------	-----------------	------------------

As stated by the software, the model F-value of 61.58 implied that the model was significant while there was only a 0.01% chance that “Model F-Value” this large could occur due to noise. Besides, the values of Prob > F less than 0.05 indicating the model terms are significant. Hence, studied factors  $X_i$ ,  $X_{ii}$ ,  $X_{iii}$  and  $X_{iv}$  were significant model terms. Moreover, the lack of fit F-value of 3.09 implied the lack of fit was not significant relative to the pure error and 11.23% chance that a lack of fit F-value this large could occur due to noise. It was reported by Karimi et al. (2016) that insignificant lack of fit was good and thus this model was fitted for removal of SSY by photocatalysis. The RSM also used by Mosleh et al. (2018) to study the optimization for photodegradation of methylene blue (MB). They noticed that Prob > F value was less than the confidence level (0.05) and the value for lack of fit was higher than 0.05, which demonstrated the significance and adequacy of the model. In conclusion, the model suggested by the software was valid and appropriate for the photodegradation of SSY over flower-like BiOBr hierarchical structures.

The response for the quadratic model for SSY degradation can also be represented in a three-dimensional plot which was the 3D surface plot. The response of two manipulating variables and constant variables can be reflected through 3D surface plot. Figure 4.25 shows the 3D surface plots of the interaction between solution pH and BiOBr catalyst loading on SSY degradation efficiency at constant initial SSY concentration and irradiation time. The

interaction of pH value and BiOBr loading exhibited a slanting plane in the 3D surface plots. As reflected from the figure, there was an increase in the degradation efficiency of SSY with decreasing of solution pH either in low level of BiOBr loading or high level of BiOBr loading. Simultaneously, the effect of BiOBr loading on the degradation efficiency of SSY has similar trends whether solution pH at the low level or at the high level. The degradation efficiency of SSY increased with increasing of BiOBr loading but decrease while the BiOBr loading beyond the optimum level. The obtained results was in a reasonable agreement with the results obtained from one-factor-at-a-time experiments.

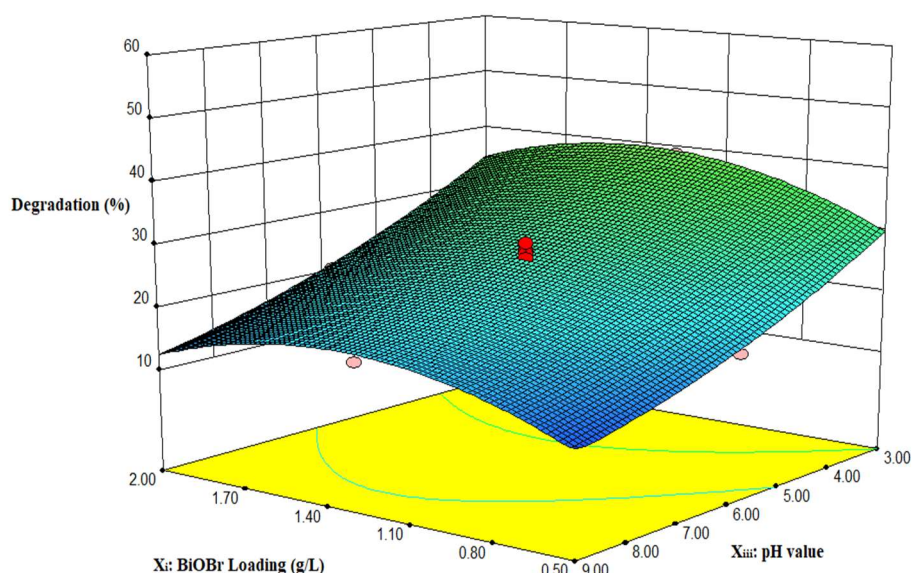


Figure 4.25 3D surface plot indicating the effect of catalyst loading and solution pH on the percentage of SSY degradation at constant initial SSY concentration and fluorescent light irradiation time.

The effects of initial SSY concentration and BiOBr loading on the degradation efficiency of SSY are shown in Figure 4.26. Based on the figure, the interaction effects of initial SSY concentration and BiOBr loading on the degradation efficiency of SSY can be observed to have a similar trend with the

interaction effects of solution pH and BiOBr loading. The degradation percentage of SSY increased when the initial SSY concentration decreased. This observations obeyed well with the results obtained from the study on the effect of operating parameters. Higher initial dye concentration led to low degradation efficiency compared to lower initial dye concentration. This was because large number of dye molecule at high dye concentrations can obstruct the light penetration and scattered onto the surface of photocatalysts. In addition, large amount of adsorbed dye can block the active sites for reaction with  $\text{OH}^-$  and  $\text{O}_2$ . On the other hand, the degradation efficiency of SSY increased with the increasing of BiOBr loading and decrease when the catalyst loading achieved its optimum value no matter in low initial SSY concentration or high SSY concentration.

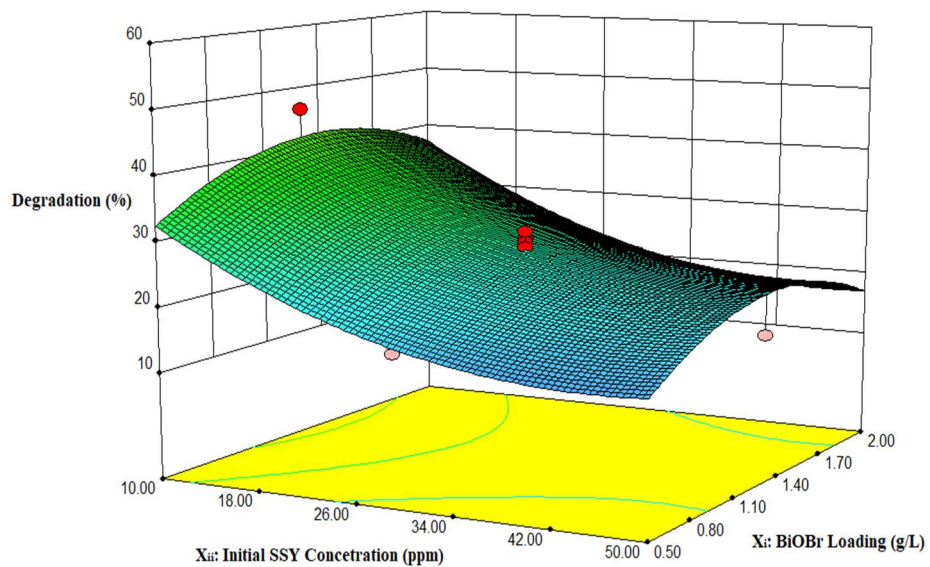


Figure 4.26 3D surface plot indicating the effect of initial SSY concentration and catalyst loading on the percentage of SSY degradation at constant solution pH and fluorescent light irradiation time.



The interaction between initial SSY concentration and solution pH is shown in the Figure 4.27 at constant catalyst loading and irradiation time. From the 3D surface plot, the influence of solution pH on degradation of SSY was highly significant. The degradation efficiency of SSY reached the highest when both the initial dye concentration and pH value at lowest value. On the other hand, when the pH value increased toward higher pH value, at low initial concentration, the degradation of SSY decreased significantly. However, the degradation percentage slightly decreased with the increase of initial SSY concentration when the solution pH remained at 3.0. Such result also can be observed for the effect of pH as investigated in one-factor-at-a-time experiments, where the highest degradation efficiency was at pH 3.0. This can be due to the electrostatic attraction between positively charge BiOBr and anionic SSY, which enhanced the photodegradation of SSY. However, at high initial SSY concentration and high solution pH exhibited to lower SSY degradation efficiency. At higher pH, the anionic SSY molecule unable to attach on the surface of deprotonated BiOBr due to repulsive force, which led to a decrement in the degradation efficiency of SSY.

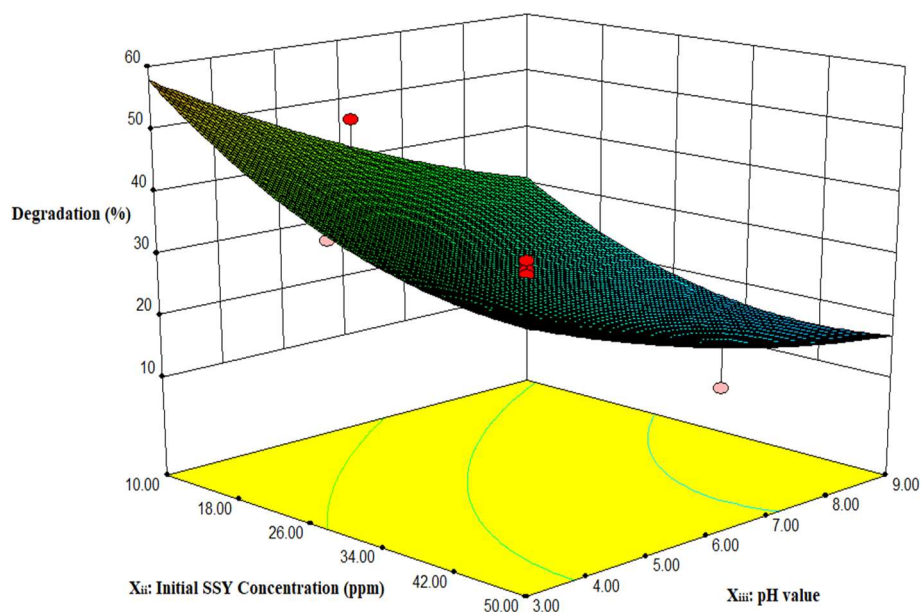


Figure 4.27 3D surface plot indicating the effect of initial SSY concentration and solution pH on the percentage of SSY degradation at constant BiOBr loading and fluorescent light irradiation time.

Figure 4.28 reflects the interactions of BiOBr loading and fluorescent light irradiation time on the photocatalytic degradation efficiency of SSY. The degradation of SSY increased gradually with the irradiation period increased from 60 min to 180 min. The effect of catalyst loading also exhibited an arch-shaped trend in the 3D surface plots. The optimum catalyst loading on the plot will be the local maximum point which was 1.30 g/L and the longer the irradiation time the higher the degradation efficiency of SSY. As stated before, the degradation of SSY decreased at high loading of BiOBr is due to the excess catalyst can block the light penetration and caused light scattering. However, as the irradiation time increased, the degradation efficiency increased while the catalyst loading remained at high level. This can due to the light have sufficient time to penetrate through the bulk catalyst and helped in photocatalytic activity

of BiOBr on degradation of SSY. In addition, when undergo a longer reaction time, the contact time of BiOBr and light can increase and resulted more active species to produce. Large amount of generated active species generated can aid in decomposing SSY molecule which resulting degradation efficiency of SSY increased.

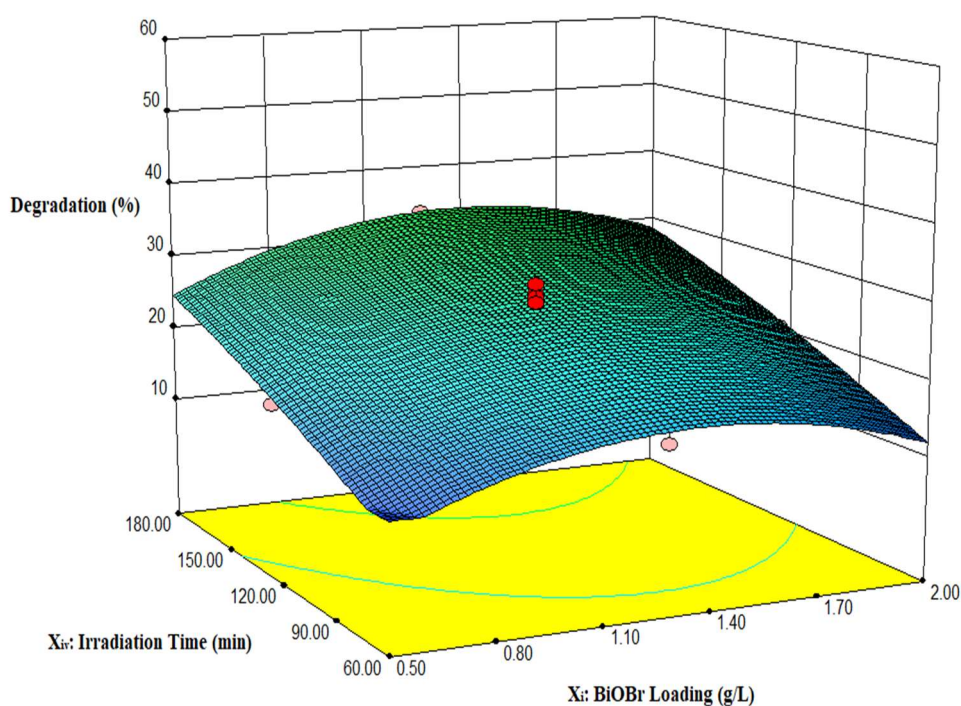


Figure 4.28 3D surface plot indicating the effect of BiOBr loading and fluorescent light irradiation time on the percentage of SSY degradation at constant initial SSY concentration and solution pH.

Figure 4.29 presents the effects of initial SSY concentration and fluorescent light irradiation time. The degradation percentage achieved 50% when initial SSY concentration at 10 ppm and irradiation time at 180 min. However, with the increasing of initial SSY concentration, the photodegradation percentage of SSY decreased significantly no matter at 60 min or 180 min of irradiation period. This was because at lower dye concentration, no obstruction for light penetration and allowed surface of BiOBr to excite by light leading to

active species generation. When the reaction time was prolonged, there were enough time for active species to oxidize the SSY molecule and hence higher photodegradation efficiency of SSY achieved. Contrary, at higher initial SSY concentration and shorter reaction time, the degradation percentage of SSY was depressed. This can be due to the light penetration blocked by mass number of dye molecule, the production of active species became slower and lesser as well as the insufficient contacting time for active species and SSY molecule. Although the reaction time was prolonged, the degradation efficiency of SSY still depressing due to the large number of SSY molecule competed for active species during the photocatalytic activity.

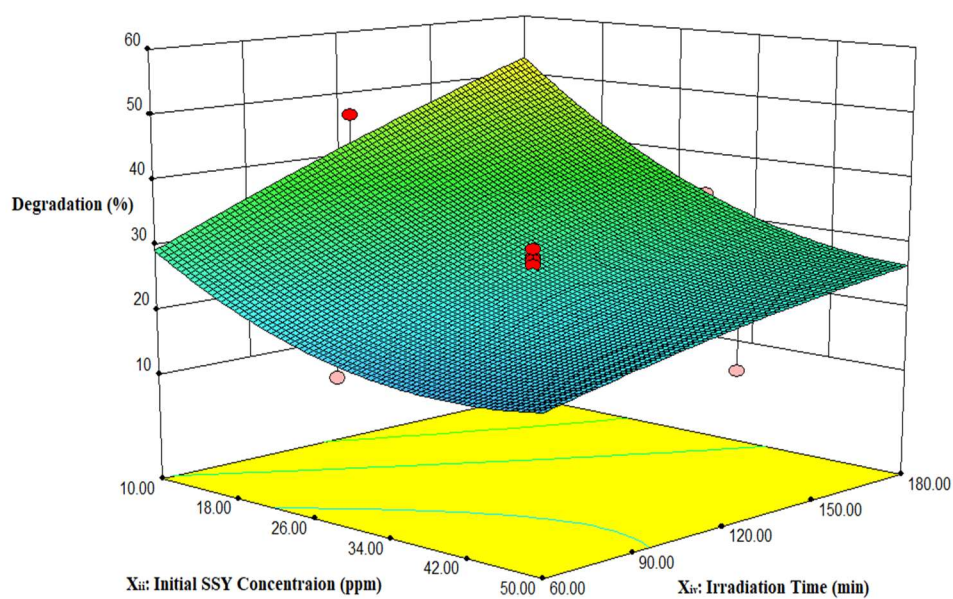


Figure 4.29 3D surface plot indicating the effect of initial SSY concentration and fluorescent light irradiation time on the percentage of SSY degradation at constant BiOBr loading and solution pH.

Lastly, the 3D surface plot for the influence of solution pH and fluorescent light irradiation time shown in Figure 4.30, with solution pH set from pH 3.0 to pH 9.0 and irradiation time varied from 60 min to 180 min. The efficiency of SSY degradation at pH 3.0 increased as the irradiation time increased. This can credit to the electrostatic attraction of positively charged flower-like BiOBr and the anionic configuration of SSY. The longer the reaction time, the longer the electrostatic attraction existed and resulted the SSY molecule able to be decomposed on the surface of BiOBr by the generated active species. Hence, after 180 min of reaction time, the photocatalytic degradation efficiency of SSY was relatively excellent compared to the degradation efficiency after 60 min of reaction time. On the other hand, the degradation percentage of SSY at high solution pH hindered due to the electrostatic repulsive force of deprotonated BiOBr and anion configuration of SSY. The repulsive force causing the SSY scarcely adsorbed on the surface of BiOBr either longer reaction time or shorter reaction time. Hence, the efficiency of SSY degradation from 60 min to 180 min do not show a significantly change.

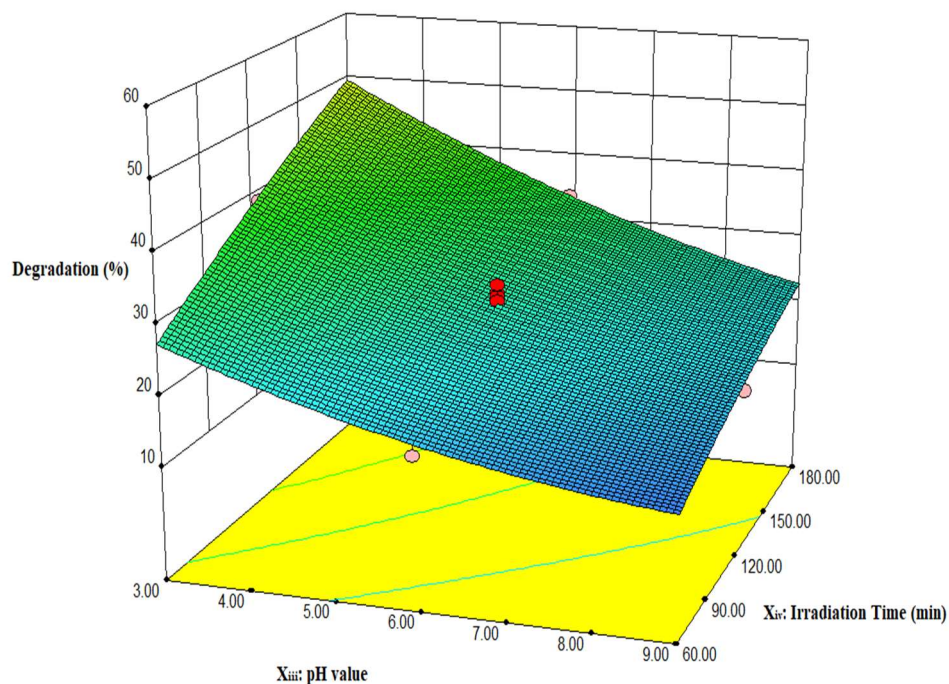


Figure 4.30 3D surface plot indicating the effect of solution pH and fluorescent light irradiation time on the percentage of SSY degradation at constant BiOBr loading and initial SSY concentration.

In order to determine the optimum conditions in this system, the system required to set the goals for the studied operating parameters as listed in Table 4.7. In this study, the BiOBr loading was set in range due to the amount can directly affect the degradation efficiency of SSY. In addition, the effect of initial SSY concentration and solution pH were set at the minimum value. This was because the photodegradation of SSY over flower-like BiOBr hierarchical structures was able to achieve excellent performance at low pollutant concentration and acidic condition. The fluorescent light irradiation was set to be maximum so that the reaction time of BiOBr and SSY molecule prolonged in order to have a better photocatalytic activity. Moreover, the response

degradation percentage was maximized in this system in order to obtain the optimum operating parameters on the degradation of SSY in this study.

Table 4.7 Factors and their desired goal for optimizing SSY degradation

<b>Factors</b>	<b>Goal</b>	<b>Lower limit</b>	<b>Upper limit</b>
Catalyst loading (g/L)	In range	0.5	2.0
Initial dye concentration (ppm)	minimize	10	50
Solution pH	minimize	3	9
Irradiation time (min)	maximize	60	180
Degradation (%)	maximize	5.7	67.6

Based on the criteria listed in Table 4.7, the Design-Expert software recommended ten sets of experimental solution which would give the highest degradation percentage of SSY. The recommended sets of experimental operating parameters is shown in Table 4.8.

Among ten listed experimental sets, the bold solution recommended by the system was performed experimentally. The experiment was conducted at condition of BiOBr loading at 1.31 g/L, initial SSY concentration at 10 ppm, solution pH at pH 3.0 and 180 min of fluorescent light irradiation time. By following the suggestion parameters, 69.7% of SSY degraded after the experimental work. This result obtained is lower than the predicted percentage as suggested by the software but the result still valid due to only 1.9% different from the predicted percentage. Hence, the maximum SSY degradation can be approached by applying the optimum factor values suggested by the software.

Table 4.8 Experimental solution as given by the software

<b>Solutions</b>	<b>Catalyst loading (g/L)</b>	<b>Initial dye concentration (ppm)</b>	<b>Solution pH</b>	<b>Irradiation time (min)</b>	<b>Degradation (%)</b>	<b>Desirability</b>
1	1.31	10.00	3.00	180	71.6	1
2	1.52	10.00	3.00	180	71.6	1
3	1.6	10.00	3.00	180	71.3	1
4	1.39	10.00	3.00	180	71.7	1
5	1.35	10.00	3.00	180	71.6	1
6	1.02	10.00	3.00	180	69.8	1
7	1.77	10.00	3.00	180	69.8	1
8	1.72	10.00	3.00	180	70.5	1
9	1.85	10.00	3.00	180	69.3	1
10	1.2	10.00	3.00	180	71.1	1



#### 4.9 PHOTOCATALYTIC DEGRADATION OF SSY OVER FLOWER-LIKE BiOBr HIERARCHICAL STRUCTURES UNDER SUNLIGHT IRRADIATION

The photodegradation of SSY over flower-like BiOBr hierarchical structures under solar irradiation was carried out. For comparison, BiOBr nanosheets was chosen in this experiment. Figure 4.31 demonstrates the photocatalytic activity of as-synthesized flower-like BiOBr hierarchical structures and BiOBr nanosheets. It can be observed that flower-like BiOBr hierarchical structures again exhibited excellent photocatalytic performance compared to BiOBr nanosheets. Both BiOBr photocatalysts able to completely degrade SSY under solar irradiation. However, SSY was fully degraded by flower-like BiOBr hierarchical structures with only 60 min while BiOBr nanosheets used 90 min of irradiation.

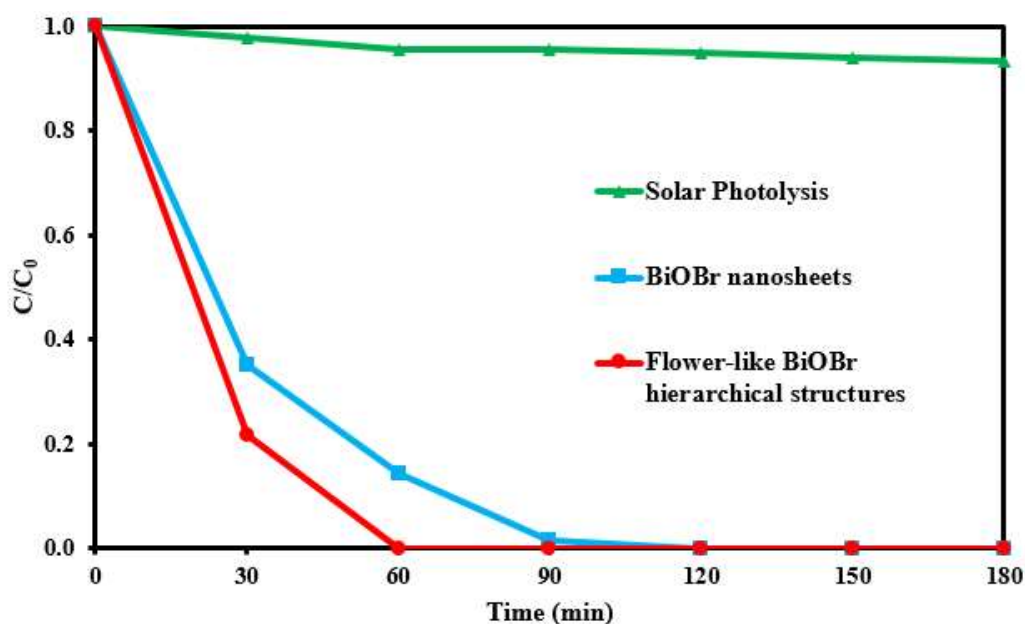


Figure 4.31 Photocatalytic degradation of SSY over flower-like BiOBr and BiOBr nanosheets under solar irradiation. Conditions: BiOBr loading=1.30 g/L, initial SSY concentrati = 10 ppm, solution pH= pH 3.0 and irradiation time= 180 min.

The superior performance by flower-like BiOBr hierarchical structures was due to the porous morphology which was formed by the interleaving of nanosheets. The hierarchical structures increased the surface to volume ratio of flower-like BiOBr which was confirmed in N<sub>2</sub> adsorption-desorption analysis (Appendix I). The large surface to volume ratio aided in accommodating more active sites and allowed penetration of solar light. Moreover, these hierarchical structures allows more efficient transportation of reactant molecules toward active sites. It was also indicated from the TA-PL test that flower-like BiOBr hierarchical structures able to produce more •OH radicals than the BiOBr nanosheets. Thus, more •OH radicals can be used to oxidize SSY leading to higher photocatalytic degradation efficiency of SSY under solar irradiation.

## CHAPTER FIVE

### CONCLUSION AND RECOMMENDATIONS

#### 5.1 CONCLUSIONS

Flower-like BiOBr hierarchical structures have been successfully synthesized via a simple hydrothermal route. The as-synthesized BiOBr samples were characterized using methods of XRD, FESEM, EDX, TEM, HRTEM, XPS, N<sub>2</sub> adsorption-desorption and UV-vis DRS for the sake of getting insights into the crystallinity, morphology, surface chemical composition, structure, specific surface area and band gap energy of the photocatalysts. Detailed structural characterization indicated that the as-synthesized BiOBr consisted a highly crystalline tetragonal structure. In addition, by employing the UV-vis DRS, the flower-like BiOBr fundamental photoabsorption edge at 430 nm while the TiO<sub>2</sub> exhibited photoabsorption below 400 nm which indicating that the light absorption of flower-like BiOBr hierarchical structures in the visible light region was excellent. Besides, the formation mechanism of the hierarchical structures through oriented aggregation was suggested and discussed in the FESEM and TEM section.

The photocatalytic activities of flower-like BiOBr hierarchical structures were also examined by degrading organic dye sunset yellow (SSY). The flower-like BiOBr hierarchical structures showed much excellent photocatalytic activity by showing 53.5% of degradation efficiency of SSY under fluorescent light irradiation while BiOBr nanosheets and TiO<sub>2</sub> showed 46.2% and 41.4% of SSY degradation

respectively. Such photocatalytic enhancement was credited to the hierarchical porous surface structure of as-synthesized BiOBr with visible light absorption ability. This can enhance the generation and separation of  $e^-$  and  $h^+$  pairs and resulted to high yield of  $\bullet\text{OH}$  radicals quantities as proven by the photoluminescence spectra.

Moreover, the performances of as-synthesized BiOBr samples were differently affected by BiOBr loading and initial SSY concentration. The photodegradation of SSY over flower-like BiOBr hierarchical structures were also tested under various pH conditions due to pH is an important operational parameter in water treatment processes. The optimum conditions of photocatalytic degradation of SSY over as-synthesized BiOBr samples were found to be 1.00 g/L of BiOBr loading, 10 ppm of initial SSY concentration and solution pH at pH 3.0 as the reaction efficiency was the highest in such conditions. The photocatalytic degradation efficiency of SSY was inhibited by inorganic anions ( $\text{SO}_4^{2-}$ ,  $\text{CO}_3^{2-}$ ,  $\text{NO}_3^-$  and  $\text{Cl}^-$ ) due to scavenger effect of various anions. In addition, the as-prepared flower like BiOBr hierarchical structures were also found to be stable and reusable after 4 times which indicated that the photocatalysts were suitable for potential practical applications.

Furthermore, photodegradation of SSY over flower-like BiOBr hierarchical structures under fluorescent light was suggested to fit the first order kinetics ( $R^2=0.9832$ ). Optimization study for SSY degradation was carried out by employing the face-centered, central composite design (CCD). It was found that maximum SSY

degradation can be achieved with 1.30 g/L BiOBr amount, 10 ppm initial SSY concentration and solution pH at pH 3.0 under 180 min of fluorescent light irradiation. Flower-like BiOBr hierarchical structures also showed an excellent performance on degradation of SSY under solar irradiation. SSY were completely degraded by as-synthesized BiOBr products with only 60 min of solar irradiation.

In a nutshell, this study demonstrated that hydrothermally synthesized flower-like BiOBr hierarchical structures were promising for applications in organic dye treatments since it can degrade pollutants in varying conditions under fluorescent and sunlight irradiation.

## 5.2 RECOMMENDATIONS

1. In this study, only pure BiOBr was examined in photocatalytic degradation SSY under fluorescent light. For future work, a variation of dopant such as transition metals to study its enhancement effect on BiOBr activity should be considered.
2. Apart from inorganic anions effect, the effect of inorganic cations such as  $Mg^{+2}$ ,  $K^+$ , and  $Na^+$  should be study in order to ensure more practical applications of flower-like BiOBr hierarchical structures.
3. There are four operating parameters were studied for their interaction in this study. In future work, more operating parameters such as effect of air flow rate, effect of light intensity and wavelength as well as effect of reaction temperature should be considered.

4. In this study, SSY was used in this study to investigate the photocatalytic activity of flower-like BiOBr hierarchical structures. In future work, real dye wastewater from industries should be used as targeted organic pollutants.
5. The research on BiOBr photocatalysis still in early phases and hence its commercialization is not foreseen in the near future. Nevertheless, while research is progressing, more convincing results can be obtained. Taking into account of commercialization, integration of the BiOBr photocatalysts with pilot scale photocatalytic generators and solar cells for large scale photocatalytic systems also seems appropriate.

## REFERENCES

- Acar, C., Dincer, I. and Zafirescu, C., 2014. A review on selected heterogeneous photocatalysts for hydrogen production. *International Journal of Energy Research*, 38 (15), pp. 1903-1920.
- Ahamd, A., 2013. *Synthesis and Evaluation of Photocatalytic Properties of BiOBr for Wastewater Treatment Applications*. M.A.Sc degree Thesis, University of Ottawa, Canada.
- Ahmad, A., Meng, X., Yun, N. and Zhang, Z., 2016. Preparation of Hierarchical BiOBr Microspheres for Visible Light-Induced Photocatalytic Detoxification and Disinfection. *Journal of Nanomaterials*, vol. 2016, Article ID 1373725, 10 pages.
- Ajmal, A. et al., 2014. Principles and mechanisms of photocatalytic dye degradation on TiO<sub>2</sub> based photocatalysts: a comparative overview. *RSC Advances*, 4, pp. 37003-37026.
- Alkaim, A. F. et al., 2014. Effect of pH on Adsorption and Photocatalytic Degradation Efficiency of Different Catalysts on Removal of Methylene Blue. *Asian Journal of Chemistry*, 26 (24), pp. 8445-8448.
- Andriantsiferana, A., Mohamed, E.F. and Delmas. H., 2013. Photocatalytic degradation of an azo-dye on TiO<sub>2</sub>/activated carbon composite material. *Environmental Technology*, 35:3, pp. 355-363.
- Antonopoulou, M., Evgenidou, E., Lambropoulou, D. and Konstantinou, I., 2013. A review on advanced oxidation processes for the removal of taste and odor compounds from aqueous media. *Water Research*, 53, pp. 215-234.

- Ao, Y. et al., 2013. Synthesis, characterization and photocatalytic activity of BiOBr-AC composite photocatalysts. *Composites: Part B*, 59, pp. 96-100.
- Ao, Y. et al., 2016. Synthesis of novel 2D-2D p-n heterojunction BiOBr/La<sub>2</sub>Ti<sub>2</sub>O<sub>7</sub> composite photocatalyst with enhanced photocatalytic performance under both UV and visible light irradiation. *Applied Catalysis B: Environmental*, 194, pp. 157-168.
- Balapure, K., Bhatt, N. and Madamwar, D., 2014. Mineralization of reactive azo dyes present in simulated textile waste water using down flow microaerophilic fixed film bioreactor. *Bioresource Technology*, 175, pp. 1-7.
- Begum, T., Gogoi, P. K. and Bora, U., 2015. Photocatalytic degradation of crystal violet dye on the surface of Au doped TiO<sub>2</sub> nanoparticles. *Indian Journal of Chemical Technology*, 24, pp. 97-101.
- Bhattacharjee, M., 2014. Evaluation of Mitodepressive Effect of Sunset Yellow Using *Allium sativum* Assay. *International Journal of Science, Environmental and Technology*, 3 (3), pp. 1120-1130.
- Bijanzad, K., Tadjarodi. A., Khiavi, M. M. and Akhavan, O., 2015. Microwave-assisted synthesis of bismuth oxybromochloride nanoflakes for visible light photodegradation of pollutants. *Physica B: Physics of Condensed Matter*, 475, pp. 14-20.
- Bilińska, L., Gmurek, M. and Ledakowicz, S., 2016. Comparison between industrial and simulated textile wastewater treatment by AOPs- Biodegradability, toxicity and cost assessment. *Chemical Engineering Journal*, 306, pp. 550-559.



- Bora, L. V. and Mewada, R. K., 2017. Visible/solar light active photocatalysts for organic effluent treatment: Fundamentals, mechanisms and parametric review. *Renewable and Sustainable Energy Reviews*, 76, pp. 1393-1421.
- Bouanimba, N. Laid, N. Zouaghi, R. and Sehili, T., 2013. Effect of pH and inorganic salts on the photocatalytic decolorization of methyl orange in the presence of TiO<sub>2</sub> P25 and PC 500. *Desalination and Water Treatment*, 53, pp. 951-963.
- Brillas, E. and Huile, C. A. M., 2014. Decontamination of wastewaters containing synthetic organic dyes by electrochemical methods. An updated review. *Applied Catalysis B: Environmental*, 166-167, pp. 603-643.
- Byrne, J. et al., 2015. A review of heterogeneous photocatalysis for water and surface disinfection. *Molecules*, 20 (4), pp. 5574-5615.
- Cao, J. et al., 2012. Chemical etching preparation of BiOI/BiOBr heterostructures with enhanced photocatalytic properties for organic dye removal. *Chemical Engineering Journal*, 185-186, pp. 91-99.
- Cao, Y., Wang, F., Jia, Z. and Liu, N., 2012. Surfactant-assisted hydrothermal synthesis of multi-layered flower-like BiOBr with enhanced visible light photocatalytic activity. *Advanced Materials Research*, 476-478, pp. 1541-1546.
- Carocho, M., Barreiro, M. F., Morales, P. and Ferreira, I. C. F.R., 2014. Adding molecules to food, pros and cons: A review on synthetic and natural food additives. *Comprehensive Reviews in Food Science and Food Safety*, 13 (4), pp. 377-399.

- Cuellar, E. L., Cruz, A. M., Torres, N. C. and Cortez, J. O., 2015. Deposition of BiOBr thin films by thermal evaporation and evaluation of its photocatalytic activity. *Catalysis Today*, 252, pp. 2-6.
- Chang, F et al., 2014. Enhanced photocatalytic performance of g-C<sub>3</sub>N<sub>4</sub> nanosheets-BiOBr hybrids. *Superlattices and Microstructures*, 76, pp. 90-104.
- Chang, X. et al., 2012. Photodegradation of Rhodamine B over unexcited semiconductor compounds of BiOCl and BiOBr. *Journal of Colloid and Interface Science*, 377, pp. 291-298.
- Chao, M and Ma, X., 2014. Convenient Electrochemical Determination of Sunset Yellow and Tartrazine in Food Samples Using a Poly(L-Phenylalanine)-Modified Glassy Carbon Electrode. *Food Analytical Methods*, 8 (1), pp. 130-138.
- Chen, J. et al., 2017. One-pot hydrothermal preparation of BiOBr/BiPO<sub>4</sub> with improved photocatalytic performance originated from remarkably enhanced separation of electron-hole pairs. *Current Applied Physics*, 17, pp. 1707-1713.
- Chen, M. et al., 2017. Enhanced Photocatalytic Degradation of Ciprofloxacin over Bi<sub>2</sub>O<sub>3</sub>/(BiO)<sub>2</sub>CO<sub>3</sub> Heterojunctions: Efficiency, Kinetics, Pathways, Mechanisms and Toxicity Evaluation. *Chemical Engineering Journal*, 334, pp. 453-461.
- Chen, Y. Wen, M. and Wu, W., 2011. Stepwise blossoming of BiOBr nanoplate-assembled microflowers and their visible-light photocatalytic activities. *CrystEngComm*, 13, pp. 3035.

- Cheng, M. et al., 2015. Hydroxyl radicals based advanced oxidation processes (AOPs) for remediation of soils contaminated with organic compounds: a review. *Chemical Engineering Journal*, 284, pp. 582-598.
- Chengalroyen, M. D. and Dabbs, E. R., 2012. The microbial degradation of azo dyes: minireview. *World Journal of Microbiology and Biotechnology*, 29 (3), pp. 389-399.
- Chládková, B. et al., 2015. Adsorption and photocatalysis of nanocrystalline TiO<sub>2</sub> particles for Reactive Red 195 removal: effect of humic acids, anions and scavengers. *Environmental Science and Pollutant Research*, 22, pp. 16514-16524.
- Choi, Y. I. et al., 2015. Recyclable magnetic CoFe<sub>2</sub>O<sub>4</sub>/BiOX (X= Cl, Br and I) microflowers for photocatalytic water treatments contaminated with methyl orange, rhodamine B, methylene blue and a mixed dyes. *RSC Advances*, 5(97), pp. 79624-79634.
- Chung, K. T., 2016. Azo Dyes and Human Health: A Review. *Journal of Environmental Science and Health, Part C*, 34 (4), pp. 233-261.
- Cui, H. et al., 2017. Synthesis of CdS/BiOBr nanosheets composites with efficient visible-light photocatalytic activity. *Journal of Physics and Chemistry of Solids*, 112, pp. 80-87.
- Cui, W., An, W., Hu, J. and Liang, Y., 2014. Novel Cu<sub>2</sub>O quantum dots coupled flower-like BiOBr for enhanced photocatalytic degradation of organic contaminant. *Journal of Hazardous Materials*. 280, pp. 417-427.

- Cui, W. et al., 2014. Synthesis of CdS/BiOBr composites and its enhanced photocatalytic degradation for Rhodamine B. *Applied Surface Science*, 319, pp. 298-305.
- Cui, W. et al., 2014. A novel nano-sized BiOBr decorated  $K_2La_2Ti_3O_{10}$  with enhanced photocatalytic properties under visible light. *Journal of Solid State Chemistry*, 215, pp. 94-101.
- Cui, Y. et al., 2013. Photocatalytic activities of  $Bi_2S_3$ /BiOBr nanocomposites synthesized by a facile hydrothermal process. *Applied Surface Science*, 290, pp. 233-239.
- Dai, K. et al., 2014. A scalable synthesis technique of hierarchical BiOBr microspheres for advanced visible light photocatalyst. *Materials Letters*, 136, pp. 438-440.
- Dash, A. et al., 2014. Microwave Synthesis, Photoluminescence, and Photocatalytic Activity of PVA-Functionalized  $Eu^{3+}$ -Doped BiOX (X= Cl, Br, I) Nanoflakes. *Langmuir*, 30, pp. 1401-1409.
- Deng, C. and Guan, H., 2013. Fabrication of hollow inorganic fullerene-like BiOBr eggshells with highly efficient visible light photocatalytic activity. *Materials Letters*, 107, pp. 119-122.
- Deng, Y. and Zhao, R., 2015. Advanced Oxidation Processes (AOPs) in Wastewater Treatment. *Current Pollution Reports*, 1 (3), pp. 167-176.
- Dugandžić, A. M. et al., 2016. Effect of inorganic ions, photosensitisers and scavengers on the photocatalytic degradation of nicosulfuron. *Journal of Photochemistry and Photobiology A: Chemistry*, 336, pp. 146-155.

- Duo, F. et al., 2015. One-pot hydrothermal synthesis of a novel BiPO<sub>4</sub>/BiOBr composite with enhanced visible light photocatalytic activities. *Materials Science in Semiconductor Processing*, 38, pp. 157-164.
- Dwivedi, K. and Kumar, G., 2015. Genetic Damage Induced by a Food Coloring Dye (Sunset Yellow) on Meristematic Cells of Brassica campestris L. *Journal of Environmental and Public Health*, 2015.
- Eskandarloo, H., Badieli, A. and Behnajady, M. A., 2014. Study of the Effect of Additives on the Photocatalytic Degradation of a Triphenylmethane Dye in the Presence of Immobilized TiO<sub>2</sub>/NiO Nanoparticles: Artificial Neural Network Modelling. *Industrial & Engineering Chemistry Research*, 53, pp. 6881-6895.
- Fang, Y. et al., 2016. Mannitol ligand-assisted assembly of BiOBr photocatalyst in the cationic micelles of cetylpyridinium bromide. *Catalysis Communications*, 80, pp. 15-19.
- Fathinia, M. and Khataee, A. R., 2013. Residence time distribution analysis and optimization of photocatalysis of phenazopyridine using immobilized TiO<sub>2</sub> nanoparticles in a rectangular photoreactor. *Journal of Industrial and Engineering Chemistry*, 19, pp. 1525-1534.
- Feilizadeh, M. et al., 2015. Optimization of operating parameters for efficient photocatalytic inactivation of Escherichia coli based on a statistical design of experiments. *Water Science and Technology*, 71, pp. 823-831.
- Felix, A., Andrew, A. and Mededode, A., 2014. Heterogeneous Photocatalytic Degradation of Naphthalene using Periwinkle Shell Ash: Effect of Operating

- Variables, Kinetic and Isotherm Study. *South African Journal of Chemical Engineering*, 19, pp. 31-45.
- Feng, H. et al., 2015. Modulation of Photocatalytic Properties by Strain in 2D BiOBr Nanosheets. *ACS Applied Materials & Interfaces*, 7 (50), pp. 27592-27596.
- Ganose, A. M. et al., 2016. Interplay of Orbital and Relativistic Effects in Bismuth Oxyhalides: BiOF, BiOCl, BiOBr, and BiOI. *Chemistry of Materials*, 28 (7), pp. 1980-1984.
- Gao, J. et al., 2017. Hydrothermal synthesis of BiOBr/FeWO<sub>4</sub> composite photocatalysts and their photocatalytic degradation of doxycycline. *Journal of Alloys and Compounds*, 732, pp. 43-51.
- Gao, M. et al., 2016. Surface decoration of BiOBr with BiPO<sub>4</sub> nanoparticles to build heterostructure photocatalysts with enhanced visible-light photocatalytic activity. *Separation and Purification Technology*, 170, pp. 193-189.
- Gao, S. et al., 2017. Photocatalytic removal of tetrabromobisphenol A by magnetically separable flower-like BiOBr/BiOI/Fe<sub>3</sub>O<sub>4</sub> hybrid nanocomposites under visible-light irradiation. *Journal of Hazardous Materials*, 331, pp. 1-12.
- Gao, X. et al., 2015. Photocatalytic degradation of carbamazepine using hierarchical BiOCl microspheres: Some key operating parameters, degradation intermediates and reaction pathway. *Chemical Engineering Journal*, 273, pp. 156-165.

- Gaya, U. I., 2013. Kinetic Concepts of Heterogeneous Photocatalysis. *Heterogeneous Photocatalysis Using Inorganic Semiconductor Solids*, pp. 43-71.
- Georgaki, I., Vasilaki, E. and Katsarakis, N., 2014. A Study on the Degradation of Carbamazepine and Ibuprofen by TiO<sub>2</sub> & ZnO Photocatalysis upon UV/Visible-Light Irradiation. *American Journal of Analytical Chemistry*, 5, pp. 518-534.
- Giannakis, S., Rtimi, S. and Pulgarin, C., 2017. Light-Assisted Advanced Oxidation Processes for the Elimination of Chemical and Microbiological Pollution of Wastewaters in Developed and Developing Countries. *Chemical Engineering Journal*, 284, pp. 582-598.
- Gondal, M. et al., 2011. Adsorption and degradation performance of Rhodamine B over BiOBr under monochromatic 532nm pulsed laser exposure. *Applied Catalysis A: General*, 397 (1-2), pp. 192-200.
- Gomes, K. M. S. et al., 2013. Citotoxicity of food dyes Sunset Yellow (E-110), Bordeaux Red (E-123) and Tartrazine Yellow (E-102) on *Allium cepa* L. root meristematic cells. *Food Science and Technology*, 33 (1), pp. 218-223.
- Guo, C. et al., 2014. Novel magnetically recoverable BiOBr/iron oxides heterojunction with enhanced visible light-driven photocatalytic activity. *Applied Surface Science*, 320, pp. 383-390.
- Guo, W. et al., 2016. Morphology-controlled preparation and plasmon-enhanced photocatalytic activity of Pt–BiOBr heterostructures. *Journal of Hazardous Materials*, 308, pp. 374-385.

- Guo, W., Yang, Z., Zhou, X. J. and Wu, Q., 2015. Degradation and mineralization of dyes with advanced oxidation processes (AOPs): A brief review. *International Forum on Energy, Environment Science and Materials*, pp. 341-344.
- Gupta, G., Kaur, A., Sinha, S. A. S. K. and Kansal, K., 2017. Photocatalytic degradation of levofloxacin in aqueous phase using Ag/AgBr/BiOBr microplates under visible light. *Materials Research Bulletin*, 88, pp. 148-155.
- Haddeland, I. et al., 2013. Global water resources affected by human interventions and climate change. *Proceedings of the National Academy of Sciences*, 111 (9), pp. 3251-3256.
- Hamad, H. A. et al., 2016. Photocatalytic parameters and kinetic study for degradation of dichlorophenol-indophenol (DCPIP) dye using highly active mesoporous TiO<sub>2</sub> nanoparticles. *Journal of Environmental Sciences (China)*, 43, pp. 26-39.
- Han, A. et al., 2017. Efficient photodegradation of chlorophenols by BiOBr/NaBiO<sub>3</sub> heterojunctioned composites under visible light. *Journal of Hazardous Materials*, 341, pp. 83-92.
- Han, Q. et al., 2016. Effect of the counter ions on composition and morphology of bismuth oxyhalides and their photocatalytic performance. *Chemical Engineering Journal*, 299, pp. 217-226.
- Harp, B. P. and Barrows, J. N., 2015. US regulation of colour additives in foods. *Colour Additives for Foods and Beverage*, pp. 75-88.



- Hassaan, M. A., Nemr, A. E. and Madkour, F. F., 2016. Advanced oxidation processes of Mordant Violet 40 dye in freshwater and seawater. *Egyptian Journal of Aquatic Research*, 43 (1), pp. 1-9.
- He, M. et al., 2015. Significant improvement of photocatalytic activity of porous graphitic-carbon nitride/bismuth oxybromide microspheres synthesized in an ionic liquid by microwave- assisted processing. *Materials Science in Semiconductor Processing*, 32, pp. 117-124.
- He, M. et al., 2013. Reactable ionic liquid-assisted solvothermal synthesis of flower-like bismuth oxybromide microspheres with highly visible-light photocatalytic performances. *Micro & Nano Letters*, 8 (8), pp. 450-454.
- He, Q., Ni, Y. and Ye, S., 2017. Preparation of flowerlike BiOBr/Bi<sub>2</sub>MoO<sub>6</sub> composite superstructures and the adsorption behaviour to dyes. *Journal of Physics and Chemistry of Solids*, 104, pp. 286-292.
- Hou, R. et al., 2017. Coupling System of Ag/BiOBr Photocatalysis and Direct Contact Membrane Distillation for Complete Purification of N-Containing Dye Wastewater. *Chemical Engineering Journal*, 317, pp. 386-393.
- Hu, Y., Li, R. Fan, C. and Mao, X., 2015. One-step synthesis of porous BiOBr film and Bi nanopowder simultaneously from Bi plate via electrochemical method. *Materials Letters*, 161, pp. 41-44.
- Hu, J. et al., 2016. BiOBr nanodots decorated hierarchical Bi<sub>2</sub>WO<sub>6</sub> fabricating p-n heterostructure with enhanced photo-induced electric performance and photocatalytic degradation. *RSC Advances*, 6, pp. 29554-29562.

- Huo, Y., Zhang, J., Miao, M. and Jin, Y., 2011. Solvothermal synthesis of flower-like BiOBr microspheres with highly visible-light photocatalytic performances. *Applied Catalysis B: Environmental*, 111-112, pp. 334-341.
- Ibhadon, A. O. and Fitzpatrick, P., 2013. Heterogeneous Photocatalysis: Recent Advances and Applications. *Catalysts*, 3 (1), pp. 189-218.
- Iqbal, M. and Bhatti, I. A., 2013. Application of biological oxidation and solar driven advanced oxidation processes to remediation of winery wastewater. *Catalysis Today*, 209, pp. 201-208.
- Jain, A. and Mathur, P., 2015. Estimation of Food Additive Intake—Overview of the Methodology. *Journal of Food Reviews International*, 31 (4), pp. 355-384.
- Janani, S. et al., 2016. Photodegradation of methylene blue using magnetically reduced graphene oxide bismuth oxybromide composite. *Journal of Environmental Chemical Engineering*, 4 (1), pp. 534-541.
- Jiang, G. et al., 2014. Growth of N-doped BiOBr nanosheets on carbon fibers for photocatalytic degradation of organic pollutants under visible light irradiation. *Power Technology*, 260, pp. 84-89.
- Jiang, G. et al., 2014. Immobilization of N, S-codoped BiOBr on glass fibers for photocatalytic degradation of rhodamine B. *Power Technology*, 261, pp. 170-175.
- Jiang, G. et al., 2013. Photocatalytic properties of hierarchical structures based on Fe-doped BiOBr hollow microspheres. *Journal of Materials Chemistry A*, 1 (7), pp. 2406.

- Jiang, R. et al., 2016. Fabrication of novel magnetically separable BiOBr/CoFe<sub>2</sub>O<sub>4</sub> microspheres and its application in the efficient removal of dye from aqueous phase by an environment-friendly and economical approach. *Applied Surface Science*, 364, pp. 604-612.
- Jiang, T. et al., 2016. BiOBr/BiOF composites for efficient degradation of rhodamine B and nitro- benzene under visible light irradiation. *Journal of Colloid and Interface Science*, 490, pp. 812-818.
- Jiang, Z. et al., 2010. The hydrothermal synthesis of BiOBr flakes for visible-light-responsive photocatalytic degradation of methyl orange. *Journal of Photochemistry and Photobiology A: Chemistry*, 212 (1), pp. 8-13.
- Julkapli, N. M., Bagheri, S. and Hamid, S. B. A., 2014. Recent Advances in Heterogeneous Photocatalytic Decolorization of Synthetic Dyes. *The Scientific World Journal*, 2014.
- Kanagaraj, T. and Thiripuranthagan, S., 2017. Photocatalytic activities of novel SrTiO<sub>3</sub>-BiOBr heterojunction catalysts towards the degradation of reactive dyes. *Applied Catalysis B: Environmental*, 207, pp. 218-232.
- Kanagaraj, T., Thiripuranthagan, S., Paskalis, S. M. K. and Hideki, A., 2017. Visible light photocatalytic activities of template free porous graphitic carbon nitride-BiOBr composite catalysts towards the mineralization of reactive dyes. *Applied Surface Science*, 426, pp. 1030-1045.
- Karimi, R. et al., 2016. Efficient adsorption of erythrosine and sunset yellow onto modified palladium nanoparticles with a 2-diamine compound: Application of

- multivariate technique. *Journal of Industrial and Engineering Chemistry*, 48, pp. 43-55.
- Keihan, A. M. et al., 2017. Pd nanoparticle loaded TiO<sub>2</sub> semiconductor for photocatalytic degradation of Paraoxon pesticide under visible-light irradiation. *Journal of Materials Science: Materials in Electronics*, 28, pp. 16718-16727.
- Khamparia, S. and Jaspal, D., 2017. Study of decolorisation of binary dye mixture by response surface methodology. *Journal of Environmental Management*, 201, pp. 316-326.
- Khataee, A. et al., 2013. Synthesis and Characterization of Dysprosium-Doped ZnO Nanoparticles for Photocatalysis of a Textile Dye under Visible Light Irradiation. *Industrial & Engineering Chemistry Research*, 53 (5), pp. 1924-1932.
- Khataee, A. R., Kasiri, M. B. and Alidokht, L., 2011. Application of response surface methodology in the optimization of photocatalytic removal of environmental pollutants using nanocatalysts A. *Environmental Technology*, 32, pp. 37-41.
- Krzemińska, D., Neczaj, E. and Borowski, G., 2015. Advanced Oxidation Processes for Food Industrial Wastewater Decontamination. *Journal of Ecological Engineering*, 16 (2), pp. 61-71.
- Kumar, R., Kumar, G. and Umar, A., 2013. ZnO nano-mushrooms for photocatalytic degradation of methyl orange. *Materials Letters*, 97, pp. 100-103.

- Kumar, R., Kumar, G. and Umar, A., 2014. Zinc Oxide Nanomaterials for Photocatalytic Degradation of Methyl Orange: A Review. *Nanoscience and Nanotechnology Letters*, 6, pp. 631-650.
- Lam, S. M., Sin, J. C., Abdullah, A. Z. and Mohamed, A. R., 2012. Degradation of wastewaters containing organic dyes photocatalysed by zinc oxide: a review. *Journal of Desalination and Water Treatment*, 41 (1-3), pp. 131-169.
- Lee, J. S. and Jang, J., 2014. Hetero-structured semiconductor nanomaterials for photocatalytic applications. *Journal of Industrial and Engineering Chemistry*, 20 (2), pp. 363-371.
- Li, H. et al., 2014. Enhanced visible light photocatalytic activity of bismuth oxybromide lamellas with decreasing lamella thicknesses. *Journal of Materials Chemistry A*, 2 (23), pp. 8926-8932.
- Li, H. et al., 2016. Synthesis of belt-like BiOBr hierarchical nanostructure with high photocatalytic performance. *Materials Research Bulletin*, 77, pp. 171-177.
- Li, J. et al., 2016. The role of adsorption in photocatalytic degradation of ibuprofen under visible light irradiation by BiOBr microspheres. *Chemical Engineering Journal*, 297, 139-147.
- Li, J., Yu, Y. and Zhang, L., 2014. Bismuth oxyhalide nanomaterials: layered structures meet photocatalysis. *Nanoscale*, 6, pp. 8473-8488.
- Li, K. et al., 2014. Photocatalytic degradation and electricity generation in a rotating disk photoelectrochemical cell over hierarchical structured BiOBr film. *Applied Catalysis B: Environmental*, 164, pp. 82-91.

- Li, R. et al., 2014. Preparation of BiOBr thin films with micro-nano-structure and their photocatalytic applications. *Thin Solid Films*, 562, pp. 506-512.
- Li, R. et al., 2015. A facile approach for the tunable fabrication of BiOBr photocatalysts with high activity and stability. *Applied Surface Science*, 355, pp. 1075-1082.
- Li, R. et al., 2017. Synthesis of BiOBr microspheres with ethanol as self-temple and solvent with controllable morphology and photocatalytic activity. *Catalysis Communications*, 106, pp. 1-5.
- Li, T., Wang, H., Zhu, Y. and Bian, Z., 2014. Optimum Conditions of Ag/BiVO<sub>4</sub> Photocatalytic Performance on Degradation of Paracetamol by Response Surface Methodology. *Advanced Materials Research*, 1073-1076, pp. 336-339.
- Li, W. et al., 2015. Hollow Mesoporous SiO<sub>2</sub>-BiOBr Nanophotocatalyst: Synthesis, Characterization and Application in Photodegradation of Organic Dyes under Visible-Light Irradiation. *ACS Sustainable Chemistry & Engineering*, 3, pp. 1101-1110.
- Li, X. et al., 2013. One-pot solvothermal preparation of S-doped BiOBr microspheres for efficient visible-light induced photocatalysis. *MRS Communications*, 3 (4), pp. 219-224.
- Li, X., Li, W., Zhang, L. and Zhuo, S., 2017. A facile route to the synthesis of magnetically separable BiOBr/NiFe<sub>2</sub>O<sub>4</sub> composites with enhanced photocatalytic performance. *Applied Surface Science*, 419, pp. 586-594.

- Li, Y. et al., 2015. Synthesis of BiOBr-PVP hybrids with enhanced adsorption-photocatalytic properties. *Applied Surface Science*, 347, pp. 258-264.
- Li, Y. et al., 2013. Titanium alkoxide induced BiOBr–Bi<sub>2</sub>WO<sub>6</sub> mesoporous nanosheet composites with much enhanced photocatalytic activity. *Journals of Materials Chemistry A*, 1 (27), pp. 7949-7956.
- Lin, H. et al., 2014. Facile anion-exchange synthesis of BiOI/BiOBr composite with enhanced photoelectrochemical and photocatalytic properties. *Ceramics International*, 40, pp. 9743-9750.
- Lin, H. P. et al., 2016. Controlled hydrothermal synthesis of PbBiO<sub>2</sub>Br/BiOBr heterojunction with enhanced visible-driven-light photocatalytic activities. *Journal of Molecular Catalysis A: Chemical*, 417, pp. 268-183.
- Lin, Y. T., Weng, C. H. and Chen, F. Y., 2014. Key operating parameters affecting photocatalytic activity of visible-light-induced C-doped TiO<sub>2</sub> catalyst for ethylene oxidation. *Chemical Engineering Journal*, 248, pp. 175-183.
- Liu, J. et al., 2017. Novel multi-heterostructured Pt-BiOBr/TiO<sub>2</sub> nanotube arrays with remarkable visible-light photocatalytic performance and stability. *Optoelectronics Letters*, 13 (3), pp. 165-171.
- Liu, Y. and Wu, Q., 2017. One novel material with high visible-light activity: hexagonal Cu flakelets embedded in the petals of BiOBr flower-nanospheres. *Journal of Nanoparticles Research*, 19 (2), pp. 1-14.

- Liu, Z. S. et al., 2013. Cadmium sulphide quantum dots sensitized hierarchical bismuth oxybromide microsphere with highly efficient photocatalytic activity. *Journal of Colloid and Interface Science*, 392 (1), pp. 337-342.
- Liu, Z. S. and Wu, B. T., 2015. One pot synthesis of bismuth–bismuth oxybromide composites with enhanced visible-light photocatalytic activity. *Materials Science in Semiconductor Processing*, 31, pp. 68-75.
- Liu, Z. S. et al., 2014. Solvothermal synthesis of BiOBr thin film and its photocatalytic performance. *Applied Surface Science*, 288, pp. 369-372.
- Liu, Z. S., Wu, B. T., Xiang, D. H. and Zhu, Y. B., 2012. Effect of solvents on morphology and photocatalytic activity of BiOBr synthesized by solvothermal method. *Materials Research Bulletin*, 47 (11), pp. 3753-3757.
- Liu, Z. S. et al., 2012. Fe-Ions Modified BiOBr Mesoporous Microspheres with Excellent Photocatalytic Property. *Catalysis Letters*, 142 (12), pp. 1489-1497.
- Lv, J. et al., 2017. Facile constructing novel 2D porous g-C<sub>3</sub>N<sub>4</sub>/BiOBr hybrid with enhanced visible-light-driven photocatalytic activity. *Separation and Purification Technology*, 178, pp. 6-17.
- Ma, J., Liu, S. and Qi, G., 2017. Synthesis of m-LaVO<sub>4</sub>/BiOBr composite photocatalysts and their photocatalytic performance under visible light. *Materials Research Bulletin*, 95, pp. 146-151.
- Mahfouz, M. E. and Moussa, E. A., 2015. The Impact of Curcumin Administration on The Food Colouring Sunset Yellow-Induced Damage in Testes and Liver of Male Rat: Gene Expression and Ultrastructural Studies. *The Egyptian Journal of Experimental Biology (Zoology)*, 11 (1), pp. 43-60.



- Mahmoodi, N. M., Keshavarzi, S. and Ghezelbash, M., 2017. Synthesis of nanoparticle and modelling of its photocatalytic dye degradation ability from colored wastewater. *Journal of Environmental Chemical Engineering*, 5 (4), pp. 3684-3689.
- Malayeri, H. Z. and Ganjidoust, A. H., 2014. Photocatalytic Phenol Degradation by Immobilized Nano ZnO: Intermediates & Key Operating Parameters. *Water Environmental Research*, 86 (9), pp. 771-778.
- Meng, X. et al., 2017. Enhanced visible light-induced photocatalytic activity of surface-modified BiOBr with Pd nanoparticles. *Applied Surface Science*, 433, pp. 76-87.
- Meng, X. and Zhang, Z., 2015. Facile synthesis of BiOBr/Bi<sub>2</sub>WO<sub>6</sub> heterojunction semiconductors with high visible-light-driven photocatalytic activity. *Journal of Photochemistry and Photobiology A: Chemistry*, 310, pp. 33-44.
- Mera, A. C., Váldez, H., Jamett, F. J. and Meléndrez, M. F., 2017. BiOBr microspheres for photocatalytic degradation of an anionic dye. *Solid State Sciences*, 65, pp. 15-21.
- Miao, J. et al., 2013. Heterogeneous photocatalytic degradation of mordant black 11 with ZnO nanoparticles under UV–Vis light. *Journal of the Taiwan Institute of Chemical Engineers*, 45 (4), pp. 1636-1641.
- Naddeo, A. V., 2013. Wastewater Treatment by Combination of Advanced Oxidation Processes and Conventional Biological Systems. *Journal of Bioremediation & Biodegradation*, 04 (08).

- Nakata, K. and Fujishima, A., 2012. TiO<sub>2</sub> photocatalysis: Design and applications. *Journal of Photochemistry and Photobiology C: Photochemistry Reviews*, 13, pp. 169-189.
- Natarajan, K., Bajaj, H. C. and Tayade, R. J., 2015. Photocatalytic efficiency of Bismuth Oxyhalide (Cl, Br, I) nanoplates for RhB dye degradation under LED irradiation. *Journal of Industrial and Engineering Chemistry*, 34, pp. 146-156.
- Nethaji, S., Tamilarasaan, G., Neehar, P. and Sivasamy, A., 2017. Visible light photocatalytic activities of BiOBr-activated carbon (derived from waste polyurethane) composites by hydrothermal process. *Journal of Environmental Chemical Engineering*.
- Niu, P. and Hao, J., 2013. Efficient degradation of organic dyes by titanium dioxide–silicotungstic acid nanocomposite films: Influence of inorganic salts and surfactants. *Colloids and Surfaces A: Physicochemical and Engineering Aspects*, 443, pp. 501-507.
- Pandir, D., 2014. DNA damage in human germ cell exposed to the some food additives in vitro. *Cytotechnology*, 68 (4), pp. 725-733.
- Patil, S. P. et al., 2016. Facile sonochemical synthesis of BiOBr-graphene oxide nanocomposite with enhanced photocatalytic activity for the degradation of Direct green. *Materials Science in Semiconductor Processing*, 52, pp. 55-61.
- Peng, Y., Xu, J., Liu, T. and Mao, Y., 2017. Controlled synthesis of one-dimensional BiOBr with exposed (110) facet and enhanced photocatalytic activities. *CrsytEngComm*, 19, pp. 6473-6480.

- Peng, Y. Z. et al., 2016. Comparing the Degradation of Acetochlor to RhB using BiOBr under Visible Light: A Significantly Different Rate-Catalyst Dose Relationship. *Applied Catalysis B: Environmental*, 181, pp. 517-523.
- Pešoutová, R., Hlavínek, P. and Matysíková, J., 2011. Use of Advanced Oxidation Processes for Textile Wastewater Treatment—A Review. *Food and Environmental Safety Journal*, 10 (3), pp. 59-65.
- Popli, S., and Patel, U. D., 2014. Destruction of azo dyes by anaerobic–aerobic sequential biological treatment: a review. *International Journal of Environmental Science and Technology*, 12 (1), pp. 405-420.
- Qin, X. et al., 2013. Three dimensional BiOX (X¼Cl, Br and I) hierarchical architectures: facile ionic liquid-assisted solvothermal synthesis and photocatalysis towards organic dye degradation. *Materials Letters*, 100, pp. 285-288.
- Rajamanickam, D. and Shanthi, M., 2014. Photocatalytic degradation of an azo dye Sunset Yellow under UV-A light using TiO<sub>2</sub>/CAC composite catalysts. *Spectrochimica Acta Part A: Molecular and Biomolecular Spectroscopy*, 128, pp. 100-108.
- Rajamanickam, D. and Shanthi, M., 2014. Photocatalytic mineralization of a water pollutant, Sunset Yellow dye by an advanced oxidation process using a modified catalyst. *Toxicological and Environmental Chemistry*, 95 (9), pp. 1484-1498.

- Ren, M., Song, J., Shi, Y., Xiang, Y. and Hu, G., 2014. Synthesis of zinc pyrovanadate 3D flower-like microspheres and their photocatalytic properties. *Journal of Crystal Growth*, 402, pp. 119-123.
- Reza, K. M., Kurny, A. S. W. and Gulshan, F., 2015. Parameters affecting the photocatalytic degradation of dyes using TiO<sub>2</sub>: a review. *Applied Water Science*, 7 (4), pp. 1569-1578.
- Ribeiro, A. R., Nunes, O. C., Pereira, M. F. R. and Silva, A. M. T., 2014. An overview on the advanced oxidation processes applied for the treatment of water pollutants defined in the recently launched Directive 2013/39/EU. *Environment International*, 75, pp. 33-51.
- Roosta, M., Ghaedi, M., Sahraei, R. and Purkait, M. K., 2015. Ultrasonic assisted removal of sunset yellow from aqueous solution by zinc hydroxide nanoparticle loaded activated carbon: Optimized experimental design. *Material Science and Engineering C*, 52, pp. 82-89.
- Rovina, K., Prabakaran, P. P., Siddiquee, S. and Shaarani, S. M., 2016. Methods for the Analysis of Sunset Yellow FCF (E110) in Food and Beverage Products- A review. *Trend in Analytical Chemistry*, 85, pp. 47-56.
- Saadati, F., Keramati, N. and Ghazi, M. M., 2016. Influence of parameters on the photocatalytic degradation of tetracycline in wastewater: A review. *Journal of Critical Reviews in Environmental Science and Technology*, 46 (8), pp. 757-782.

- Saravanan, R., Gracia, F. and Stephen, A., 2017. Nanocomposites for Visible Light-induced Photocatalysis. *Nanocomposites for Visible Light-induced Photocatalysis*, pp. 19-40.
- Sarkar, S., Banerje, A., Halder, U., Biswas, R. and Bandopadhyay, R., 2017. Degradation of Synthetic Azo Dyes of Textile Industry: a Sustainable Approach Using Microbial Enzymes. *Water Conservation Science and Engineering*, 2, pp. 121-131.
- Sayed, H. M. et al., 2012. The modifying effect of selenium and vitamins A, C, and E on the genotoxicity induced by sunset yellow in male mice. *Mutation Research*, 744 (2), pp. 145-153.
- Shang, M., Wang, W. and Zhang, L., 2009. Preparation of BiOBr lamellar structure with high photocatalytic activity by CTAB as Br source and template. *Journal of Hazardous Materials*, 167, pp. 803-809.
- Shi, H., Gondal, M. A., Al-Saadi, A. A. and Chang, X., 2015. Visible-light-induced Photodegradation Enhancement of Methyl Orange over Bismuth Oxybromide Through a Semiconductor Mediated Process. *Journal of Advanced Oxidation Technologies*, 18 (1), pp. 78-84.
- Shi, X. et al., 2013. PVP assisted hydrothermal synthesis of BiOBr hierarchical nanostructures and high photocatalytic capacity. *Chemical Engineering Journal*, 222, pp. 120-127.
- Sin, J. C., Lam, S. M., Lee, K. T. and Mohamed, A. R., 2013. Preparation of rare earth-doped ZnO hierarchical micro/nanospheres and their enhanced

- photocatalytic activity under visible light irradiation. *Ceramics International*, 40, pp. 5431-5440.
- Singh, C. and Chaudhary, R., 2015. Response Surface Methodology Used for Characterization and Optimization of Photocatalytic and Oxidant for the Treatment of Municipal Wastewater. *Environmental Progress & Sustainable Energy*, 34 (6), pp. 1629-1639.
- Singh, R. L., Singh, P. K. and Sing, R. P., 2015. Enzymatic decolorization and degradation of azo dyes –A review. *International Biodeterioration & Biodegradation*, 104, pp. 21-31.
- Sivakumar, A., Murugesan, B., Loganathan, A. and Sivakumar, P., 2014. A review on decolourisation of dyes by photodegradation using various bismuth catalysts. *Journal of the Taiwan Institute of Chemical Engineers*, 45, pp. 2300-2306.
- Sohrabi, M. R., Khavaran, A., Shariati, S. and Shariati, S., 2014. Removal of Carmoisine edible dye by Fenton and photo Fenton processes using Taguchi orthogonal array design. *Arabian Journal of Chemistry*, 10, pp. 3523-3531.
- Song, S. et al., 2012. Microwave-assisted synthesis of BiOBr/graphene nanocomposites and their enhanced photocatalytic activity. *Dalton Transactions*, 41 (34), pp. 10472-10476.
- Souza, S. B. et al., 2013. Application of biological oxidation and solar driven advanced oxidation processes to remediation of winery wastewater. *Catalysis Today*, 209, pp. 201-208.

- Tassalit, D. et al., 2016. Effect and interaction study of acetamiprid photodegradation using experimental design. *Water Science and Technology*, 74 (8), pp. 1953-1963.
- Tavakoli, F. et al., 2017. Optimization of Influential Factors on the Photocatalytic Performance of TiO<sub>2</sub>–Graphene Composite in Degradation of an Organic Dye by RSM Methodology. *Journal of Cluster Science*, 28 (5), pp. 2979-2995.
- Tripathi, G. K. and Kurchania, R., 2017. Photocatalytic behaviour of BiOX (X = Cl/Br, Cl/I and Br/I) composites/heterogeneous nanostructures with organic dye. *Optical and Quantum Electronics*, 49 (6), pp. 1-17.
- Tong, Z. et al., 2015. Three-Dimensional Porous Aerogel Constructed by g-C<sub>3</sub>N<sub>4</sub> and Graphene Oxide Nanosheets with Excellent Visible-Light Photocatalytic Performance. *ACS Applied Materials & Interfaces*, 7 (46), pp. 25693-25701.
- Tu, X., Luo, S., Chen, G. and Li, J., 2012. One-Pot Synthesis, Characterization, and Enhanced Photocatalytic Activity of a BiOBr–Graphene Composite. *Chemistry- A European Journal*, 18 (45), pp. 14359-14366.
- Vaez, M. Moghaddam, A. Z. and Alijani, S., 2012. Optimization and Modeling of Photocatalytic Degradation of Azo Dye Using a Response Surface Methodology (RSM) Based on the Central Composite Design with Immobilized Titania Nanoparticles. *Industrial & Engineering Chemistry Research*, 51 (11), pp. 4199-4207.
- Vasques, É. C. et al., 2014. Modelling studies by adsorption for the removal of sunset yellow azo dye present in effluent from a soft drink plant. *Environmental Technology*, 35 (12), pp. 1532-1540.

- Vörösmarty, C. J. et al., 2010. Global threats to human water security and river biodiversity. *Nature*, 467 (7315), pp. 555-561.
- Wang, D., Hou, P., Yang, P. and Cheng, X., 2017. BiOBr@SiO<sub>2</sub> flower-like nanospheres chemically-bonded on cement-based materials for photocatalysis. *Applied Surface Science*, 430, pp. 539-548.
- Wang, L. L. et al., 2012. The Contrastive Research in the Photocatalytic Activity of BiOBr Synthesized by Different Reactants. *Journal of Nanomaterials*, 2012.
- Wang, M. et al., 2016. Fe<sub>3</sub>O<sub>4</sub>@β-CD nanocomposite as heterogeneous Fenton-like catalyst for enhanced degradation of 4-chlorophenol (4-CP). *Applied Catalysis B: Environmental*, 188 (5), pp. 113-122.
- Wang, Q. et al., 2015. Immobilized Heteropolyacids with zeolite (MCM-41) to enhance photocatalytic performance of BiOBr. *Materials Letters*, 161, pp. 267-270.
- Wang, Q. et al., 2015. Preparation of efficient visible-light-driven BiOBr/Bi<sub>2</sub>O<sub>3</sub> heterojunction composite with enhanced photocatalytic activities. *Journal of Alloys and Compounds*, 649, pp. 474-482.
- Wang, X. J., Xu, X. N., Han, Y. J. and Chen, X. N., 2015. Highly efficient photocatalytic degradation of methyl orange and Rhodamine B by hierarchical BiOBr microspheres. *Crystal Research and Technology*, 50 (5), pp. 405-412.
- Wang, X. et al., 2015. Construction of amorphous TiO<sub>2</sub>/BiOBr heterojunctions via facets coupling for enhanced photocatalytic activity. *Journal of Hazardous Materials*, 292, pp. 126-136.



- Wang, X. Yang, J., Chen, Y., Zhang, Y. and Tang, Y., 2013. EDTA-modified hydrothermal synthesis of a novel four-leaf clover-shape BiOBr microstructure. *Materials Letters*, 116, pp. 171-174.
- Wang, Y. et al., 2012. Synthesis, characterization, and photocatalytic properties of BiOBr catalyst. *Journal of Solid State Chemistry*, 199, pp. 224-229.
- Wang, Y., Sunarso, J., Zhao, B., Ge, C. and Chen, G., 2017. One-dimensional BiOBr nanosheets/TiO<sub>2</sub> nanofibers composite: Controllable synthesis and enhanced visible photocatalytic activity. *Ceramic International*, 43 (17).
- Wawrzkiwicz, M., 2011. Sorption of Sunset Yellow dye by weak base anion exchanger – kinetic and equilibrium studies. *Environmental Technology*, 32 (4), pp. 455-465.
- Wei, Z. D. and Wang, R., 2016. Hierarchical BiOBr microspheres with oxygen vacancies synthesized via reactable ionic liquids for dyes removal. *Chinese Chemical Letters*, 27 (5), pp. 769-772.
- Wu, D. et al., 2016. Alkali-Induced in Situ Fabrication of BiO-Decorated BiOBr Nanosheets With Excellent Photocatalytic Performance. *Journal of Physical Chemistry C*, 120 (14), pp. 7715-7727.
- Wu, S. et al., 2015. Microwave-Solvothermal Synthesis of Nanostructured BiOBr with Excellent Visible-Light Photocatalytic Properties. *Journal of Nanomaterials*, 2015.
- Xia, J. et al., 2011. Improved visible light photocatalytic activity of sphere-like BiOBr hollow and porous structures synthesized via a reactable ionic liquid. *Dalton Transcation*, 40 (19), pp. 5249-5258.

- Xiao, F. X. et al., 2015. One-Dimensional Hybrid Nanostructures for Heterogeneous Photocatalysis and Photoelectrocatalysis. *Small*, 11 (18), pp. 2115-2131.
- Xiao, P., Zhu, L., Zhu, Y. and Qian, Y., 2011. Selective hydrothermal synthesis of BiOBr microflowers and Bi<sub>2</sub>O<sub>3</sub> shuttles with concave surfaces. *Journal of Solid State Chemistry*, 184, pp. 1459-1464.
- Xiao, P., Zhu, L., Zhu, Y. and Qian, Y., 2012. Room-Temperature Synthesis of BiOBr Sub-Microflowers and Their Photocatalytic Properties. *Journal of Nanoscience and Nanotechnology*, 12 (3), pp. 2008-2013.
- Xiao, W. et al., 2014. Structural Correspondence of Solution, Liquid Crystal, and Crystalline Phases of the Chromonic Mesogen Sunset Yellow. *Crystal Growth and Design*, 14 (8), pp. 4166-4176.
- Xiao, Y. et al., 2016. Photocatalytic removal of cefazolin using Ag<sub>3</sub>PO<sub>4</sub>/BiOBr under visible light and optimization of parameters by response surface methodology. *Journal of Industrial and Engineering Chemistry*, 45, pp. 248-256.
- Xing, H. et al., 2015. Preparation of BiOBr by solvothermal routes with different solvents and their photocatalytic activity. *Journal of Renewable and Sustainable Energy*, 7 (6).
- Xiong, J. et al., 2014. Direct conversion of Bi nanospheres into 3D flower-like BiOBr nanoarchitectures with enhanced photocatalytic properties. *RSC Advances*, 4 (2), pp. 583-586.

- Xu, J., Li, L., Guo, C., Zhang, Y. and Wang, S., 2013. Removal of benzotriazole from solution by BiOBr photocatalysis under simulated solar irradiation. *Chemical Engineering Journal*, 221, pp. 230-237.
- Xue, C. Xu, X., Yang, G. and Ding, S., 2015. Comprehensive investigation on the reciprocity of structure and enhanced photocatalytic performance in finned-tube structured BiOBr/TiO<sub>2</sub> heterojunction. *RSC Advances*, pp. 1-9.
- Xue, C. et al., 2014. A facile and efficient solvothermal fabrication of three-dimensionally hierarchical BiOBr microspheres with exceptional photocatalytic activity. *Materials Letters*, 133 (3), pp. 274-277.
- Yu, H. et al., 2017. Liquid Phase Exfoliation into Monolayered BiOBr Nanosheets for Photocatalytic Oxidation and Reduction. *ACS Sustainable Chemistry and Engineering*, 5 (11), pp. 10499-10508.
- Yu, X. et al., 2016. A Three-Dimensional BiOBr/RGO Heterostructural Aerogel with Enhanced and Selective Photocatalytic Properties under Visible Light. *Applied Surface Science*, 396, pp. 1775-1782.
- Yu, Z., Bahnemann, D., Dillert, R., Lin, S. and Lu, L., 2012. Photocatalytic degradation of azo dyes by BiOX (X = Cl, Br). *Journal of Molecular Catalysis A: Chemical*, 365, pp. 1-7.
- Yuan, Q. L., Zhang, Y., Yin, H. Y., Nie, L. Q. and Wu, W. W., 2015. Rapid, simple and low-cost fabrication of BiOBr ultrathin nanocrystals with enhanced visible light photocatalytic activity. *Journal of Experimental Nanoscience*, 11 (5), pp. 359-369.

- Zangeneh, H. et al., 2014. Photocatalytic oxidation of organic dyes and pollutants in wastewater using different modified titanium dioxides: A comparative review. *Journal of Industrial and Engineering Chemistry*, 26, pp. 1-36.
- Zhang, D., Li, J., Wang, Q. and Wu, Q., 2013. High {001} facets dominated BiOBr lamellas: facile hydrolysis preparation and selective visible-light photocatalytic activity. *Journal of Materials Chemistry A*, 1 (30), pp. 8622-8629.
- Zhang, D. et al., 2011. Ionothermal synthesis of hierarchical BiOBr microspheres for water treatment. *Journal of Hazardous Materials*, 211-212, pp. 104-111.
- Zhang, H. et al., 2014. Enhanced Photocatalytic Properties in BiOBr Nanosheets with Dominantly Exposed (102) Facets. *Journal of Physical Chemistry C*, 118 (26), pp. 14662-14669.
- Zhang, H., Niu, C. G., Yang, S. F. and Zeng, G. M., 2016. Facile fabrication of BiOIO<sub>3</sub>/BiOBr composites with enhanced visible light photocatalytic activity. *RSC Advances*, 6 (69), pp. 64617-64625.
- Zhang, J. et al., 2013. Exceptional visible-light-induced photocatalytic activity of attapulgite–BiOBr–TiO<sub>2</sub> nanocomposites. *Applied Clay Science*, 90, pp. 135-140.
- Zhang, J., Lv, J., Dai, K., Liang, C. and Liu, Q., 2017. One-step growth of nanosheet-assembled BiOCl/BiOBr microspheres for highly efficient visible photocatalytic performance. *Applied Surface Science*, 430, pp. 639-646.

- Zhang, J., Han, Q., Zhu, J. and Wang, X., 2016. A facile and rapid room-temperature route to hierarchical bismuth oxyhalide solid solutions with composition-dependent photocatalytic activity. *Journal of Colloid and Interface Science*, 477, pp. 25-33.
- Zhang, J. et al., 2008. Self-Assembled 3-D Architectures of BiOBr as a Visible Light-Driven Photocatalyst. *Chemistry of Materials*, 20 (9), pp. 2937-2941.
- Zhang, K. et al., 2014. Mechanochemical destruction of decabromodiphenyl ether into visible light photocatalyst BiOBr. *RSC Advances*, 4 (28), pp. 14719-14724.
- Zhang, L., Cao, X. F., Chen, X. T. and Xue, Z. L., 2010. BiOBr hierarchical microspheres: Microwave-assisted solvothermal synthesis, strong adsorption and excellent photocatalytic properties. *Journal of Colloid and Interface Science*, 354, pp. 630-636.
- Zhang, S. and Wang, D., 2015. Preparation of novel BiOBr/CeO<sub>2</sub> heterostructured photocatalysts and their enhanced photocatalytic activity. *RSC Advances*, 5, pp. 93032-93040.
- Zhang, X. et al., 2012. Synthesis and photocatalytic activity of graphene/BiOBr composites under visible light. *Applied Surface Science*, 258, pp. 7826-7832.
- Zhang, Y. et al., 2017. N-situ synthesis of heterostructured BiVO<sub>4</sub>/BiOBr core-shell hierarchical mesoporous spindles with highly enhanced visible-light photocatalytic performance. *Journal of Alloys and Compounds*, 713, pp. 78-86.

- Zhao, X., Wang, Y., Shi, Z. and Fan, C., 2011. Photocatalytic treatment of MO in water with BiOBr photocatalyst. *Materials Science Forum*, 694, pp. 554-558.
- Zhu, S. R. et al., 2017. In situ growth of MOF on BiOBr 2D material with excellent photocatalytic activity for dye degradation. *Crystal Growth and Design*, 17 (5), pp. 2309-2313.

## APPENDIX

### APPENDIX I

FESEM images for BiOBr nanosheets

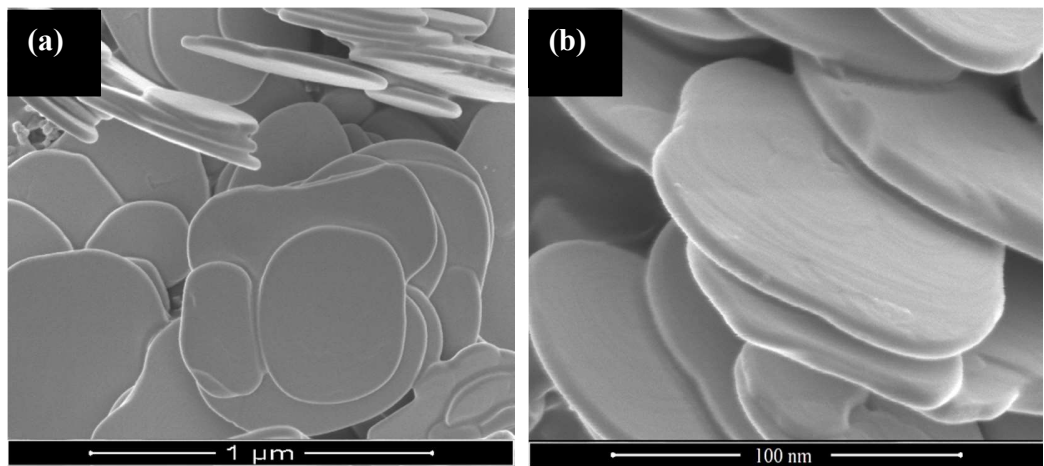


Figure A1 FESEM images for BiOBr nanosheet at different magnification (a) 20000X and (b) 50000X

## APPENDIX II

N<sub>2</sub> adsorption-desorption isotherm analysis of flower-like BiOBr and BiOBr nanosheets

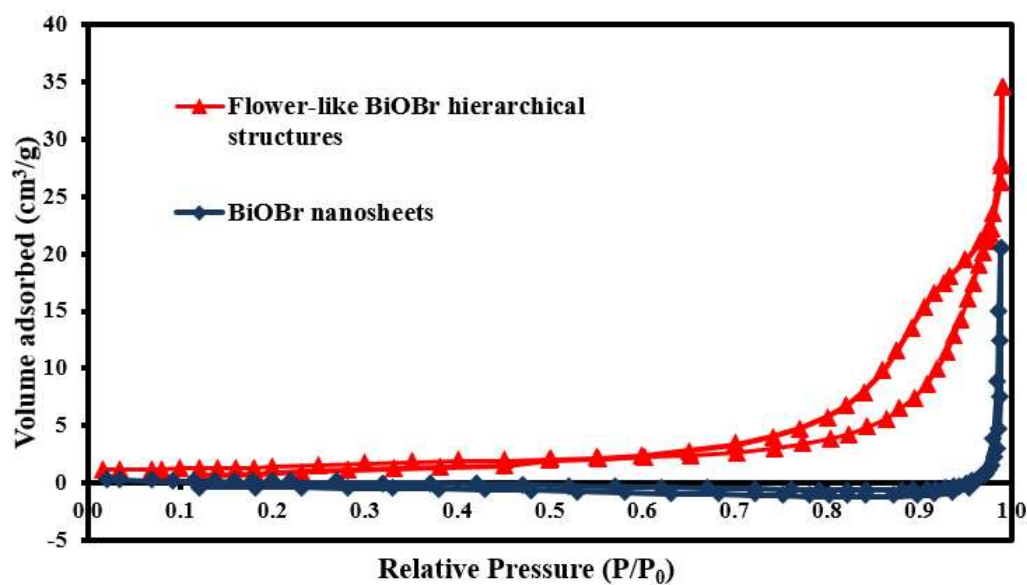


Figure A2 N<sub>2</sub> adsorption-desorption analysis of flower-like BiOBr and BiOBr nanosheet.

Table A1 BET surface area of flower-like BiOBr and BiOBr nanosheets.

Samples	BET surface area
BiOBr nanosheets	4.7595 m <sup>2</sup> /g
Flower-like BiOBr	0.0708 m <sup>2</sup> /g



## LIST OF PUBLICATION

1. Chin-Aik Lim, Jin-Chung Sin, Sze-Mun Lam, Abdul Rahman Mohamed. Synthesis of flower-like BiOBr hierarchical structures for photocatalytic degradation of sunset yellow under visible light irradiation. *Multidisciplinary Academic Conferences 2017 (MULAC 2017)*, 12<sup>nd</sup> & 13<sup>rd</sup> May 2017, Kota Kinabalu, Sabah.
2. Jin-Chung Sin, Chin-Aik Lim, Sze-Mun Lam, Abdul Rahman Mohamed, 2017, Surfactant-free hydrothermal synthesis of flower-like BiOBr hierarchical structure and its visible light-driven catalytic activity towards the degradation of sunset yellow, *Journal of Materials Science: Materials in Electronics*, 28, pp. 13236–13246.
3. Jin-Chung Sin, Chin-Aik Lim, Sze-Mun Lam. Photocatalytic degradation of organic pollutants using surfactant-free hydrothermally prepared flower-like BiOBr hierarchical structures under visible light irradiation, *IOP Conference Series: Earth and Environmental Science*, Accepted.
4. Chin-Aik Lim, Jin-Chung Sin, Sze-Mun Lam, Abdul Rahman Mohamed, 2017, Flower-like BiOBr hierarchical structures for enhanced photocatalytic degradation of sunset yellow using a low power energy saving light bulb, Submitted to *Materials Science in Semiconductor Processing*.